On the Dynamics of Magnetic Fluids in Magnetic Resonance Imaging

by

Pádraig J. Cantillon-Murphy

Submitted to the Department of Electrical Engineering and Computer Science

in partial fulfillment of the requirements for the degree of

Doctor of Philosophy

at the

MASSACHUSETTS INSTITUTE OF TECHNOLOGY

[June 2008]
May 2008

Author .....
.....
Department of Electrical Engineering and Computer Science
May 22nd, 2008.

Certified by ...
.....
Elfar Adalsteinsson

R.J. Shillman Assistant Professor of
Electrical Engineering and Computer Science
Harvard-MIT Health Sciences and Technology
Thesis Supervisor

Certified by ..
.....
Markus Zahn

Thomas and Gerd Perkins Professor of
Electrical Engineering
Thesis Supervisor

Accepted by .....
Terry P. Orlando
Chairman, Department Committee on Graduate Students

On the Dynamics of Magnetic Fluids in Magnetic Resonance Imaging

by

Pádraig J. Cantillon-Murphy

B.E., Electrical and Electronic Engineering

University College Cork, Ireland, 2003.

S.M., Electrical Engineering and Computer Science

Massachusetts Institute of Technology, 2005.

Submitted to the Department of Electrical Engineering and Computer Science

on May 22nd 2008, in partial fulfillment of the requirements for

the degree of Doctor of Philosophy

Abstract

The hydrodynamics of magnetic fluids, often termed ferrofluids, has been an active area of research since the mid 1960s. However, it is only in the past twenty years that these fluids have begun to be used in magnetic resonance imaging (MRI) where they have found application as contrast agents, improving the contrast to noise ratio of the received MR intensity.

The major goal of this work was to assess the feasibility of modulating the signal intensity in MRI in regions near superparamagnetic iron oxide contrast agents by applying a rotating magnetic field. Analytical study and numerical simulations of the effects of such a rotating magnetic field are presented. Simulated variations in fluid magnetization are achieved by changing the frequency of the rotating magnetic field. A linearization of the equilibrium magnetization Langevin relation results in a small signal magnetic susceptibility tensor that can be used to influence fluid flow. The feasibility of the approach under the real-life constraints of MR imaging are assessed. Also examined is the potential for coupling changes in magnetization due to rotating fields with hyperthermia treatment of cancerous tissue.

In addition to theoretical and simulated analysis, considerable experimental work was undertaken at the MRI systems of the HST Athinoula A. Martinos Center for Biomedical Imaging at Massachusetts General Hospital, Charlestown, Massachusetts. This work evaluated the passive behavior of both commercial ferrofluids and MRI

contrast agents. The ability of MRI to serve as a highly accurate indicator of the fluid's physical and magnetic properties is shown. The thesis represents the first investigation into the use of the hydrodynamic properties of magnetic fluid in the presence of a rotating field as a mechanism for contrast in MRI. The results show the possibility of varying MR image intensity under careful selection of field conditions.

Thesis Supervisor: Elfar Adalsteinsson
Title: Assistant Professor of Harvard-MIT Division of Health Sciences and Technology and Robert J. Shillman Career Development Assistant Professor of Electrical Engineering

Thesis Supervisor: Markus Zahn
Title: Thomas and Gerd Perkins Professor of Electrical Engineering

Acknowledgements

There are so many many people to whom I am indebted. I begin with my advisors, Professors Zahn and Adalsteinsson for their constant support and encouragement throughout these last years. Also to Professor Wald for his words of wisdom. I would like to acknowledge everybody in the MRI group at RLE for their help and support as well as those at the Martinos Center for Biomedical Imaging who were of such an immense help in the experimentation.

I thank all of my friends and community for their prayers and encouragement over the final difficult months. I want to acknowledge the families of both Grâce and I who were of enormous support throughout! In particular, I want to acknowledge uncle Aubs who always taught me to reach for the stars, auntie Mamie, who helped keep my feet on the ground and my aunts and uncles who always had me in mind. I want to thank my brothers, Éamonn and Mícheál, and my parents, for their love, concern and for supporting me always in my work. Finally, I thank my wife Grâce, my constant solace and joy of my life...for everything! You are a blessing I could never have imagined.

And finally, finally to St. Teresa of Avila because her saying I have found to be true...

Let nothing disturb you,
Let nothing frighten you,
All things pass:
God never changes.
Patience obtains all.
Whoever has God lacks nothing;

God alone is enough.

"Set against personal struggles, moral confusion and fragmentation of knowledge, the noble goals of scholarship and education, founded on the unity of truth and in service of the person and the community, become an especially powerful instrument of hope."

His Holiness Pope Benedict XVI.
Address to Catholic Educators of the United States.
Catholic University of America, Washington DC.
April 17, 2008.

Contents

List of Tables

List of Figures

Note on the Outline of the Thesis

1. Chapter 1 presents the basics of ferrofluids and MRI. This chapter represents a bridging of the fields of ferrohydrodynamics and MRI.

2. In chapter 2, the theoretical work is begun with an examination of the effect on fluid magnetization in regions near a compartment of SPIO contrast agent by applying a rotating magnetic field transverse to the main DC field that characterizes MRI. Analytical study and numerical simulations of the effects of such a rotating magnetic are included.

3. Chapter 3 expands the work of the preceding chapter to account for a rotating magnetic field where one of the components is parallel to the main field. Again, analytical and numerical results are presented in some detail.

4. Chapter 4 includes a brief examination of the feasibility of mechanical rotation of a vial of contrast agent as a means for modulating the magnetic fluid's magnetization which, in turn, would change the MRI intensity.

5. In chapter 5, experimental results from MRI investigations at the Martinos Center are presented. These include measurements of contrast agent magnetization at 3T and comparison with results from vibrating sample magnetometry as well as investigations of the effects of gradients in the magnetic field, ferrofluid

nanoparticle chaining and sensitivity of the contrast agent to transverse field components.

6. Chapter 6 examines the experimental results for magnetic fluid flow in the presence of the MRI's B_0 field gradient at the magnet's edge. The effects are investigated for various dosages of commercial MRI contrast agents.

7. Chapter 7 details the application of RF fields in MRI in the presence of magnetic nanoparticles. The application of RF fields causing non-ohmic heating due to the magnetic nanoparticles is presented.

8. The thesis ends with chapter 8 which includes a summary of the major contributions from the work as well as suggestions for future work.

Chapter 1

Introduction to Magnetic Fluids and MRI

Magnetic Resonance Imaging (MRI) is an investigative and diagnostic tool used to visualize the structure and function of tissue in living organisms. The image contrast associated with MRI is due to the response of water protons in the presence of external magnetic fields. Exciting water protons and observing their relaxation behavior enables the clinician to make diagnosis. Due to similarities between many bodily cells and tissues, it is sometimes difficult to achieve this goal with traditional MRI. The use of contrast agents can reduce this problem. Examples include the investigation of vascular tissues (*e.g.*, tumors), the assessment of brain perfusion (*e.g.*, in stroke), imaging of the gastrointestinal tract and liver and, most recently, cancer imaging by cell-labelling [1–5]. Contrast agents seek to aid the clinician by enhancing the variability across an MR image. However, once contrast agent is administered to the patient, it is beyond the control of the clinician to influence the image intensity in the neighborhood of the agent. A highly desirable property of contrast agent would be active *in vivo* control so that the clinician might direct and manipulate MR image

intensity even after it has been administered to the patient. This would place MRI on a more even footing with emerging imaging technologies, in particular Positron emission tomography (PET). PET has a unique ability to not only provide images but also to do so with high sensitivity and to provide both relative and absolute quantification [6].

The goal of this work is to propose a means to modulate MR image intensity by application of a rotating magnetic field in addition to the usual magnetic fields present in MRI. This would be achieved by applying the fields in the neighborhood of iron oxide nanoparticles and the effect of image modulation would be seen in nearby water compartments.

The thesis begins by describing the salient properties of superparamagnetic iron oxide (SPIO) particles in high-concentration suspensions and a brief introduction to the basics of MRI. The particle properties are coupled to the governing constitutive relations and boundary equations of physics to solve the particular problem of MR image intensity in water located in the macroscopic vicinity of a compartment of SPIO particles in a water suspension, referred to as a "ferrofluid". The system is investigated by means of *Comsol Multiphysics* software simulations. In addition to the main z-directed B_0 magnetic field, which is a very strong static field, a weak rotating field, B_{rot}, is applied in the transverse $\{xy\}$ and longitudinal $\{yz\}$ planes. It is shown that the frequency of B_{rot}, denoted Ω, can be used to modulate the MR image intensity in the vicinity of the compartment under strict constraints by introducing an additional source of rotating field, not currently found on the conventional MRI system. The theoretical effect is investigated and found to be present when the "spin-velocity" of the ferrofluid is significant and the value of Ω approaches the reciprocal of the ferrofluid's characteristic time constant, τ.

1.1 Prior Work on Ferrofluids in MRI

The ferrohydrodynamics of suspensions of iron-oxide (usually consisting mainly of magnetite, Fe_3O_4) in carrier liquids such as oil or water, commonly termed ferrofluids, is well-understood [42, 48, 50, 51]. Following the analysis of Shliomis [48], much work has sought to validate his theory through experiment [49, 52, 53] and these efforts have proven convergent with the established theory, at least while the ferrofluid remains well outside the region of complete magnetic saturation. Iron oxide nanoparticles were first proposed as a contrast agent in MRI by Weissleder [59] with subsequent application by many other investigators [63, 64]. Water-based ferrofluids have found application as imaging contrast agents [59], particularly in tumor imaging [1]. Scientists and clinicians in the MRI field preferred the term superparamagnetic iron oxide (SPIO) agents, rather than ferrofluids. In 2002, Feridex[1] became the first FDA-approved SPIO agent for clinical studies. While much important work has been undertaken to characterize the biomedical, physical and passive magnetic properties of such SPIO agents [57, 58], including the relaxivity critical to contrast in MRI [8–10, 25], there has yet been no attempt, until now, to analyze the effect of ferrofluid spin-velocity on MR imaging. This work, the subject of a filed patent application [7], investigates the use of the spin velocity of magnetic nanoparticles in presence of a rotating magnetic field as a possible source of image contrast in MRI.

Contrast agents fall under two categories: positive and negative agents. Positive contrast agents increase signal intensity and usually refers to Gadolinium-based agents (also called T1 agents). Negative contrast decreases signal intensity and this usually

[1]Feridex is manufactured by AMAG Pharmaceuticals, Cambridge, Massachusetts and distributed by Bayer Pharmaceuticals under a licensing agreement. Up until 2007, AMAG was known as Advanced Magnetics. Feridex is sold in Europe under the brandname of Endorem and is licensed to Guerbet, a French pharmaceutical firm.

refers to SPIO agents (also called T2 agents). One novel work has proposed SPIO as a positive contrast agent (rather than a negative agent as it is usually employed) by means of spectrally selective RF pulse excitation and subsequent off-resonance readout of the surrounding water spins [66]. A separate technique [67] involves the use of Oxygen-17 as an effective T2 relaxation[2] agent where the additional T2 relaxation associated with ^{17}O can be suppressed at will by irradiation of the oxygen resonance before the signal is collected for image reconstruction. Reported results suggest comparable contrast to noise ratios (CNR) to diffusion and Gadolinium contrast mechanisms. However, it would appear that no prior work investigates the application of the spin velocity associated with SPIO particles such as magnetite to the field of MRI contrast enhancement.

1.2 Physical Properties of Ferrofluids

Iron-oxide particles, often referred to as SPIO particles, are a commonly used MR contrast agent [27, 59, 63, 64] as discussed in the previous section. The particles, oftentimes magnetite (Fe_3O_4), usually measure between 5 and 15 nm in diameter and are contained in a carrier liquid such as water as depicted in Figure 1-1. To prevent the particles agglomerating, a thin surfactant coating surrounds each particle [65]. Oleic acid is a common surfactant in oil-based ferrofluids while *dextran* became the preferred surfactant in the early development of iron-oxide particles for MRI [59]. SPIO particles represent an enormous disturbance of the local magnetic field in an MRI environment. Single-domain magnetite particles have a typical local magnetization equal to 0.56 T (although this varies with volume). This field disturbance will fall off inversely proportional to the cubic distance from the nanoparticle [35, 42],

[2] T1 and T2 are the usual MRI relaxation time constants, discussed in detail in Section 1.4.3

so that, for typical imaging fields of 1.5 T, the effect due to a single nanoparticle will not extend radially beyond approximately 10 μm from the particle's center. In reality, each MRI imaging voxel[3] contains many thousands or tens of thousands of nanoparticles. Therefore, the voxel's image intensity is a smeared or averaged effect due to all the nanoparticles within the voxel. Even with this averaging effect, SPIO agents are a potent MR contrast agent. In order to produce MR images with sufficient signal to noise ratio[4] (SNR) to allow the region where the contrast agent is present to be differentiated from background noise, typical solid volume fractions lie in the ppm range. However, it should be noted that magnetite volume fractions of 0.008 have been tested on live rat brain [69] investigating capillary diffusion in the *dorsal hippocampus*. The work of this thesis uses solid volume fractions varying from 0.01 to 0.03 in order to achieve a perceptible effect due to spin-velocity effects. Although the effects of nanoparticle spin-velocity persist at lower particle concentrations, they are not significant enough to impact the MRI environment. At such high concentrations, the SPIO solution is referred to as a ferrofluid, in keeping with physics parlance [42, 68].

[3]Typical MRI imaging voxels are cubes on the order of 2 to 4 mm in length for high resolution imaging.

[4]SNR compares the level of a desired signal to the level of background noise. SNR is optimal for low concentrations of ferrofluid with all other MR parameters fixed. However, at very low concentrations (solid fractions less than 10^{-8}), the effect of the magnetic nanoparticles will cease to be apparent in MRI. Conversely, at very high concentrations (solid fractions greater than 10^{-4}), regions containing nanoparticles become indistinguishable from the background noise. This latter phenomenon is not critical if the tissue surrounding the highly concentrated agent has a relatively high image intensity, yielding good contrast to noise ratio (CNR) in the resultant MRI. Thus arises the distinction between SNR and CNR.

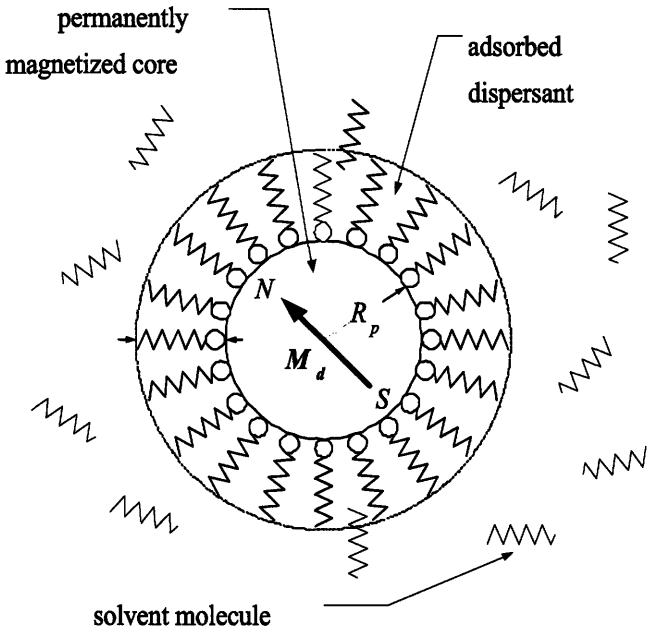

Figure 1-1: Each ferrofluid particle consists of a superparamagnetic core surrounded by a surfactant (also called dispersant) layer. This has a dual purpose in MRI: to avoid agglomeration and to render the particle biocompatible.

1.3 Ferrofluid Time Constant, τ

In the absense of an external magnetic field, a superparamagnetic ferrofluid suspension has no net magnetization due to the random orientation of the nanoparticles in the suspension. Upon the application of an external DC magnetic field to a ferrofluid suspension, some fraction of the particles will rotate to align themselves with the applied field. The time for this alignment to occur is characterized by the ferrofluid relaxation time, τ, given by Eq. (1.1) and shown in Fig. 1-2 as a function of the magnetic core radius.

$$\frac{1}{\tau} = \frac{1}{\tau_B} + \frac{1}{\tau_N} \tag{1.1}$$

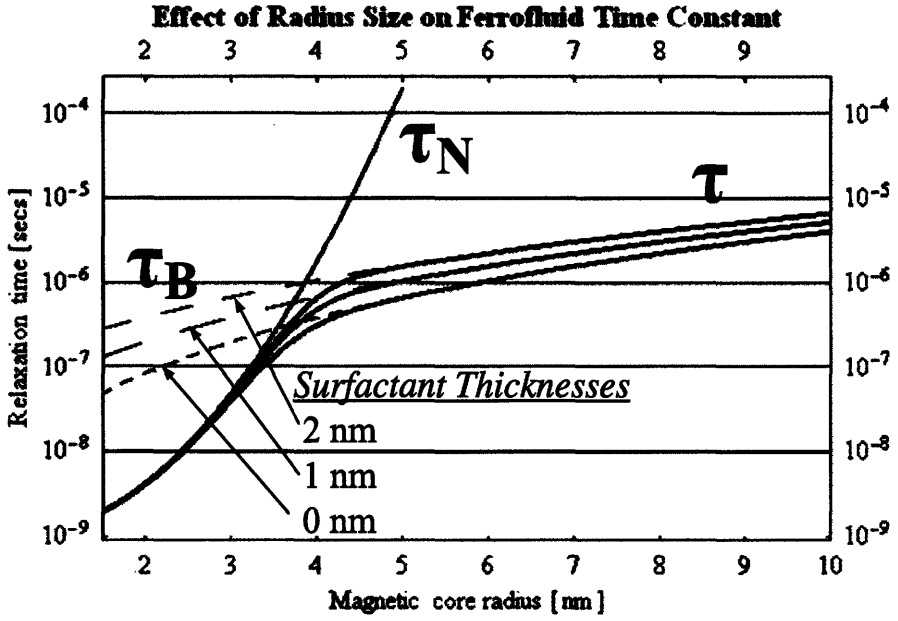

Figure 1-2: The ferrofluid time constant, τ, is usually dominated by either the Néel (τ_N) or Brownian (τ_B) relaxation times, depending on the particle's radius.

As seen from Eq. (1.1), the ferrofluid relaxation time, τ, is due to two distinct contributions. These are the Brownian (τ_B) and Néel (τ_N) relaxation times. For Brownian relaxation, which dominates at larger particle sizes, relaxation is due to particle rotation in the carrier liquid. For Néel relaxation, which is the dominant mechanism for smaller particle sizes, the mechanism is due to rotation of the magnetic vector within the particle. If the ferrofluid particle is constrained, for example by attaching it to a surface, Néel relaxation is still operative although Brownian is not. The relative expressions for τ_B and τ_N are given by Eq. (1.2) and Eq. (1.3) where:

V_h = Particle hydrodynamic volume in m^3 (includes surfactant contribution)

η = Dynamic viscosity of the carrier liquid (assumed that of water) in Pa· s

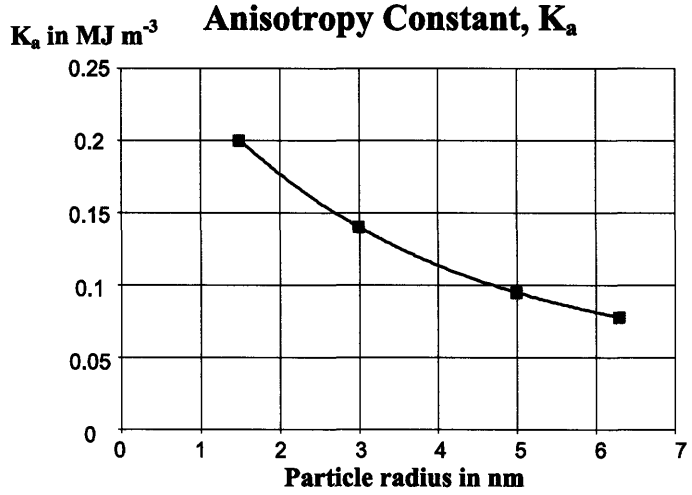

Figure 1-3: Recorded values of K_a are plotted along with an interpolated expression which is an excellent fit to the recorded results of Lehlooh et al. [55], [56] over the range of nanoparticles considered; magnetic core radii between 1.5 nm and 6.3 nm.

k = Boltzmann's constant = 1.38×10^{-23} in $\mathrm{m^2{\cdot}kg{\cdot}s^{-2}{\cdot}K^{-1}}$

T = absolute temperature in K, assumed 295 K unless stated.

V_p = Particle volume in $\mathrm{m^3}$ (excludes surfactant contribution)

K_a = Anisotropy constant in $\mathrm{J\,m^{-3}}$

τ_0 = Characteristic Néel time given by Rosensweig [42] as 1 ns

$$\tau_B = \frac{3\,V_h\,\eta}{k\,T} \tag{1.2}$$

$$\tau_N = \tau_0\, e^{\frac{K_a V_p}{kT}} \tag{1.3}$$

The value of the anisotropy constant, K_a, follows from the analysis of Lehlooh et al. [55, 56] who used collective magnetic excitation (CME) techniques to obtain

the values for K_a listed in Table 1.1. The analysis leading to the plot of Fig. 1-2 uses a third-order polynomial interpolation based on the values of Table 1.1, given by Eq. (1.4), to estimate the value of K_a for the entire range of feasible particle radii, R, given in meters, in the interpolated expression.

$$K_a = -4.47 \times 10^{29} R^3 + 9.24 \times 10^{21} R^2 - 7.46 \times 10^{13} R + 2.93 \times 10^5 \qquad (1.4)$$

The interpolated expression is plotted in Fig. 1-3 along with the recorded values for K_a from Table 1.1. For the plot of Fig. 1-2, surfactant thicknesses of 0, 1 and 2 nm are assumed and the temperature is 298 K.

Particle Radius in nm	K_a in J m^{-3}
6.3	0.78×10^5
5.0	0.95×10^5
3.0	1.40×10^5
1.5	2.00×10^5

Table 1.1: The anisotropy energy constant, K_a, for different particle radii, as calculated by Lehlooh [56] using CME.

1.3.1 Ferrofluid Langevin Parameter, L(α)

The fraction of magnetic nanoparticles in the ferrofluid that align with a static, external, magnetic flux density, B_0, with associated magnetic field[5] H_0, is determined

[5]In general $B_0 = \mu_0(H_0 + M_0)$ where μ_0 is the magnetic permeability of free space and M_0 is the magnetization of the sample. However, many times in MRI, where B_0 is 1.5 T or 3 T, $H_0 \gg M_0$

by the Langevin function, $L(\alpha)$, shown in Fig. 1-4 and described by Eq. (1.5) where:

$\mathbf{M}_{eq}$ = equilibrium magnetization in $\mathrm{A\,m^{-1}}$

$\mathbf{M}_s$ = saturation magnetization = $\phi\ \mathbf{M}_d$ in $\mathrm{A\,m^{-1}}$

M_d = single domain saturation magnetization for Fe_3O_4 ($\sim 446\ \mathrm{kA\,m^{-1}}$)

ϕ = unitless volume fraction of solids in the suspension[6]

α = unitless Langevin parameter = $\frac{\mu_0 V_p M_d H_0}{kT}$

V_p = magnetic volume of each particle in $\mathrm{m^3}$ (excluding surfactant)

$B_0 = \mu_0 H_0$ = applied external field in T

$$\mathbf{M}_{eq} = \mathbf{M}_s L(\alpha) = \mathbf{M}_s(\coth(\alpha) - 1/\alpha) \tag{1.5}$$

The Langevin parameter, α, describes the ratio of magnetic to thermal energy densities in the suspension [42]. If $\alpha \gg 1$, then the Langevin function approaches unity and practically all the particles are aligned with the applied field, B_0. The ferrofluid is referred to as "saturated". This is the typical operating domain for conventional SPIO contrast-agents in conventional, clinical MRI albeit at reduced particle concentrations.

Shliomis [48] has shown that if the external magnetic field is rotating, then the ferrofluid's equilibrium magnetization, $\mathbf{M}_{eq}$ (given by the Langevin function) will lag behind the time-varying magnetic field intensity, $\mathbf{H}$, that is applied, resulting in a body-torque density on the ferrofluid given by $\mu_0 \mathbf{M} \times \mathbf{H}$ where μ_0 is the permeability

since the applied field due to the magnet is dominant over the magnetization of the sample under investigation, even for ferrofluids. In this scenario, $B_0 \approx \mu_0 H_0$.

[6]Refer to Appendix B for an explanation of the various concentration units of relevance to MRI contrast agents.

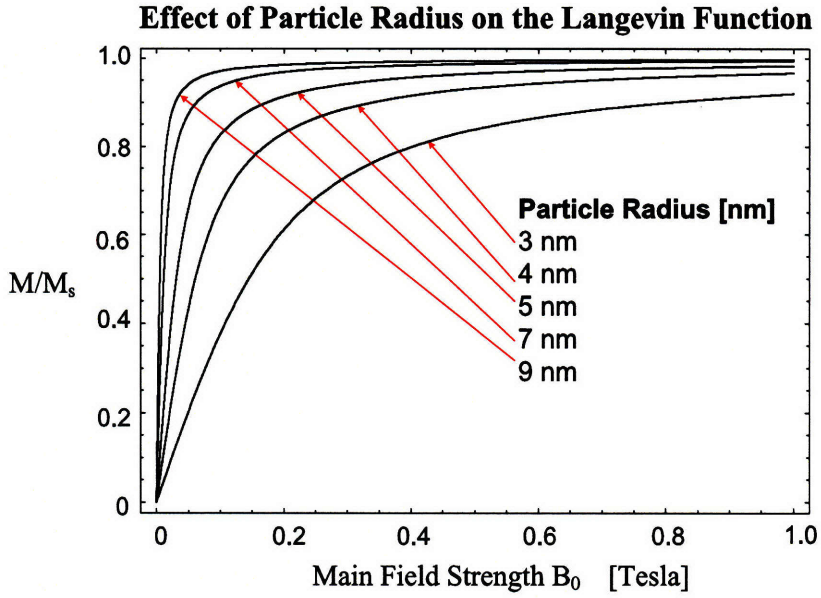

Figure 1-4: The equilibrium magnetization associated with each particle radius is determined by the Langevin function.

of free space in $\mathrm{H{\cdot}m^{-1}}$ and $\mathbf{M}$ is the instantaneous magnetization in $\mathrm{A\,m^{-1}}$. The fluid exhibits a spin velocity vector, $\boldsymbol{\omega}$, and its value is related to the other critical parameters by Shliomis' Relaxation Equation, given for an incompressible fluid[7] by Eq. (1.6) where:

$\mathbf{v}$ = fluid flow velocity vector in $\mathrm{m\,s^{-1}}$

$\boldsymbol{\omega}$ = fluid spin flow velocity vector in $\mathrm{s^{-1}}$

τ = relaxation time constant in s

[7]For an incompressible fluid, the divergence of the fluid flow velocity is identically zero, $\nabla \cdot \mathbf{v} = 0$

$$\frac{\partial}{\partial t}\mathbf{M} + \mathbf{v}\cdot\nabla\mathbf{M} - \boldsymbol{\omega}\times\mathbf{M} - (1/\tau)(\mathbf{M}-\mathbf{M_{eq}}) = 0 \tag{1.6}$$

While in the most general case, the equilibrium magnetization, $\mathbf{M_{eq}}$, is given by the Langevin function, for very low driving fields ($\alpha \ll 1$), $L(\alpha)$ might be approximated by the initial linear portion of the curve in Fig. 1-2. In this case, $\mathbf{M_{eq}}=\chi_0\mathbf{H}$ where χ_0 is the initial[8] susceptibility as given in Equation (2.28) of reference [42] and repeated in Eq. (1.7).

$$\chi_0 = \frac{\mu_0\,\phi\,\mathrm{M_d}^2\,\mathrm{V_p}}{3\,kT} \tag{1.7}$$

The following analysis follows a more general case applicable to the MRI environment. The equilibrium magnetization is estimated as $\mathbf{M_{eq}}=\chi_{eq}\mathbf{H}$ where χ_{eq} is the incremental susceptibility found from a small-signal linearization of the Langevin relation about an operating point defined by a large DC z-directed magnetic field intensity, H_0, with a corresponding equilibrium DC magnetization component, M_0, also z-directed, and given by the Langevin function evaluated at the operating point. Perturbations in the magnetic field intensity about this operating point can be represented by small-signal magnetic fields along the x, y and z axes, denoted $\tilde{h}_x$, $\tilde{h}_y$ and $\tilde{h}_z$. The corresponding small-signal magnetization, denoted $\tilde{m}_x$, $\tilde{m}_y$ and $\tilde{m}_z$, will be related to the small-signal magnetic field by the linearized Langevin relation. The full analysis is included in Appendix A and the final results are given in Eqs. (1.8) through (1.11), where $\alpha_0 = \frac{M_d\,V_p\,\mu_0\,H_0}{kT}$

[8]In this context, initial refers the presence of low field strengths, where the Langevin function can be approximated by its *initial* linear relation between the magnetization and the applied field.

$$M_0 = M_s\left(\coth(\alpha_0) - 1/\alpha_0\right) \tag{1.8}$$

$$\tilde{m}_x = \chi_x \tilde{h}_x = \frac{M_s}{H_0}\left(\coth(\alpha_0) - 1/\alpha_0\right)\tilde{h}_x = \frac{M_0}{H_0}\tilde{h}_x \tag{1.9}$$

$$\tilde{m}_y = \chi_y \tilde{h}_y = \frac{M_s}{H_0}\left(\coth(\alpha_0) - 1/\alpha_0\right)\tilde{h}_y = \frac{M_0}{H_0}\tilde{h}_y \tag{1.10}$$

$$\tilde{m}_z = \chi_z \tilde{h}_z = \frac{M_s}{H_0}\left(\frac{-\alpha_0}{\sinh^2(\alpha_0)} + \frac{1}{\alpha_0^2}\right)\tilde{h}_z = \frac{\partial M_0}{\partial H_0}\tilde{h}_z \tag{1.11}$$

It should be noted that for the case of a saturated ferrofluid, the Langevin function approaches unity, as already stated. In this case, the susceptibility tensor solvable from Eq. (1.6) approaches zero because **H** and **M** are increasingly decoupled and the slope of the Langevin curve approaches zero, although this is only important for the $\tilde{h}_z$ term. Shliomis has postulated that the formulation of Eq. (1.6) only remains valid when the excitation frequency Ω is maintained in the range $\Omega\tau < 10$ [51]. Beyond this range, it is unclear that the formulation still holds validity.

Finally, the analysis in this work induces spin velocity in the ferrofluid primarily by application of external rotating magnetic fields. It should be noted that spin velocity will also be observed in ferrofluid for flows with vorticity [42].

1.4 Magnetic Resonance Imaging

1.4.1 Introduction

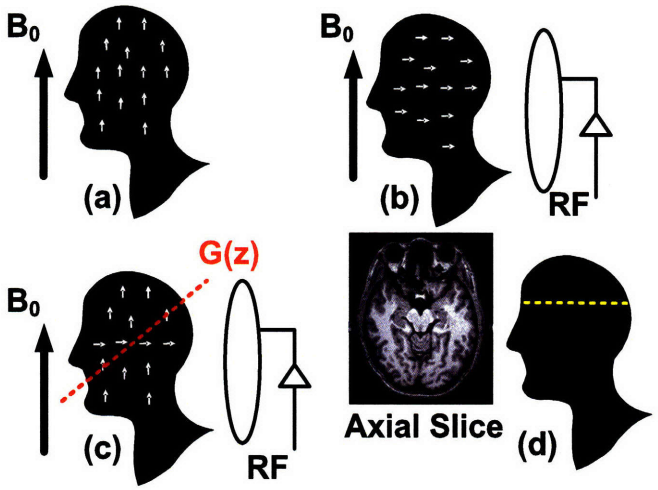

Figure 1-5: The fundamental elements of MRI are (a) dipole alignment, (b) RF excitation, (c) slice selection and (d) image reconstruction. The axial image slice is shown with grateful thanks to Divya Bolar (MIT/HST).

The purpose of this section is to introduce the reader to the fundamental principles of MRI in order to appreciate the work which follows. The interested reader is referred to reference texts such as Haacke's [35] or Bushong's [36] for further elaboration of the principles introduced in this work. In addition, Professor Dwight Nishimura's brief introductory text [37] is a superb "light" introduction to MRI. The online resources at the *MRI tutor*[9] as well as the personal websites of Professors Joseph P. Hornak[10] (Rochester Institute of Technology) and Brian Hargreaves[11] (Stanford University) are

[9]http://www.mritutor.org/mritutor/
[10]http://www.cis.rit.edu/htbooks/mri/inside.htm
[11]http://www-mrsrl.stanford.edu/~brian/intromr/

excellent additional resources. What follows represents an incomplete synopsis drawn from these and other resources.

1.4.2 Excitation

Magnetic Resonance Imaging, in the clinical environment, is usually used to detect signal from water molecules in the body. The dominant magnetic field associated with each of these molecules is that of the hydrogen proton, which has a dipolar magnetic field. In general, the hydrogen dipoles in the body are randomly oriented. In the presence of a large DC magnetic field, B_0, aligned along the z axis, some small net fraction of the dipoles align with the applied field, as shown in Fig. 1-5(a). If a radio-frequency (RF) source is now brought to bear on the aligned dipoles, it is found that at one particular frequency (the Larmor frequency, denoted ω_0) the dipoles will precess about their equilibrium orientation, lagging the RF field, denoted B_1, by 90° in space. If B_1 is orthogonal to B_0 (as is oftentimes the case in MRI), the dipoles will be tipped into the plane perpendicular to B_0, as depicted by Fig. 1-5(b). Typically, B_1 (which is only a small fraction of B_0) is applied in the $\{xy\}$ plane so that upon excitation, each dipole is "flipped" by 90°. In fact, the hydrogen proton's magnetization vector experiences nutation at $\omega_0 = 2\pi\gamma B_0$ as it tips away from B_0, where γ is referred to as the proton gyromagnetic ratio and its value for hydrogen is 42.58 MHz T^{-1}. When this tipping occurs, the component of the hydrogen magnetic dipole field moves from being aligned with the z axis to the $\{xy\}$ plane.

1.4.3 T1 and T2 Relaxation

After the B_1 excitation field is turned off, the dipole's magnetization vector relaxes back to align with B_0. As this occurs, the magnitude of the EMF that is induced in a

coil positioned perpendicular to the $\{xy\}$ plane is found to decrease from its value at the instant when the dipoles magnetization vector is aligned with B_1. The relaxation is characterized by two different time constants: T1 and T2. T1 relaxation, also referred to as longitudinal relaxation, is due to interactions between the dipole *spins*[12] and the lattice while T2 relaxation, also referred to as transverse relaxation, is due to interactions between the spins. T1 characterizes the return of the z component of magnetization back to its equilibrium value after excitation. T2 characterizes the decay of the transverse $\{xy\}$ component after excitation. Due to fluctuations in the magnetic field across a sample, T1 is always longer than T2. The Bloch equation which governs spin behavior in MRI is found in many texts, including equation (4.19) of reference [37] and is repeated in Eq. (1.12). M_0 is the equilibrium sample magnetization due to the B_0 field. However, in this case, M_0 is the equilibrium magnetization due to the water protons used for imaging and not the magnetization of the ferrofluid suspension.

$$\frac{\partial}{\partial t}\mathbf{M} = \mathbf{M} \times 2\pi\gamma\mathbf{B} - \frac{M_x\bar{\mathbf{i}}_x + M_y\bar{\mathbf{i}}_y}{T2} - \frac{(M_z - M_0)\bar{\mathbf{i}}_z}{T1} \tag{1.12}$$

In order to compile a coherent MR image, it is necessary to vary the Larmor frequency across the sample of interest, so that the signal corresponding to each spatial position is mapped to a particular temporal frequency. This variation is accomplished by means of gradient coils, highlighted in the example of Fig. 1-5(c) as $G(z)$, where G is a linear gradient in the z component of magnetic field along the z axis. The local Larmor frequency is then related to the local magnetic field by

[12] A nuclear *spin* refers to a non-classical kind of angular momentum intrinsic to a body, as opposed to orbital angular momentum, which is the motion of its center of mass about an external point. This quantum-mechanical spin is quantized in units of half or full integers. The proton is a spin-1/2 particle. In MRI, a spin is oftentimes (somewhat inaccurately) used to refer to the ^{1}H proton.

Eq. (1.13).

$$\omega_0 = 2\pi\gamma(B_0 + G(z)) \tag{1.13}$$

Adding further gradients in the x and y directions now allows for a three-dimensional array of frequency bins to be collected. This array is termed *k space* and the magnitude of each frequency bin corresponds to the MR signal strength from a particular voxel in the spatial domain. Mapping between the spatial and frequency domains is performed by a *Fourier* analysis. The final image, typified by Fig. 1-5(d), is usually multi-sliced although only one image is shown (in this case along the $\{xy\}$ or *axial* plane). Three-dimensional imaging is also possible.

1.4.4 Spin Dephasing and Compensation

In perfectly pure water, the values of the characteristic time constants, T1 and T2, would be identical. As noted previously, due to inhomogeneities occurring in all practical experiments, this is not the case. In fact, the decay of the magnetization in the $\{xy\}$ plane is rapid due to "spin dephasing". Due to inhomogeneities in the B_o field, each spin will experience slightly more or slightly less dephasing as time goes by. Spins which were initially coherently aligned (usually along the x axis) by excitation, rapidly fall out of coherence once the B_1 field is turned off. The net signal associated with their magnetization vector within a given voxel gradually falls away. This intrinsic decay is characterized by the T2* time constant.

The rapid effect of T2* decay limited the use of conventional MR imagery until Hahn [35] developed a compensating procedure that mitigates against rapid decay of the signal in the $\{xy\}$ plane: the "spin-echo" technique. The approach, highlighted in Fig. 1-6 is to flip all the spins at a time half-way between excitation and read-

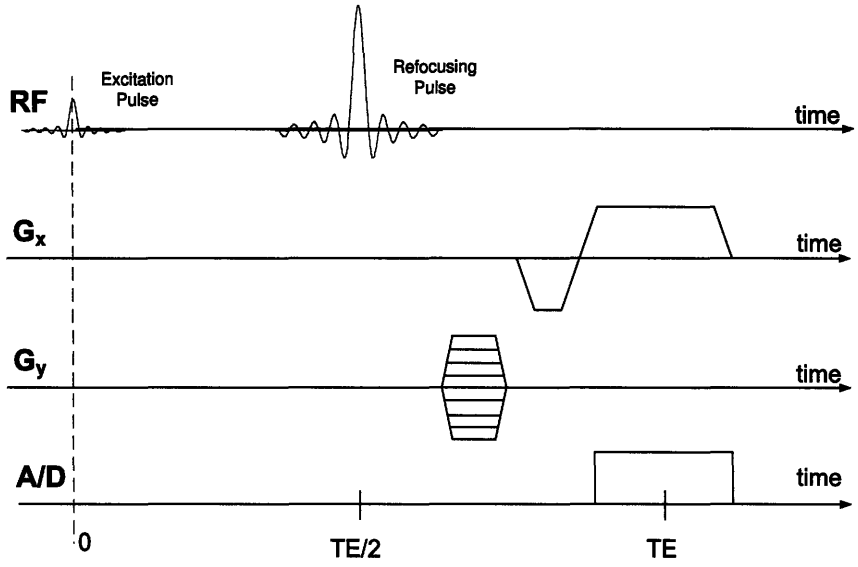

Figure 1-6: A typical "spin-echo" sequence includes a refocusing flip at half the time between excitation and read-out, TE. Representative gradient fields, G_x and G_y are also included. In general, the slice selection gradient, G_y, is varied during each TR to select a given slice along the y axis, as indicated in the figure.

out, denoted TE, thus causing the coherence to be reestablished at read-out. The rephased envelope of signal decay, shown in Fig. 1-7, has a new characteristic decay time termed T2. In fact, the intrinsic T2* time constant can be decomposed into two distinct contributions [35], as given by Eq. (1.14). T2′ is due to external field induced relaxation while T2 is due to thermal and diffusion effects in the material. The spin-lattice time constant, T1, is a mono-exponential rise back to the equilibrium value, as shown in Fig. 1-7.

$$\frac{1}{T2^*} = \frac{1}{T2} + \frac{1}{T2'} \tag{1.14}$$

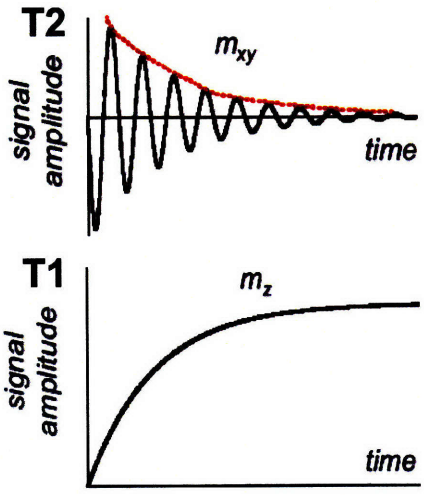

Figure 1-7: T2 decay is characterized by the exponential decay envelope of the magnetization signal in the $\{xy\}$ plane after excitation. T1 recovery is characterized by the exponential growth of the magnetization along the z axis as the vector returns to the equilibrium magnetization.

The time constants, T1 and T2 are unique for any material. The image contrast between tissue types in living humans which is so important to medical diagnosis and afforded by MRI is due mostly to T1 and T2 signal decay, in addition to factors such as spin density, tissue density etc. Typical values of T2 are 100 ms for gray matter deceasing to 40 ms for human liver [37]. T2 values in pure water typically range between 1 s and 3 s. T1 values *in vivo* can be significantly longer, reaching the order of several seconds.

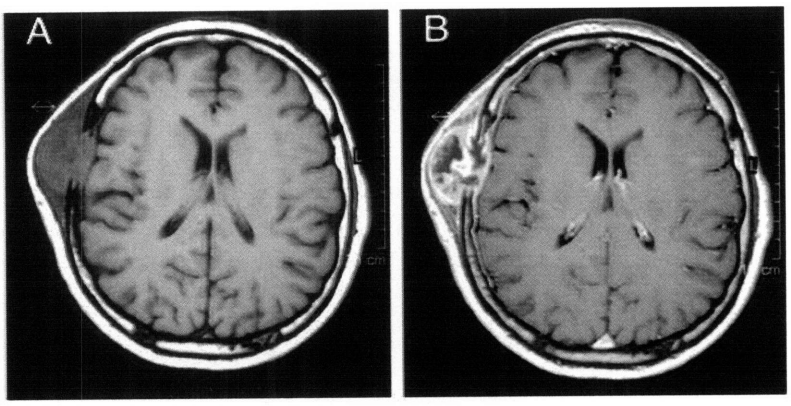

Figure 1-8: T1 weighted MRI of the brain (A) before and (B) after Gadolinium contrast enhancement, showing a metastatic deposit involving the right frontal bone with a large extracranial soft tissue component and meningeal invasion. This figure comes from a case report of suspected dormant micrometastasis in a cancer patient [75]. (Reproduced with the kind permission of Dr. Nagi S. El Saghir, Clinical Professor of Medicine Hematology-Oncology, American University of Beirut Medical Center.)

1.5 Contrast Agents

1.5.1 T1 and T2 contrast

Oftentimes when using MRI for diagnosing medical conditions *in vivo*, there is insufficient inherent contrast between adjacent human tissues to allow for medical personnel to reach a definitive clinical prognosis. This is often the case for stomach and small bowel imaging as well as for detection of vascular tissues (*e.g.*, tumors) and the assessment of brain perfusion (*e.g.*, in stroke victims). In such cases, it is common to administer a contrast-enhancing agent to the patient, either orally or by injection. Contrast-agents are effective when neighboring tissues have similar MRI relaxation times but absorb the contrast agents to varying degrees. Although there has been some work in the field of positive contrast agents using off-resonance refocussing effects in the presence of SPIO nanoparticles [66], almost all current contrast agents

decrease the effective time constant (either T1, T2 or a combination of both, depending on the particular agent) resulting in a time constant that is shorter for the tissue where absorption occurs. This is highlighted in Fig. 1-8 which shows a T1-weighted[13] MRI of the brain (A) before and (B) after *positive* Gadolinium contrast enhancement. Since the presence of the gadolinium agent primarily affects T1 relaxation, causing the imaging spins in the vicinity of the contrast agent to recover more quickly to their equilibrium position, a T1-weighted image will show increased image intensity or "positive" contrast enhancement in the presence of the agent. Hence, the referral to gadolinium agents as positive contrast agents. Alternately, SPIO agents primarily affect T2 relaxation. Imaging spins in the vicinity of the contrast agent exhibit more rapid dephasing in the presence of the agent and therefore, a T2-weighted image will show reduced or "negative" contrast compared to when the SPIO agent is absent. Hence, SPIO agents are often referred to as negative contrast agents.

The new time constants after either positive or negative contrast enhancement are approximated by Eqs (1.15) and (1.16) where C is concentration of agent, usually expressed in mol l^{-1} and R_1 and R_2 refer to the longitudinal and transverse relaxivities of the agent respectively, with units of $l{\cdot}s^{-1}{\cdot}mol^{-1}$. Contrast agents are usually selected so that either the longitudinal or transverse relaxivities are dominant, resulting in T1 (eg., Gadolinium-based) and T2 (eg., SPIO) contrast agents.

$$1/T1_{after} = 1/T1_{before} + R_1 C \tag{1.15}$$

$$1/T2_{after} = 1/T2_{before} + R_2 C \tag{1.16}$$

[13]MR images can be defined as either T1-weighted or T2-weighted, depending on the parameters TE (read-out time) and TR (repetition time between excitations). This analysis follows from the Bloch Equation and is found in reference [35]. Generally, for T2-weighted images TR$\gg$T2 with a long TE time and for T1-weighting, TE$\ll$T1 with a short TR time.

1.5.2 Predicting T1 and T2 Relaxation Times

As evident from Eqs (1.15) and (1.16), the altered relaxivity[14] associated with contrast agents is necessarily longer due to the inverse addition relation. T1 contrast-agents are generally paramagnetic and their magnetization is usually a linear function of the applied B_0 field. This is not always the case for T2 contrast agents, which are usually superparamagnetic materials and often operate at or near to magnetic saturation (as determined by the Langevin function of Fig. 1-4). Most T1 agents are gadolinium-based [28] and all act to decrease T1. Most commercial T2 agents are superparamagnetic suspensions, such as MION-46L [16] and Feridex [62], and these agents act to decrease T2.

Aqueous Solution Relaxation

In pure aqueous solutions, the dominant mechanism of T2 relaxation is dipole-dipole interactions. Dipole-dipole interactions refer to the spatially varying magnetic fields associated with the hydrogen protons of each water molecule. Since the dependence falls off as the sixth power of the distance from the dipole [34], the effect on any given hydrogen proton is only due to the other hydrogen proton of the same water molecule. Due to thermally-induced tumbling, there will be a spatial variation in the local B field experienced by each dipole, resulting in an exponentially decaying magnetization recorded by a receiver coil and characterized by the T2 time constant. Analytical expressions for intrinsic T1 and T2 of pure water are included as Equations (2.28) and (2.29) of reference [34] as well as in numerous other sources.

[14]The relaxivity of a contrast agent is defined as the inverse of relaxation time associated with the agent acting alone and has units of $\text{mol}^{-1}\,\text{s}^{-1}$. However, it is often expressed in units of s^{-1}, so that the final time constant (in seconds) is the result of adding the inverse of the time constant before contrast enhancement (sometimes called the "intrinsic relaxivity") to the contribution from the agent's relaxivity.

Outer and Inner Sphere Relaxation

Contrast agent electrons interact with the hydrogen spins of nearby water molecules in two ways and these are referred to as inner-sphere and outer-sphere relaxation. Inner-sphere relaxation refers to the direct exchange of energy between the proton spins and the electrons of the contrast agent and, in general, involves binding between the water molecules and the contrast agent. Inner sphere relaxation accounts for up to 50% of the relaxation effect in gadolinium-based agents [28]. Outer sphere relaxation occurs due to the movement of water molecules in the vicinity of the field inhomogeneities arising from the agent particles and usually does not involve binding. Inner sphere relaxation is modulated over frequency by a time constant which depends on proton exchange rate, ion rotation and electron spin relaxation. In outer sphere relaxation, this modulation is usually approximated by the diffusion time constant of the solution in the absence of contrast agents.

The relaxation of superparamagnetic suspensions in water is described by the theory of Outer Sphere Relaxation. This theory owes its derivation to quantum mechanical spin theory. After much debate within the literature, it appears that a correct formulation for the additional contribution to T1 and T2 relaxation due to superparamagnetic agents in water is given by equations (23a) and (23b) of Gillis' publication [10].

1.5.3 Superparamagnetic Relaxation

In the presence of superparamagnetic contrast agents, relaxation mechanisms other than dipole-dipole interactions become important. The theory of MRI relaxation in the presense of magnetic particles owes its beginnings to the Solomon-Bloembergen equations for diffusion [20] and has been subject to much revision and debate since

[8–10, 25]. It now appears that Gillis et al. [11, 13] have formulated a complete and experimentally verifiable theoretical prediction for the additional contribution to T2 in the presence of superparamagnetic particles. Their approach, relying heavily on a quantum derivation, is based on extending the analysis of paramagnetic agents to include the additional characteristics of superparamagnetic particles. The final analytical expressions given by Eqs. (23a) and (23b) of reference [10] for the additional contributions to T1 and T2 (expressed here in *SI* units) due to magnetic nanoparticles are given by Eqs. (1.17) and (1.18) in the *high field*[15] limit where "$\Re$e" denotes the real component of a complex quantity and where:

N_A = Avogadros' constant = 6.022×10^{23} mol^{-}1

μ_0 = magnetic permeability of free space = $4\pi \times 10^{-7}$ T·m·A^{-1}

C = molar concentration[16] of contrast agent in mol·m^{-3}

μ_m = magnetic dipole moment = $V_p M_d$ from Eq. (1.5)

τ_d = diffusion time constant in s from Eq. (1.21)

d = closest distance of approach of water molecule to SPIO particle in m

J_0 = power spectral density function from Eqs. (1.19) and (1.20)

τ = ferrofluid time constant from Fig. 1-2 and Eq. (1.1)

α = unitless Langevin parameter = $\frac{\mu_0 V_p M_d H_0}{kT}$

V_p = magnetic volume (excluding surfactant) of each particle in m^3

B_0 = applied external field in T

k = Boltzmann's constant = 1.38×10^{-23} m^2·kg·s^{-2}·K^{-1}

[15]Gillis' *high field* limit corresponds to a *high spin* limit, where S$\gg$1 in the quantum-based expressions he establishes. Since this is true of superparamagnetic particles over the entire range of Larmor frequencies, we can consider the expressions to be complete for superparamagnetic particles over all frequencies.

[16]A full discussion on the various terminologies employed to describe contrast agent concentration is included in Appendix B

T = absolute temperature in K

$$1/T1 = \frac{10^4 \mu_0^2}{135\pi} \gamma^2 N_A C \mu_m^2 \frac{\tau_d}{d^3} \{ 3 L^2(\alpha) J_0(\omega_0, \tau_d, \tau \rightarrow \infty) + 3 [1 - 2\frac{L(\alpha)}{\alpha} - L^2(\alpha)] J_0(\omega_0, \tau_d, \tau) \} \quad (1.17)$$

$$1/T2 = \frac{10^4 \mu_0^2}{135\pi} \gamma^2 N_A C \mu_m^2 \frac{\tau_d}{d^3} \{ L^2(\alpha) [3 J_0(\omega_0, \tau_d, \tau \rightarrow \infty) + 4 J_0(0, \tau_d, \tau_s \rightarrow \infty)] + [1 - 2\frac{L(\alpha)}{\alpha} - L^2(\alpha)] [3 J_0(\omega_0, \tau_d, \tau) + 4 J_0(0, \tau_d, \tau)] \} \quad (1.18)$$

$$J_0(\omega, \tau_d, \tau) = \Re e\{\frac{1 + 0.25 \Upsilon^{0.5}}{1 + \Upsilon^{0.5} + 4\Upsilon/9 + 1/9 \Upsilon^{1.5}}\} \quad (1.19)$$

$$\Upsilon = (\jmath\omega + 1/\tau) \tau_d \quad (1.20)$$

While the expressions seem unwieldy at first, it should be noted that these are general equations governing T1 and T2 over the entire spectrum of Larmor frequencies. The expressions for 1/T1 and 1/T2 are the analytical equivalents to the usually experimental values for the $R_{1,2} C$ terms in Eqs. (1.15) and (1.16). In reality, one is generally interested in the time constant at a particular frequency, corresponding to B_0 for the MRI system in question. However, since these expressions have been experimentally validated over a large range of ω_0 [8, 16], the theory of the approach merits discussion. For this work, the additional contribution from superparamagnetic particles to the T1 and T2 relaxation times is shown in Figures 1-9 and 1-10 respectively when the solid magnetic volume fraction is 1.38×10^{-6}.

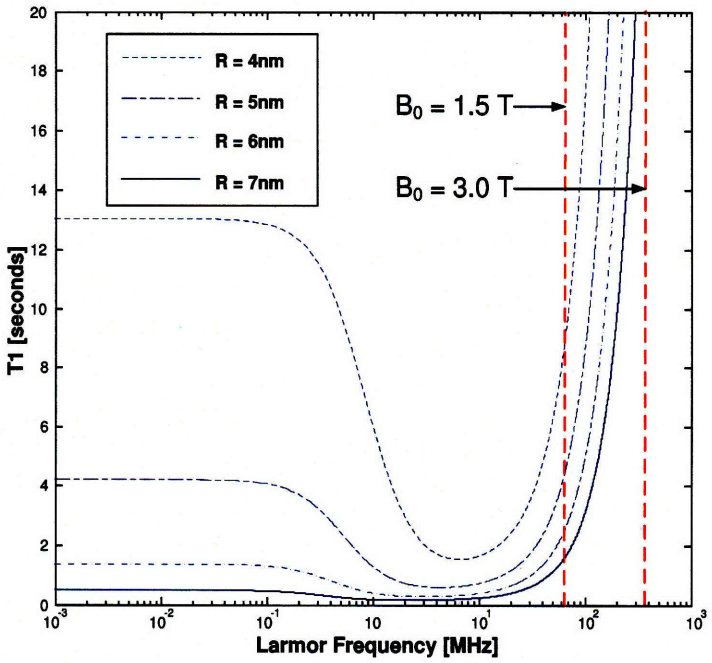

Figure 1-9: Theoretical contribution to T1 predicted by Equation 1.17 for superparamagnetic particles of magnetite with varying radii and a solid magnetic volume fraction of 1.38×10^{-6}.

Outer Sphere Relaxation Discussion

The power spectral density term, given by Eqs. (1.19) and (1.20), represents the correlation between ω_0 and the electron-proton modulation [28] and for superparamagnetic particles is dependent on two time constants: τ_d and τ, where τ is the previously defined ferrofluid time constant. The diffusion time constant τ_d is dependent on the "closest distance of approach", d, as given by Eq. (1.21) where D is approximated as the self-diffusion time constant of water at 25°C. Mills [29] has estimated D to be 2.4×10^9 $m^2 \cdot s^{-1}$ using an activation energy of 17.6 kJ/mol at room temperature.

$$\tau_d = \frac{d^2}{D} \tag{1.21}$$

While Gillis et al. approximate d as the effective radius of the magnetic nanoparticle [8], the approach of Bulte et al. [16] is to approximate it from experimental results of MION-46L[17] as 7.9 nm. Bulte's approach and approximation has been adopted in this analysis for convenience. Furthermore, the approximation of D as the self-diffusion time constant of water at 25°C is wholly justified given the very low superparamagnetic particle concentrations that are practical for imaging and the negligible variation of the Langevin function over the clinical temperature range. The analysis here is conducted assuming a temperature of 25°C.

Gillis notes that his expressions for T1 and T2 are only valid for small particle radii (up to 6.5 nm, from Fig. 1-4), when the Néel time constant dominates [11]. This follows from an earlier assumption made in his analysis concerning the anisotropic energy density [10].

It is evident that the expression for 1/T2 carries an additional DC term which does not arise in the T1 expression. It is the DC term that gives rise to net phase shifts in the $\{xy\}$ plane [34]. Terms containing an infinite τ term correspond to the relaxation effect due to the time-averaged component of the spin aligned with B_0, since the time-average is not affected by electron spin fluctuations [11]. The remaining terms result from the AC or fluctuating components of the spins aligned with B_0 and these terms do show a dependence on τ, as expected. A factor of 3, which was omitted in previous analysis [10] and now appears in the fluctuating (*i.e.*, ω_0-dependent) terms of both the expressions for 1/T1 and 1/T2, Eqs. (1.17) and (1.18), accounts for the alignment of superparamagnetic moment with the applied B_0 field.

In comparing Gillis' expressions to experimental results, it is important to consider the conversion of all quantities to *SI* units and to carefully consider the units of molar

[17]MION-46L is an ultrasmall monocrystalline superparamagnetic iron oxide believed to consist mainly of maghemite or magnetite crystals.

concentration, C. The theoretical work outlined here follows the approach of Bulte et al. [16] in applying Gillis' results to MION-46L particles in solution, where we only consider the superparamagnetic contribution detailed in [16]. Following this approach, the contributions from a ferrofluid dilution containing 1.38×10^{-6} solid volume fraction to the overall relaxation time constants, as given by Eqs. (1.15) and (1.16), are plotted in Fig. 1-9 and Fig. 1-10.

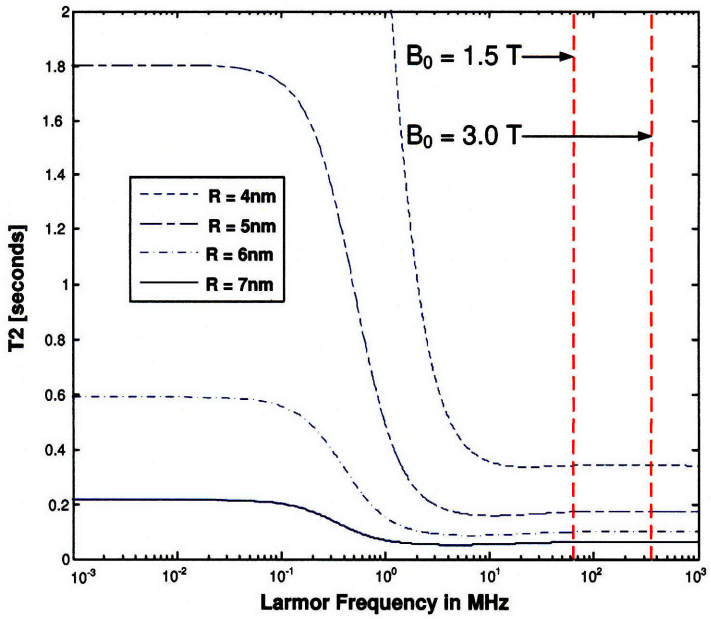

Figure 1-10: Theoretical contribution to T2 predicted by Equation 1.18 for superparamagnetic particles of magnetite with varying radii and a solid magnetic volume fraction of 1.38×10^{-6}.

Susceptibility Effects *in vivo*

While Gillis' theory of outer sphere relaxation is an accurate model for the relaxation of water molecules in aqueous solutions of superparamagnetic particles, the model does not account for the restrictions imposed on water diffusion *in vivo*. Instead

of the implicit assumption of unlimited diffusion which is true in the phenomenological model, diffusion is restricted in the body by compartmentalization of the contrast agent in various tissues and cells [28]. Consequently, the transverse relaxation time, T2, is considerably shorter *in vivo* than that predicted by the model and will be a function of the echo-time, TE [12,14,15,17]. The literature refers to this phenomenon of T2-shortening *in vivo* as susceptibility effects.

The longitudinal relaxation time, T1, is affected to a lesser extent since the local magnetic fields generated *in vivo* are large enough that T1 relaxivity due to the contrast agent has dispersed and the T1 decay is due mostly to the contribution from the solvent, which is usually water.

In spin-echo sequences, susceptibility effects are minimized since the phase of each individual spin is refocused in every echo with a consequent reduction in the total dephasing observed at the echo time, TE. This means that susceptibility effects are only of interest for the case of T2* imaging.

1.6 Results

1.6.1 T1 and T2 Estimation

In order to validate the model described in the previous section, a series of experiments were conducted to establish the T1 and T2 relaxivities due to an aqueous solution containing superparamagnetic particles. This work continued the initial evaluations of Professor Adalsteinsson which are included in Appendix C. Since the ferrofluid concentrations and imaging parameters varied considerably from his work to this, a meaningful comparison is difficult. However, the work is included for the interested

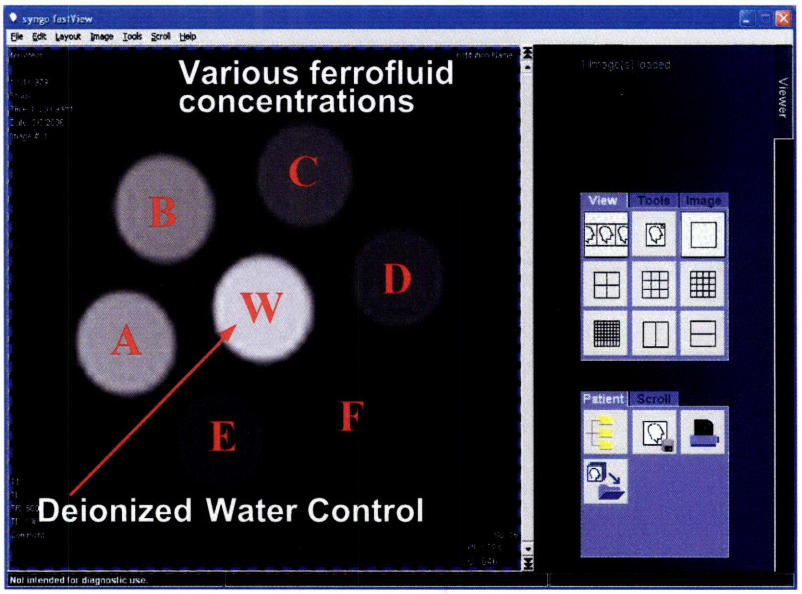

Figure 1-11: Various ferrofluid concentrations were examined at 1.5 T with reference to a deionized water control. The white vial W outlines indicate the regions of interest for quantification of T1 and T2 relaxation times.

reader. Various concentrations of MSG W11[18] ferrofluid in deionized water were placed in sealed cylindrical vials (11 cm in length, 2.8 cm in diameter) and the vials were placed in a 1.5 Tesla MRI. Results for T2-weighted images of vial cross-sections are shown in Fig. 1-11. Through careful selection of the TR and TE times, a relaxation series of curves was obtained and it was possible to arrive at an experimental relationship between the transverse and longitudinal relaxation times of the ferrofluid and the concentration of the ferrofluid in the vial. These results correspond to the combined effects of water and ferrofluid relaxation, as given by $T1_{after}$ and $T2_{after}$ of

[18]MSG W11 is a water-based ferrofluid available from Ferrotec Gmbh (Germany) containing 2.8% to 3.5% magnetite by volume with an estimated mean core radius of 4.7 nm [44]. Further information is at *http://www.ferrofluidics.de/pdf/si/msgw11.en.pdf*

Eqs. (1.15) and (1.16). The ferrofluid solution contained 2.75% magnetite by volume but in order to generate MR images with meaningful SNR, it was necessary to dilute the solution considerably as outlined in Table 1.2. The concentration dependence was fitted to a power curve and resulting experimental fit led to Eqs (1.22) and (1.23) where T1 and T2 have units of ms and ϕ is the solid volume fraction of the solution.

Vial	*Solid Volume Fraction, ϕ*	T1 in ms	T2 in ms
A	4.7×10^{-7}	1706	265
B	1.15×10^{-6}	1345	108
C	2.2×10^{-6}	1009	74
D	2.75×10^{-6}	887	57
E	5.5×10^{-6}	-	27
F	1.4×10^{-5}	-	20

Table 1.2: T1 and T2 results for various ferrofluid solid volume fractions, ϕ, of MSG W11 supplied by Ferrotec. At very high concentrations ($\phi > 5 \times 10^{-6}$), the SNR was not sufficient to allow for the accurate determination of T1 relaxation times.

$$T1 \approx 10.794\, \phi^{-0.348} \tag{1.22}$$

$$T2 \approx 0.00062\, \phi^{-0.889} \tag{1.23}$$

1.6.2 Significance of T1

The theoretical prediction of the total time constant for MSG W11 was obtained from the right-hand side of Eqs. (1.15) and (1.16) where $T1_{before}$ and $T2_{before}$ correspond to the longitudinal and transverse relaxation of pure water. The RC terms are as predicted by the outer-sphere relaxation model (Eqs. 1.17 and 1.18) at a Larmor frequency of 64 MHz (corresponding to 1.5 T, as given by $\omega_0 = 2\pi\gamma B_0$). The values of $T1_{before}$ and $T2_{before}$, due to pure water acting alone, are clearly independent of

ferrofluid concentration and in the most fundamental derivation would be derived from Eqs. (2.28) and (2.29) of reference [34]. However, these expressions prove to be over-complications for this purpose and experimental values for T1 and T2 of pure water are used. The experimental data from Table 1.2 for T1 (in ms) is plotted in Fig. 1-12 along with the experimental datapoints.

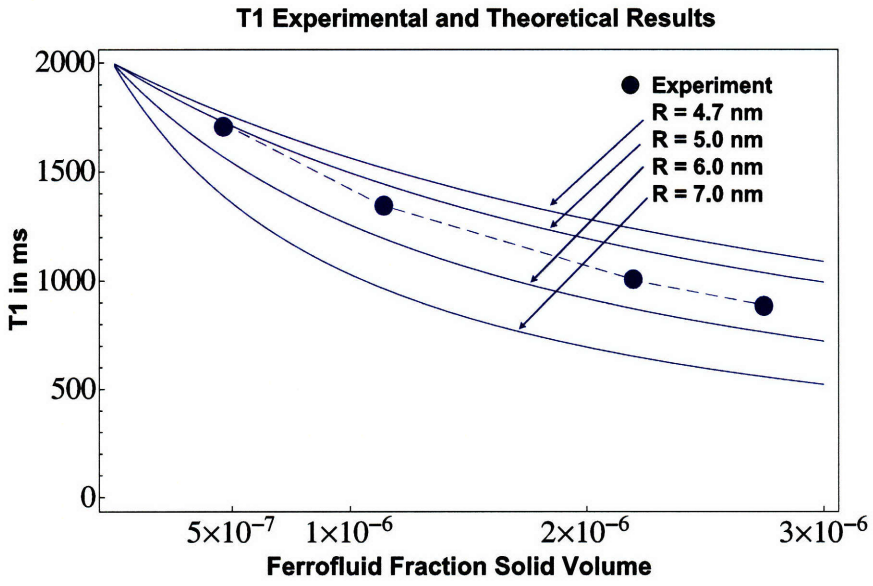

Figure 1-12: Experimental results for T1 (given in ms) over a range of MSG W11 ferrofluid concentrations measured by the unitless fraction solid volume, ϕ.

It turns out that an accurate prediction of the theoretical T1 value from the combination of T1 for pure water and the prediction of Eq (1.17) replicates the experimental analysis when the T1 relaxation time for water is 2000 ms. This is the value used in Figure 1-12. Since the T1 contribution from the ferrofluid grows rapidly at reasonable imaging frequencies so as to soon become insignificant compared to the contribution due to the intrinsic T1 from the water's dipole-dipole interactions (this

is clearly seen from the plots of Fig. 1-9), T1 is of lesser interest when considering ferrofluid as a contrast agent for MRI since the percentage change in T1 is modest compared to the effect of the SPIO particles on T2 (as will be shown in Figure 1-13). Nonetheless, the effect of T1 shortening, even for dilute solutions, is not negligible. This is clearly seen from the results of Table 1.2 and in the plots of Figure 1-12. However, since the effects on T2 are more pronounced (*i.e.*, comparable to those from pure water), superparamagnetic solutions are generally considered T2-contrast agents.

1.6.3 Significance of T2 and Theoretical Approximations

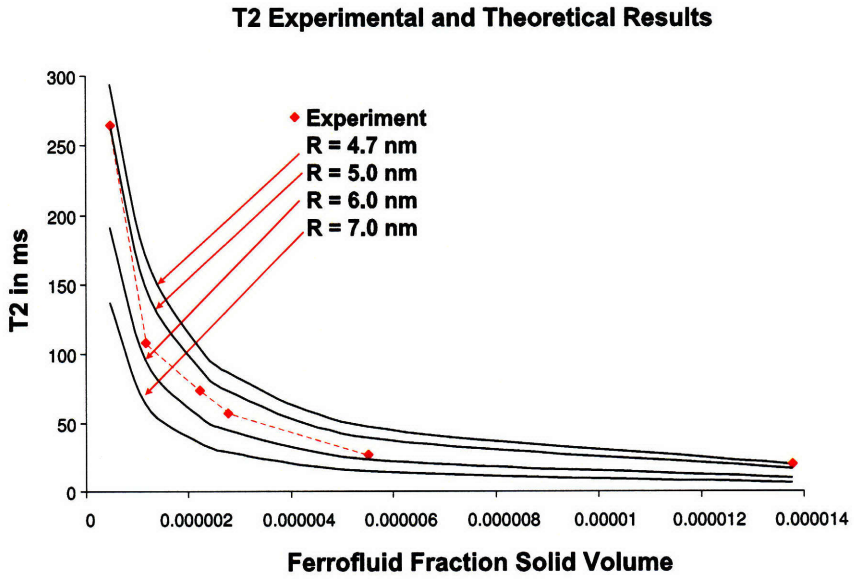

Figure 1-13: Comparison of the theoretical prediction for T2 at various superparamagnetic particle radii with the experimental results over a range of MSG W11 ferrofluid concentrations measured by the unitless fraction solid volume, ϕ.

In estimating T2 from theoretical analysis, the relaxation contribution due to the pure water acting alone was chosen to be 570 ms in accordance with our recorded experimental result. The value for T2 due to the ferrofluid alone was calculated over a range of particle radii and the combined result, as given by Eq. (1.16) is plotted in Fig. 1-13 versus ferrofluid concentration. Also included in the figure are the experimental values for T2 in the solution over the same concentration range for an expected mean particle radius in the range of 2.2 to 6.2 nm as measured by Elborai [44] and He [45] using transmission electron microscopy. From inspection of Fig. 1-13, a number of observations are notable:

- The value for the particle radius from Figures 1-12 and 1-13 appears to agree closely with the upper end of the particle radius range measured by Elborai and He [44,45]. This is expected since it is the largest particles which will dominate the T1 and T2 relaxation times. Larger particles tend to have shorter relaxation times and hence, due to the parallel nature of the contributions from particles of different radii, it is these shorter relaxation times which will dominate the final T1 and T2 values. Indeed, T1 and T2 measurements would appear to be a robust measure of the particle radius, R as evidenced by the results shown here.

- The experimental result at a concentration of 1.4×10^{-5} would appear to be somewhat outlying. This is to be expected since at very high concentrations the ferrofluid image on the MRI appears so dark that accurate determination of the mean signal intensity is difficult and the SNR suffers significantly.

- The values of theoretical T2 are found to have little frequency dependence at traditional Larmor imaging frequencies. This follows from Fig. 1-10 where, depend-

ing on particle radius, at Larmor frequencies beyond approximately 100 MHz, the contribution to T2 due to the ferrofluid is almost independent of frequency. Accordingly, it is sometimes deemed satisfactory [12] to ignore this frequency dependence entirely and approximate T2 from the ferrofluid by the high-frequency limit of Eq. (1.18) given by Eq. (1.24) where the Langevin function approaches unity and all of the power spectral density functions approach zero except for $J_0(\omega_0, \tau_d, \tau \rightarrow \infty)$ which approaches unity. At 1.5 T, this is not an entirely accurate approximation as can be seen from inspection of the plots of Fig. (1-10), which are not quite independent of frequency at the corresponding Larmor frequency.

$$1/T2 \approx \frac{4 \times 10^4 \mu_0^2}{135\pi} \gamma^2 N_A C \mu_m^2 \frac{\tau_d}{d^3} \tag{1.24}$$

Chapter 2

Transverse Field Excitation

The purpose of this chapter is to explore the feasibility of inducing spin-velocity in a ferrofluid while in MRI. To do this, an external field, in addition to those currently available in MRI, is introduced and its effect on the magnetization of the ferrofluid is examined. The external field is transverse to the B_0 field that characterizes MRI systems.

2.1 Introduction

Fundamental to MRI are three applied magnetic flux densitites: a strong, homogenous z-directed DC field, B_0; an RF field, B_1; and spatially-varying encoding fields or gradients, G. The B_0 field (1.5 T or 3 T for the most common clinical systems) induces polarization of nuclear spins, the much weaker ($\sim$0.01 mT) and transient ($\sim$ms) B_1 field is used to drive the induced z-directed magnetization into a transverse xy component for imaging, and the gradients ($\sim$10 mT/m) are DC fields used to spatially encode the transverse magnetization during relaxation to a resting state ($\sim$ 10ms). Under the large B_0 field of conventional clinical MRI systems, it is expected (based

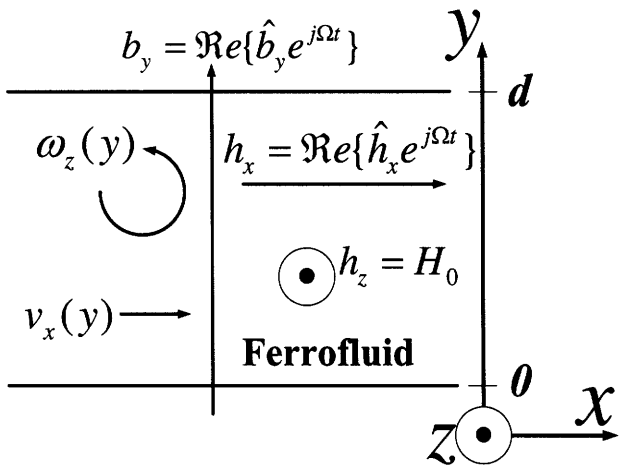

Figure 2-1: A planar ferrofluid layer between rigid walls at $y = 0, d$, is magnetically stressed by a uniform DC z-directed magnetic field H_0, an x-directed magnetic field of complex amplitude $\tilde{h}_x$ and a y-directed magnetic flux density of complex amplitude $\tilde{b}_y$. The x and y components vary sinusoidally at frequency Ω. The walls are of infinite extent along the x and z axes and there is no ferrofluid outside the channel.

on Fig. 1-2) that the equilibrium magnetization of a water-based ferrofluid would be saturated and virtually all the magnetic particles in the suspension would rigidly align with B_0. However, low-field MRI platforms exist, typically employed for better patient access or intervention by physicians during scanning. Commercial low-field MRI scanners operate typically at 0.2 T or 0.35 T, and this is the field-range examined in the work that follows. With this lower B_0, it is shown that ferrofluid saturation is not complete as determined by the Langevin relation for magnetic suspensions [42] and ferrofluid particle spin is indeed possible. In our analysis, we derive the expression for the ferrofluid spin velocity, $\boldsymbol{\omega}$ induced by adding a fourth field component, B_e, to a conventional MRI. Here, we assume B_e to be a rotating field applied in either the transverse $\{xy\}$ plane or the longitudinal $\{yz\}$ plane such that one component of the rotating field is collinear with the z-directed B_0. A simple but important channel geometry introduced by Zahn and Greer [47] and shown in Fig. 2-1 is employed,

which allows for the imposition of boundary conditions on both magnetic fields and fluid flow. For the first case to be considered in this chapter, both B_e and B_1 are transverse, rotating fields and the rotation frequency of B_1 is proportional to B_0 as given by (2.1), where γ is the gyromagnetic ratio of the nucleus under study, which for conventional MRI is the ^{1}H proton with $\gamma = 42.58$ MHz T^{-1}.

$$f_1 = \gamma B_0 \tag{2.1}$$

This work examines a wide range of rotation frequencies for B_e including those typical of f_1 in open MRI systems (8.5 MHz for 0.2 T and 14.9 MHz for 0.35 T). However, the amplitude of B_e is set between 1% and 10% of B_0, which is much larger than typical B_1 amplitudes. Modulation of the transverse magnetization is achieved by selecting the transverse B_e excitation frequency, termed Ω, to be of the same order as the reciprocal of the ferrofluid relaxation time τ. For typical SPIO nanoparticles, τ is on the order of 1 μs, (see Fig. 1-2).

A novel linearization of the Langevin relation for magnetic fluid suspensions is presented for small signal field variations around the operating point determined by the B_0 field. Having established this linearization, the scenario of a concurrent B_0 and transverse rotating B_e field is examined. In addition to this relatively simple case of magnetic field-driven spin-velocity, two flow-driven regimes for spin-velocity modulation are examined for the channel geometry shown in Fig. 2-1. The first considers Couette-imposed flow [105] where the upper channel plate moves at a constant linear velocity U_c, transverse to B_0. The second regime is the more common Poiseuille flow [105] where fluid flow is due to an x-directed pressure differential across the channel. Two critical parameters of interest in the MRI environment are examined in all cases. These are the ferrofluid spin-velocity in the channel and the resultant

modulation of the transverse fluid magnetization that arises in the channel due to the simultaneous relaxation and realignment of the magnetic nanoparticles with the applied transverse rotating field. Results for both quantities are examined over a wide range of parameters for magnetic nanoparticles with physical characteristics typical of SPIO agents used in MRI.

2.2 Theory

2.2.1 Governing Equations

The geometry shown in Fig. 2-1 follows the analysis of Zahn and Greer [47] and is carefully selected to allow the imposition of fields along all three axes.

Magnetization Constitutive Law

The magnetization relaxation equation for a ferrofluid under the action of a rotating magnetic field, thereby undergoing simultaneous magnetization and reorientation with the applied field, is given by (2.2). The fluid linear flow velocity vector is $\boldsymbol{v}$, the ferrofluid spin-velocity vector is $\boldsymbol{\omega}$ and the ferrofluid relaxation time [42] is τ.

$$\frac{\partial \mathbf{M}}{\partial t} + \boldsymbol{v} \cdot \nabla \mathbf{M} - \boldsymbol{\omega} \times \mathbf{M} + (\mathbf{M} - \mathbf{M}_{eq})/\tau = 0 \tag{2.2}$$

For the planar geometry shown in Fig. 2-1, the flow velocity can only be x-directed and the spin-velocity can only be z-directed. Both quantities may vary spatially along y.

$$\boldsymbol{v} = v_x(y)\boldsymbol{i}_x \tag{2.3}$$

$$\boldsymbol{\omega} = \omega_z(y)\boldsymbol{i}_z \tag{2.4}$$

Magnetic Fields

This analysis assumes the magnetoquasistatic limit so that the displacement current can be neglected. For typical poorly conducting fluids compared to typical metal conductivities, conduction currents can also be neglected if the skin-depth is much larger than a characteristic dimension of the ferrofluid. A water-based ferrofluid may have a conductivity, σ, of about 28×10^{-6} $(\Omega\,\mathrm{m})^{-1}$ [73]. Based on an excitation frequency of 850 kHz and $\mu = 2\mu_0$ (both typical of the analysis which follows), the skin depth, given by Eq. (2.5) is shown to be 2 orders of magnitude greater than any length dimension characteristic of this analysis (where d is on the order of 4 cm).

$$\delta = \sqrt{\frac{2}{\omega\,\mu\,\sigma}}$$

$$\delta \approx 1 \times 10^{2}\ \mathrm{m} \tag{2.5}$$

Under such conditions Ampere's Law approximately reduces to Eq. (2.6).

$$\nabla \times \mathbf{H} = \mathbf{0} \tag{2.6}$$

In this case, the magnetic field intensity can be rewritten [43] as the gradient of a scalar potential, Ψ, as in Eq. (2.7).

$$\mathbf{H} = -\nabla\,\Psi \tag{2.7}$$

Gauss' Law, given in Eq. (2.8) requires the divergence of the magnetic flux density

to be identically zero.

$$\nabla \cdot \mathbf{B} = 0 \tag{2.8}$$

The constitutive relation for a magnetizable material, such as ferrofluid or water, is given by Eq. (2.9) where μ_0 is the permeability of free space and has the value of $4\pi \times 10^{-7}$ H·m^{-1}.

$$\mathbf{B} = \mu_0(\mathbf{H} + \mathbf{M}) \tag{2.9}$$

In water, which is diamagnetic and has a magnetic susceptibility of $\chi = -9 \times 10^{-6}$ at room temperature [93], it can be generally assumed that the magnetization vector, $\mathbf{M}$, is significantly smaller than the $\mathbf{H}$ field and the constitutive relation reduces to Eq. (2.10).

$$\mathbf{B} = \mu_0\mathbf{H} \tag{2.10}$$

Considering the geometric arrangement of Fig. 2-1, the imposed magnetic field intensities along $\boldsymbol{i}_x$ and $\boldsymbol{i}_z$ are spatially uniform with corresponding zero spatial derivatives. This follows from Ampère's Law which states that in the absence of any conductive or displacement current densities, the curl of the magnetic field intensity is necessarily zero, as given by (2.11). For the geometry of Fig. 2-1, this means that both the x and z components of magnetic field intensity are uniform since H_0 is invariant in space and there is no imposed H field along the y axis (*i.e.*, $\hat{h}_y = 0$) as given in (2.11).

$$\nabla \times \mathbf{H} = 0$$

$$\Rightarrow \frac{\partial H_0}{\partial y} - \frac{\partial \tilde{h}_y}{\partial z} = 0 \;\Rightarrow \frac{\partial H_0}{\partial y} = 0$$

$$\Rightarrow \frac{\partial \tilde{h}_x}{\partial z} - \frac{\partial H_0}{\partial x} = 0 \;\Rightarrow \frac{\partial \tilde{h}_x}{\partial z} = 0$$

$$\Rightarrow \frac{\partial \tilde{h}_y}{\partial x} - \frac{\partial \tilde{h}_x}{\partial y} = 0 \;\Rightarrow \frac{\partial \tilde{h}_x}{\partial y} = 0 \tag{2.11}$$

Similarly for the imposed magnetic flux density along $\boldsymbol{i}_y$ since Gauss' Law states that normal components of the **B** field are continuous, as given by (2.12). For Fig. 2-1, this means that the components of **B** field along the y axis are continuous since there are no imposed B components along x (*i.e.*, $\hat{b}_x = 0$) and the main, z-directed B_0 field is invariant in space.

$$\nabla \cdot \mathbf{B} = \frac{\partial \tilde{b}_x}{\partial x} + \frac{\partial \tilde{b}_y}{\partial y} + \frac{\partial B_0}{\partial z} = 0$$

$$\Rightarrow \frac{\partial \tilde{b}_y}{\partial y} = 0 \text{ since } \frac{\partial \tilde{b}_x}{\partial x} = \frac{\partial B_0}{\partial z} = 0 \tag{2.12}$$

In light of these observations, the total magnetic flux density **B** and the total magnetic field **H** is given by (2.13) and (2.14) respectively where $\tilde{h}_x$ and $\tilde{h}_y$ are now sinusoidally time-varying quantities and $\tilde{h}_z = 0$. Complex notation is used for convenience. The $\hat{}$ symbol denotes a complex amplitude, $\Re e$ signifies the real component of a complex quantity, Ω is the frequency of excitation in rad·s^{-1} and $\jmath = \sqrt{-1}$. The relationship between **B**, **H** and **M** is given by the familiar expression of (2.16).

$$\mathbf{B} = \Re e\{(\hat{b}_x(y)\boldsymbol{i}_x + \hat{b}_y\boldsymbol{i}_y)e^{\jmath\Omega t}\} + B_0\boldsymbol{i}_z \tag{2.13}$$

$$\mathbf{H} = \Re e\{(\hat{h}_x \boldsymbol{i}_x + \hat{h}_y(y)\boldsymbol{i}_y)e^{\jmath\Omega t}\} + H_0 \boldsymbol{i}_z \tag{2.14}$$

$$\mathbf{M} = \Re e\{(\hat{m}_x(y)\boldsymbol{i}_x + \hat{m}_y(y)\boldsymbol{i}_y)e^{\jmath\Omega t}\} + M_0 \boldsymbol{i}_z \tag{2.15}$$

$$\mathbf{B} = \mu_0(\mathbf{H} + \mathbf{M}) \tag{2.16}$$

The relationship between M_0 and H_0, the z-directed components of magnetization and magnetic field intensity respectively, has been established in (A.20). In seeking a solution for the instantaneous magnetization, the imposed fields $\hat{b}_y$ and $\hat{h}_x$ are assumed known. This follows from (2.11) and (2.12), where normal components of the B field and tangential components of the H field are continuous within the ferrofluid. The $\hat{b}_y$ field might be imposed by means of a U-shaped electromagnet with its poles at $y = 0$ and $y = d$. The magnetic field, $\hat{h}_x$, might be imposed using planar current sheets at the $y = 0$ and $y = d$ (equal in magnitude and opposite in direction) where the surface current density, $\mathbf{K_s}$, is given by Ampere's Law: $\nabla \times \mathbf{H} = \mathbf{K_s}$.

Substituting for $\mathbf{M}_{eq}$ from (A.17) through (A.20) and for $\mathbf{M}$ from (2.15) one can rewrite the x and y (transverse) components of (2.2) using (2.16) as given by (2.17) and (2.18).

$$\hat{m}_x = \frac{M_0}{H_0} \frac{(\jmath\Omega\tau + 1 + M_0/H_0)\hat{h}_x - (\omega_z\tau)\hat{b}_y/\mu_0}{(\jmath\Omega\tau + 1)(\jmath\Omega\tau + 1 + M_0/H_0) + (\omega_z\tau)^2} \tag{2.17}$$

$$\hat{m}_y = \frac{M_0}{H_0} \frac{(\omega_z\tau)\hat{h}_x + (\jmath\Omega\tau + 1)\hat{b}_y/\mu_0}{(\jmath\Omega\tau + 1)(\jmath\Omega\tau + 1 + M_0/H_0) + (\omega_z\tau)^2} \tag{2.18}$$

The only unknowns are the complex amplitudes of transverse magnetization $\hat{m}_x$

and $\hat{m}_y$ which are a function of the, yet undetermined, spin-velocity ω_z. The second term of (2.2), $\boldsymbol{v} \cdot \nabla \mathbf{M}$, does not contribute any terms since the flow velocity is along $\boldsymbol{i}_x$ and all small signal terms can only vary with y. In the absence of a small signal magnetic field along $\boldsymbol{i}_z$, the z-component of magnetization is constant and given by the equilibrium value of M_0. The magnetization of the ferrofluid in the presence of small-signal rotating magnetic fields gives rise to a torque which, in turn, is responsible for fluid motion causing a non-zero value for spin-velocity ω_z and flow velocity v_x. Non-zero ω_z and v_x results in a changed fluid magnetization. Therefore, as well as the ferrofluid relaxation, one should consider the mechanical equations of interest to arrive at a consistent solution for $\hat{m}_x$, $\hat{m}_y$ and ω_z.

Fluid Mechanics

Applying the principles of conservation of linear and angular momentum to an incompressible ferrofluid leads to the simplified expressions of (2.19) and (2.21) respectively [42, 48] where p' is the modified pressure along the channel, given by (2.20), p is the absolute pressure in Pa, g is the gravitational acceleration acting along $\boldsymbol{i}_y$ in $\mathrm{m{\cdot}s^{-2}}$, ρ is the ferrofluid mass density in $\mathrm{kg{\cdot}m^{-3}}$, ζ is the ferrofluid vortex viscosity in $\mathrm{N{\cdot}s{\cdot}m^{-2}}$, η is the dynamic shear viscosity of the ferrofluid in $\mathrm{N{\cdot}s{\cdot}m^{-2}}$ and $\mathbf{T}_m$ is the magnetic torque density given by (2.22) in $\mathrm{N{\cdot}m^{-2}}$. The expressions consider the situation of sinusoidal steady state with viscous dominated flow conditions (so that inertia is negligible) and the ferrofluid only responds to force and torque densities which have a time-averaged, non-zero component. Also ignored are the coefficients of shear and bulk viscosity (η' and λ') [42] discussed by Elborai [44] and He [45].

$$-\nabla p' + \mu_0(\mathbf{M}\cdot\nabla)\mathbf{H} + 2\zeta\nabla\times\boldsymbol{\omega} + (\zeta+\eta)\nabla^2\boldsymbol{v} = 0 \tag{2.19}$$

$$p' = p + \rho g y \tag{2.20}$$

$$\mathbf{T}_m + 2\zeta(\nabla\times\boldsymbol{v} - 2\boldsymbol{\omega}) = 0 \tag{2.21}$$

$$\mathbf{T}_m = \mu_0(\mathbf{M}\times\mathbf{H}) \tag{2.22}$$

Considering that, for the channel geometry of Fig. 2-1, fluid flow is only allowed in the x direction, (2.21) can be simplified and rewritten in (2.23) where the only non-zero components are along the z axis.

$$T_{m,z} + 2\zeta(-\frac{\partial v_x}{\partial y}) - 4\zeta\omega_z = 0 \tag{2.23}$$

After considering time averaging, denoted by $\langle\ \rangle$, the only remaining non-zero component of magnetic torque density for the system, now expressed in terms of the applied fields from (2.22), is given by (2.24) where * denotes the complex conjugate.

$$\langle T_{m,z}\rangle = \frac{\mu_0}{2}\Re e(\hat{m}_x\,\hat{h}_y^* - \hat{h}_x\,\hat{m}_y^*) \tag{2.24}$$

Considering (2.16), one can rewrite the time-averaged torque density in terms of the imposed fields and the complex transverse magnetization amplitudes.

$$\langle T_{m,z}\rangle = \frac{1}{2}\Re e(\hat{m}_x\,\hat{b}_y^* - \mu_0(\hat{h}_x + \hat{m}_x)\,\hat{m}_y^*) \tag{2.25}$$

Comparing (2.25) and (2.23), one can combine to find an expression that eliminates $T_{m,z}$ and is given by (2.26).

$$2\zeta\frac{\partial v_x}{\partial y} + 4\zeta\omega_z - \frac{1}{2}\Re e(\hat{m}_x\,\hat{b}_y^* - \mu_0(\hat{h}_x + \hat{m}_x)\,\hat{m}_y^*) = 0 \tag{2.26}$$

Considering (2.19), one should note that the second non-zero term, $\mu_0(\mathbf{M}\cdot\nabla)\mathbf{H}$, is the magnetic force density $\boldsymbol{F}_m$ associated with the ferrofluid. However for the geometric arrangement of Fig. 2-1, the field components can only vary with y so the only non-zero component of magnetic force density is y-directed and given by (2.28). Again, only the non-zero, time-averaged terms are retained. As previously, the ˜ symbol is used to denote the real-valued, time-varying, small signal field while the * symbol indicates the complex, small-signal amplitude.

$$F_{m,y} = \mu_0(\tilde{m}_x\frac{\partial\tilde{h}_y}{\partial x} + \tilde{m}_y\frac{\partial\tilde{h}_y}{\partial y} + \tilde{m}_z\frac{\partial\tilde{h}_y}{\partial z})$$

$$\Rightarrow F_{m,y} = \mu_0(m_y\frac{\partial h_y}{\partial y})$$

$$\langle F_{m,y}\rangle = \frac{\mu_0}{2}\Re e[\hat{m}_y^*\frac{\partial\hat{h}_y}{\partial y}]$$

$$\tilde{b}_y = \mu_0(\tilde{h}_y + \tilde{m}_y)$$

$$\Rightarrow \langle F_{m,y}\rangle = \frac{-\mu_0}{2}\Re e[\hat{m}_y^*\frac{\partial\hat{m}_y}{\partial y}] \tag{2.27}$$

Considering the chain rule of differentiation, (2.27) can be expressed as (2.28).

$$\langle F_{m,y} \rangle = -\frac{\mu_0}{4} \frac{\partial |\hat{m}_y|^2}{\partial y} \tag{2.28}$$

In light of the simplification of (2.28) one might write the non-zero components for (2.19) as given by (2.29) and (2.30). Conservation of linear momentum yields components along both $\boldsymbol{i}_x$ and $\boldsymbol{i}_y$, given by (2.29) and (2.30) respectively. There is no component along $\boldsymbol{i}_z$.

$$-\frac{\partial p}{\partial x} + 2\zeta \frac{\partial \omega_z}{\partial y} + (\zeta + \eta) \frac{\partial^2 v_x}{\partial y^2} = 0 \tag{2.29}$$

$$-\frac{\partial (p + \rho g y)}{\partial y} - \frac{\mu_0}{4} \frac{\partial |\hat{m}_y|^2}{\partial y} = 0 \tag{2.30}$$

$$\Rightarrow p + \rho g y + \frac{\mu_0}{4} |\hat{m}_y|^2 = \text{ constant} \tag{2.31}$$

Equations (2.17), (2.18), (2.26) and (2.29) now constitute a closed system of equations with 4 unknown quantities: spin-velocity, ω_z, flow velocity, v_x, and the two complex amplitudes of magnetization along $\boldsymbol{i}_x$ and $\boldsymbol{i}_y$, denoted $\hat{m}_x$ and $\hat{m}_y$, respectively. It is again noted that $\hat{b}_y$ and $\hat{h}_x$ are imposed uniform small-signal fields and therefore known. While (2.31) is an additional equation of interest which accounts for changes in fluid pressure, it does not govern fluid flow. However, (2.31) does provide a way to measure $\hat{m}_y$ from pressure measurements.

2.2.2 General Solutions

Field Driven Solution

Generalized analytical solutions are possible considering (2.17), (2.18), (2.26) and (2.29) when boundary conditions are defined. When both plates in Fig. 2-1 are fixed, the flow velocity is necessarily zero at the boundaries $y = 0$ and $y = d$.

From Maxwell's Equations, the relevant boundary conditions on the magnetic field components are given by Eq. (2.32) and Eq. (2.33) where $\boldsymbol{i}_n$ is the unit vector normal to the boundary in the second medium. $\mathbf{K}_s$ is the boundary surface current density in $\mathrm{A{\cdot}m^{-1}}$. The magnetic flux density and magnetic field intensity, given by $\mathbf{B}_1$ and $\mathbf{H}_1$ respectively, correspond to the fields on the inside of the ferrofluid region (*i.e.*, $0 < y < d$) in the first medium while $\mathbf{B}_2$ and $\mathbf{H}_2$ correspond to the fields outside the ferrofluid (*i.e.*, $y < 0$ and $y < d$). The surface currents at $y = 0$ and $y = d$ must be opposite in direction (x-directed surface current to generate a uniform z-directed field and z-directed surface current to generate a uniform x-directed field) so that the fields outside the ferrofluid region are zero. For the y-directed $\mathbf{B}$ field, the field is confined to the channel when the pole faces are located at $y = 0$ and $y = d$.

$$\boldsymbol{i}_n \cdot (\mathbf{B}_1 - \mathbf{B}_2) = 0 \tag{2.32}$$

$$\boldsymbol{i}_n \times (\mathbf{H}_1 - \mathbf{H}_2) = \mathbf{K}_s \tag{2.33}$$

In the absence of any imposed flow or pressure differential in the channel, the first term of (2.29) is zero. It it is not necessary to define boundary conditions on ω_z.

$$v_x(0) = v_x(d) = 0 \tag{2.34}$$

Additional boundary conditions for the field components follow the continuity law of electromagnetics such that normal components of $\mathbf{B}$ are continuous at the boundaries $y = 0$ and $y = d$, while the tangential components of $\mathbf{H}$ are determined by the surface current densities at the boundaries $y = 0$ and $y = d$. Integrating (2.29) with respect to y and some rearranging leads to (2.35) where C_1 is a constant of integration. For this solution, the pressure differential is not considered although the cases of an applied pressure differential are considered later.

$$\frac{\partial v_x}{\partial y} = -\frac{1}{\zeta + \eta}(C_1 + 2\zeta\omega_z) \tag{2.35}$$

Substituting from (2.35) for the derivative of v_x in (2.26) and solving for ω_z leads to (2.36).

$$\omega_z = \frac{\zeta + \eta}{8\eta\zeta}\Re e(\hat{m}_x\,\hat{b}_y^* - \mu_0(\hat{h}_x + \hat{m}_x)\,\hat{m}_y^*) + \frac{C_1}{2\eta} \tag{2.36}$$

Inspection of (2.36), where the expressions for $\hat{m}_x$ and $\hat{m}_y$ can be substituted from (2.17) and (2.18), shows no y dependence. It follows that ω_z is necessarily a constant in space, thereby also setting the second term in (2.29) to zero. Solving the remaining non-zero term of (2.29) by integration with respect to y (since ζ and η are both assumed non-zero) and applying the boundary conditions of (2.34) shows that the flow velocity in the channel is zero. C_2 and C_3 are constants of integration.

$$\frac{\partial^2 v_x}{\partial y^2} = 0 \tag{2.37}$$

$$\frac{\partial v_x}{\partial y} = C_2 \tag{2.38}$$

$$v_x(y) = C_2 y + C_3 \tag{2.39}$$

$$v_x(0) = v_x(d) = 0 \Rightarrow C_2 = C_3 = 0 \Rightarrow v_x(y) = 0 \tag{2.40}$$

Applying this result to (2.35), one can solve $C_1 = -2\zeta\omega_z$ and substituting for C_1 in (2.36), the spin-velocity ω_z is given in terms of $\hat{m}_x$ and $\hat{m}_y$.

$$\omega_z = \frac{1}{8\zeta}\Re e(\hat{m}_x\,\hat{b}_y^* - \mu_0(\hat{h}_x + \hat{m}_x)\,\hat{m}_y^*) \tag{2.41}$$

While (2.41), (2.17) and (2.18) do not facilitate closed form solutions for ω_z, $\hat{m}_x$, and $\hat{m}_y$, the equations were solved using *Mathematica 5.2* (Wolfram Research, Champaign, Illinois) and the results are included in the following section. It should be clear from (2.41) that in the absence of one or other of the x and y components of the applied small-signal magnetic field, the spin-velocity is zero.

Couette Flow Solution

The only difference between the case of an imposed Couette flow and the previous solution is the changed boundary condition at $y = d$ where $v_x(d) = U_c$ and U_c is the imposed linear velocity of the upper plate in $\mathrm{m{\cdot}s^{-1}}$. In addition to the imposed Couette flow, the applied rotating transverse field excitation remains present so that the spin-velocity is due to a combination of the magnetic driving field and fluid flow. There is no imposed pressure differential along $\boldsymbol{i}_x$ so the analysis is identical up until (2.35). However since the non-slip boundary condition at $y = d$ requires $v_x(d) = U_c$ this leads to a solution with $C_3 = 0$ and $C_2 = U_c/d$. Substituting into (2.35) one finds the revised form of (2.41) for imposed Couette flow conditions, given in (2.42).

$$\omega_z = \frac{1}{8\zeta}\Re e(\hat{m}_x\,\hat{b}_y^* - \mu_0(\hat{h}_x + \hat{m}_x)\,\hat{m}_y^*) - \frac{U_c}{2d} \tag{2.42}$$

Similar to the no-flow solution, (2.42), (2.17) and (2.18) were solved using *Mathematica 5.2* and the numerical results are presented.

Poiseuille Flow Solution

Poiseuille flow is achieved in the channel by means of an x-directed pressure differential which, in the absence of a magnetic torque density in the fluid, results in a parabolic flow profile with y. The imposed flow is, again, in addition to the rotating transverse field excitation due to B_e where B_e is the amplitude (in Tesla) of the rotating field excitation. This complicates the previous solution and leads to the expression of (2.48) after twice integrating (2.29) (repeated in (2.43)) with respect to y. The expression for $\frac{\partial \omega_z}{\partial y}$ is substituted from (2.25). Note that the first term of (2.29) is now non-zero, corresponding to the pressure drive. K_1 and K_2 are constants of integration while $\langle T_{m,z} \rangle$ is still given by (2.25).

$$-\frac{\partial p'}{\partial x} + 2\zeta \frac{\partial \omega_z}{\partial y} + (\zeta + \eta)\frac{\partial^2 v_x}{\partial y^2} = 0 \tag{2.43}$$

$$-\frac{\partial p'}{\partial x} + 2\zeta \left(\frac{1}{4\zeta}\frac{\partial T_{m,z}}{\partial y} - \frac{1}{2}\frac{\partial^2 v_x}{\partial y^2} \right) + (\zeta + \eta)\frac{\partial^2 v_x}{\partial y^2} = 0 \tag{2.44}$$

$$\Rightarrow -\frac{\partial p'}{\partial x} + \frac{1}{2}\frac{\partial T_{m,z}}{\partial y} + \eta \frac{\partial^2 v_x}{\partial y^2} = 0 \tag{2.45}$$

$$\Rightarrow -\frac{\partial p'}{\partial x} y + \frac{1}{2}\langle T_{m,z} \rangle + \eta \frac{\partial v_x}{\partial y} + K_1 = 0 \tag{2.46}$$

$$\Rightarrow -\frac{\partial p}{\partial x} y + \frac{1}{2}\langle T_{m,z} \rangle + \eta \frac{\partial v_x}{\partial y} + K_1 = 0 \tag{2.47}$$

$$\Rightarrow -\frac{\partial p}{\partial x}\frac{y^2}{2} + \frac{1}{2}\int_0^y \langle T_{m,z}\rangle dy + \eta v_x + K_1 y + K_2 = 0 \tag{2.48}$$

Applying the non-slip boundary conditions on v_x at $y = 0$ and d allows for the solution of K_1 and K_2.

$$v_x(0) = 0 \Rightarrow K_2 = 0 \tag{2.49}$$

$$v_x(d) = 0 \Rightarrow K_1 = \frac{d}{2}\frac{\partial p'}{\partial x} - \frac{1}{2d}\int_0^d \langle T_{m,z}\rangle dy \tag{2.50}$$

Substituting the results of (2.49) and (2.50) into (2.48) and rearranging one arrives at (2.51).

$$\frac{\partial v_x}{\partial y} = \frac{1}{2\eta}\frac{\partial p'}{\partial x}(2y - d) - \frac{1}{2\eta}\langle T_{m,z}\rangle + \frac{1}{2d\eta}\int_0^d \langle T_{m,z}\rangle dy \tag{2.51}$$

Substituting for the derivative of v_x given by (2.51) into (2.48) and substituting for K_1 and K_2 leads to an expression for ω_z which is independent of v_x and where $\langle T_{m,z}\rangle$ is given by (2.25).

$$\omega_z = -\frac{1}{4}\frac{\partial p'}{\partial x}(2y - d) + \langle T_{m,z}\rangle\frac{\eta + \zeta}{4\zeta\eta} - \frac{1}{4d\eta}\int_0^d \langle T_{m,z}\rangle dy \tag{2.52}$$

While (2.52) is not solvable analytically, it can be solved numerically and the results which follow use *ComsolMultiphysics* to do that. As an analytical check on the numerical solutions, some simplifications were examined. The first limit is when the pressure differential dominates and $\langle T_{m,z}\rangle$, the internal magnetic torque density after time-averaging, is zero. In such a scenario, ω_z is a maximum or minimum at $y = \{0, d\}$, where the sign depends on the direction of the pressure differential and

$\omega_z = 0$ at $y = d/2$. For x-directed flow, the differential is negative and ω_z is a positive maximum at $y = 0$ as given by (2.53).

$$\langle T_{m,z} \rangle = 0$$

$$\omega_z(y = 0) = -\omega_z(y = d) = \frac{d}{4\eta}\frac{\partial p'}{\partial x} \tag{2.53}$$

Similarly for v_x which has a maximum value at $y = d/2$ given by (2.54). In the results which follow, this maximum velocity is denoted U_p.

$$\langle T_{m,z} \rangle = 0$$

$$v_x(d/2) = -\frac{d^2}{8\eta}\frac{\partial p'}{\partial x} = U_p \tag{2.54}$$

As with the field-driven and Couette-imposed flow conditions, spin-velocity and transverse magnetization are solved and plotted under varying physical parameters of interest.

2.3 Results

2.3.1 Physical Parameters

The physical ferrofluid parameters are selected for application of SPIO agents in a 0.1-0.35 T MRI scanner with SPIO concentrations, ϕ, varying between 3% and 0.003%. This lower end value of $\phi = 0.003\%$ is still over an order of magnitude beyond the recommended dosage of Feridex, the only FDA-approved SPIO agent, after it becomes diluted in the subject's bloodstream (see Table B.1 of Appendix B). The non-varying parameters are included in Table 2.1. Nominal values are included for B_0, B_e, f,

Table 2.1: Table of Nominal Physical Parameters

Symbol	Value	Quantity
B_0	0.2	Main Flux Density in T
H_0	B_0/μ_0	Main Field Intensity in water in $\mathrm{A{\cdot}m^{-1}}$
B_e	5% of $B_0 = -j\hat{b}_y$	Rotating Flux Density Amplitude in T
H_e	$B_e/\mu_0 = \hat{h}_x$	Rotating Field Intensity in water in $\mathrm{A{\cdot}m^{-1}}$
μ_0	$4\pi \times 10^{-7}$	Permeability of free space in $\mathrm{H{\cdot}m^{-1}}$
R	4×10^{-9}	Mean particle radius in m
V_p	$4/3\,\pi R^3$	Magnetic particle volume in $\mathrm{m^3}$
f	$1/(2\pi\tau)$	Frequency of transverse B_e field rotation in Hz
Ω	$2\pi f$	Frequency of magnetic field rotation $\mathrm{rad{\cdot}s^{-1}}$
ϕ	0.03	Ferrofluid volume fraction of solids
α_0	$M_d\,V_p\,\mu_0\,H_0/(kT)$	Equilibrium Langevin Parameter
M_0	$M_s\,L(\alpha_0)$	Equilibrium Ferrofluid Magnetization in $\mathrm{A{\cdot}m^{-1}}$
M_d	446×10^3	Single-domain magnetization (Fe_3O_4) in $\mathrm{A{\cdot}m^{-1}}$
M_s	ϕM_d	Saturation magnetization of ferrofluid in $\mathrm{A{\cdot}m^{-1}}$
τ	10^{-6}	Ferrofluid Time Constant in s
η	0.00202	Ferrofluid Kinematic Viscosity in Pa·s [44] [45]
ζ	$1.5\,\eta\,\phi$	Ferrofluid Vortex Viscosity in Pa·s [42]
T	295	Absolute temperature in K
k	1.381×10^{-23}	Boltzmann Constant in $\mathrm{JK^{-1}}$
d	0.005	Channel width in m
U_c	1	Top plate velocity (Couette flow) in $\mathrm{m{\cdot}s^{-1}}$
U_p	1	Maximum flow velocity (Poiseuille flow) in $\mathrm{m{\cdot}s^{-1}}$

ϕ, U_c, and U_p although the effect of varying these values is investigated. U_c denotes the velocity of the upper plate under conditions of Couette flow while U_p denotes the maximum imposed inflow velocity under conditions of Poiseuille flow.

The main DC B_0 field is directed along $\boldsymbol{i}_z$. A rotating field of angular frequency, Ω, and constant amplitude is generated in the transverse xy plane by setting $\hat{h}_x = H_e$

and $\hat{b}_y = jB_e$ where B_e and H_e are real-valued quantities. The resultant transverse field rotates in an clockwise sense about the z axis. The magnetic particle properties are typical of those used as superparamagnetic contrast agents in MRI [27], [59], [64]. The magnetic core is assumed to be magnetite (Fe_3O_4). The frequency of excitation, denoted Ω, of the transverse rotating field varies but is normalized with respect to the ferrofluid time constant τ, as is the spin-velocity ω_z in the resulting plots. The ferrofluid kinematic viscosity, η, is that recorded by He [45] using 3% solid volume *MSG-W11* ferrofluid from the *Ferrotec Corporation*, Bedford, New Hampshire.

The effect of varying the physical system parameters is examined for the normalized spin-velocity $\omega\tau$ and the magnitude and lag angle (denoted *phase*) of the instantaneous transverse magnetization $|M_{trans}(t)|$. Since the imposed transverse field is circularly polarized in xy, one expects that the transverse magnetization will also be circularly polarized in xy. Referring to (2.15) one can write $M_{trans}(t)$ as given by (2.55). For non-dimensionalized plotting, the transverse magnetization is normalized with respect to B_e by dividing by B_e/μ_0.

$$M_{trans}(t) = \Re e\{(\hat{m}_x \boldsymbol{i}_x + \hat{m}_y(x)\boldsymbol{i}_y)e^{j\Omega t}\} \tag{2.55}$$

For simplicity, the instantaneous magnitude is evaluated at time $t = 0$ so that $|M_{trans}(0)|$ is given by (2.56).

$$|M_{trans}(0)| = \sqrt{(\Re e(\hat{m}_x))^2 + (\Re e(\hat{m}_y))^2} \tag{2.56}$$

The phase, which represents the lag angle between the rotating transverse field

and the ferrofluid magnetization vectors is given by (2.57).

$$Phase\ of\ M_{trans} = \text{ArcTan}\left(\frac{\Re\text{e}(\hat{\text{m}}_\text{y})}{\Re\text{e}(\hat{\text{m}}_\text{x})}\right) \tag{2.57}$$

2.3.2 Field-Driven Results

The conditions of field-driven excitation are simulated and the effect of changing B_0, B_e and ϕ on both the normalized spin velocity $\omega_z\tau$ and the instantaneous transverse magnetization, normalized with respect to B_e are investigated. The results are shown in Figs. 2-2 and 2-3 respectively. The plots are achieved using *Mathematica 5.2* with reference to (2.17), (2.18) and (2.41). In all cases, the x-axis is the normalized transverse rotating field frequency $\Omega\tau$.

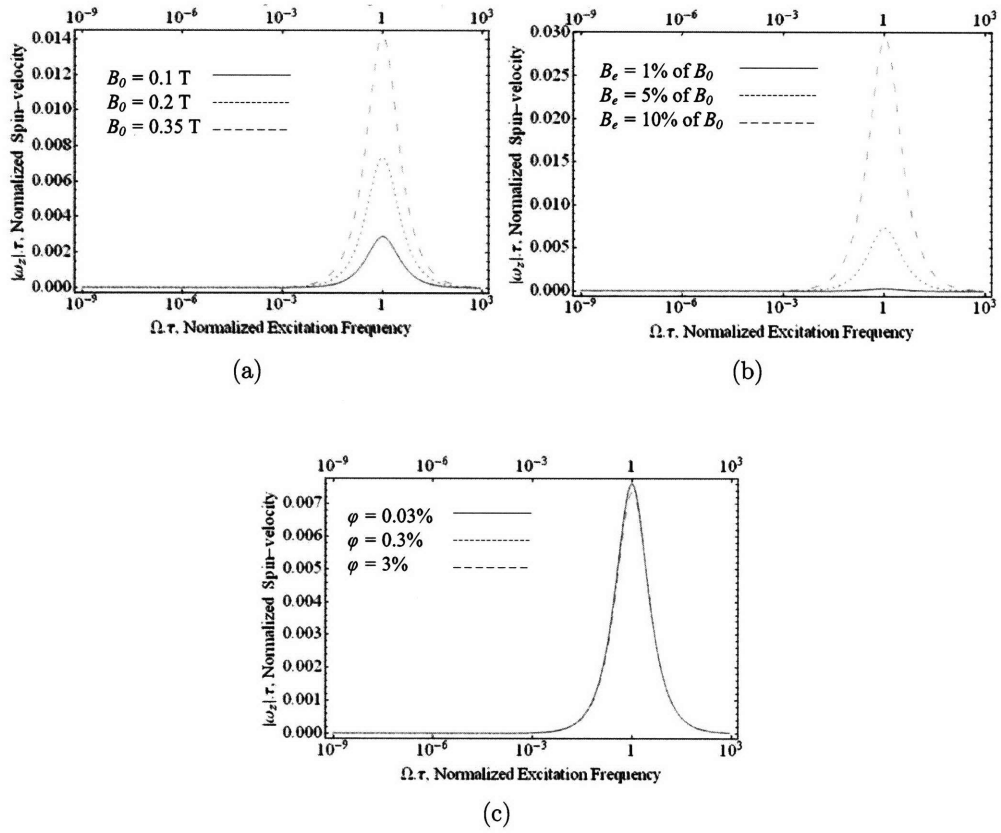

Figure 2-2: Frequency dependence of $|\omega_z|\tau$ on (a) B_0 (b) B_e and (c) ϕ is presented in the presence of rotating field excitation and the absence of any imposed fluid flow. Unless otherwise noted $B_0 = 0.2$ T in (b) and (c), $B_e = 5\%$ of B_0 in (a) and (c), and $\phi = 3\%$ in (a) and (b). Note that for $\tau = 1\,\mu$s, $\Omega/(2\pi) \approx 160$kHz.

2.3.3 Couette Flow Results

Couette flow is imposed by allowing the upper plate at $y = d$ to move with linear velocity U_c. As for the previous case where the spin-velocity is due only to field-driven excitation, the effect of changing B_0, B_e and ϕ on both $\omega_z\tau$ and normalized M_{trans} is investigated and results are shown in Figs. 2-4 and 2-5 respectively. Now, the spin-velocity is due to the combined effects of imposed field and flow on the ferrofluid. The result of imposed Couette flow is a uniform, z-directed spin-velocity

in the channel. The resultant transverse magnetization is also uniform in space. The effect of changing the maximum top-plate linear velocity, U_c, on $\omega_z\tau$ and normalized M_{trans} is investigated and the results are included in Figs. 2-4(d) and 2-5(g) and (h).

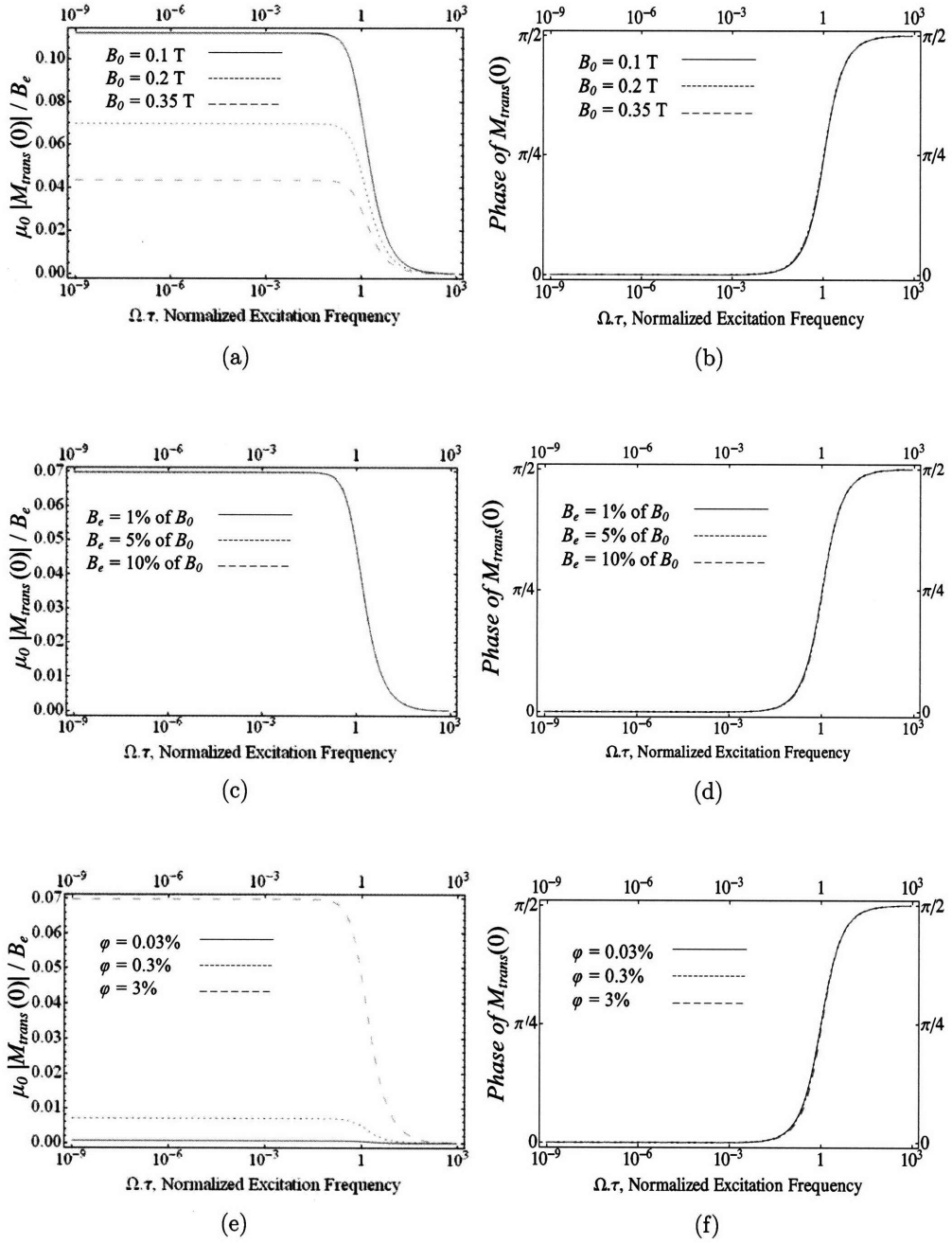

Figure 2-3: Frequency dependence of normalized, instantaneous, transverse magnetization, both magnitude and phase of $M_{trans}(0)$ at time t=0 on (a),(b) B_0 (c),(d) B_e and (e),(f) ϕ is presented in the presence of rotating field excitation and the absence of any imposed fluid flow. Unless otherwise noted $B_0 = 0.2$ T in (c)-(f), $B_e = 5\%$ of B_0 in (a),(b),(e) and (f), and $\phi = 3\%$ in (a)-(d).

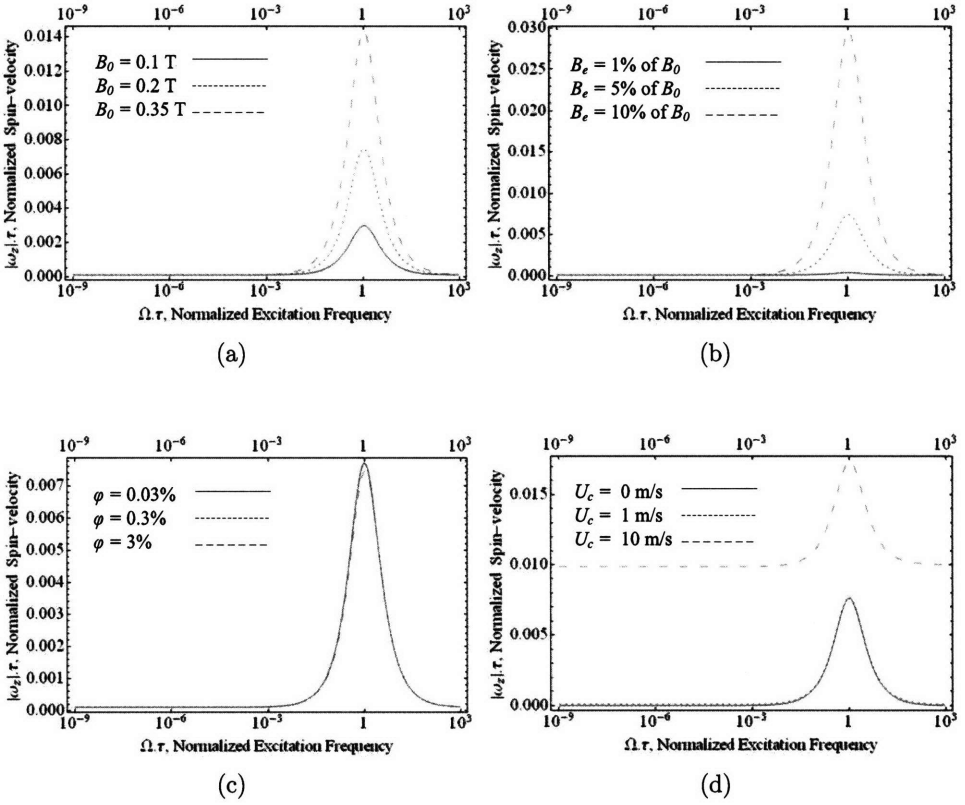

Figure 2-4: Frequency dependence of $|\omega_z|\tau$ on (a) B_0 (b) B_e (c) ϕ and (d) U_c is presented under conditions of Couette flow. Unless otherwise noted $B_0 = 0.2$ T in (b)-(d), $B_e = 5\%$ of B_0 in (a), (c) and (d), $\phi = 3\%$ in (a), (b) and (d), and $U_c = 1$ m/s in (a)-(c). Note that for $\tau = 1\,\mu$s, $\Omega/(2\pi) \approx 160$kHz.

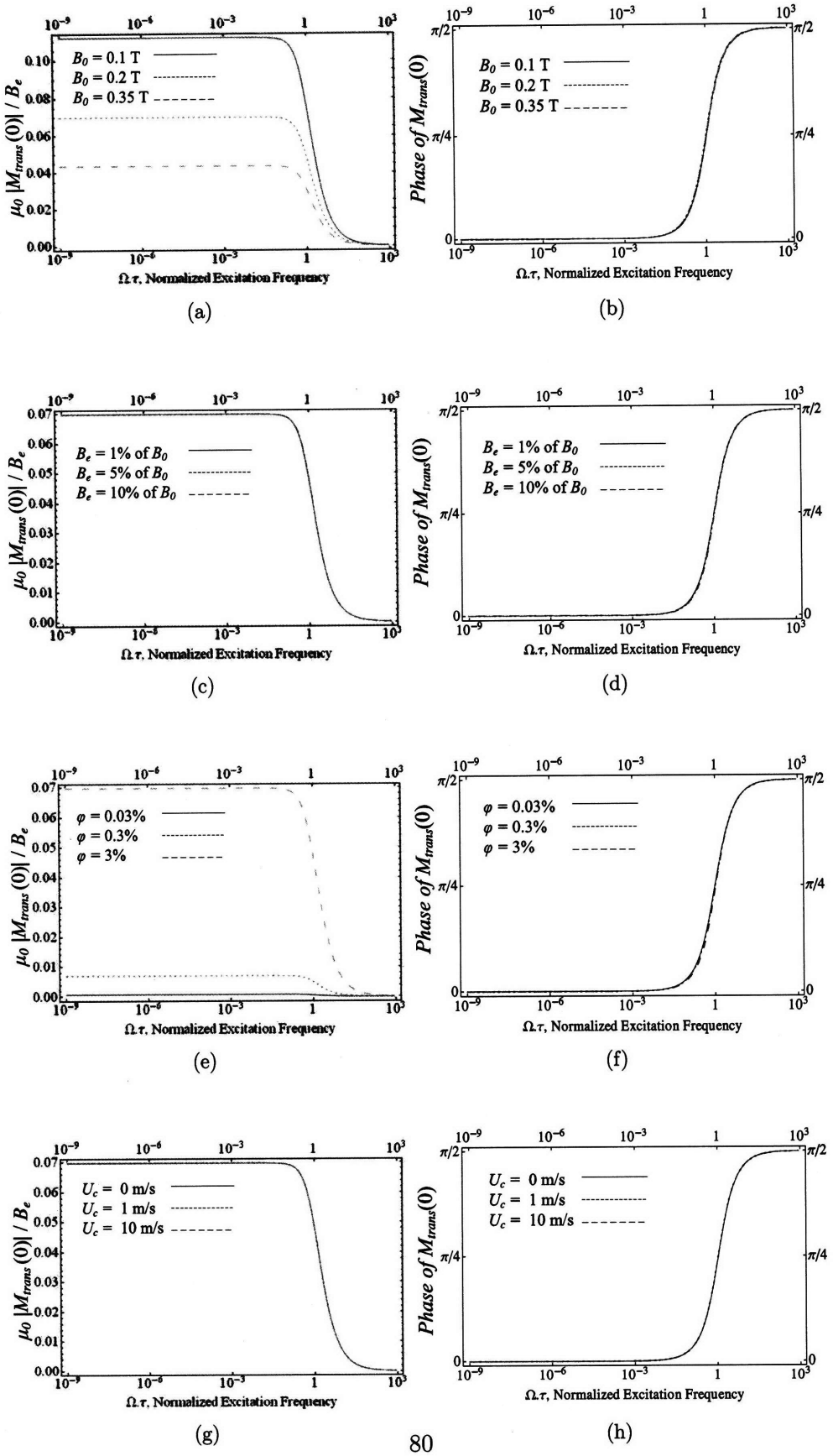

Figure 2-5: Frequency dependence of normalized, instantaneous, transverse magnetization, both magnitude and phase of $M_{trans}(0)$ at time t=0 on (a),(b) B_0 (c),(d) B_e (e),(f) ϕ and (g),(h) U_c is presented under conditions of Couette flow. Unless otherwise noted $B_0 = 0.2$ T in (b)-(d), $B_e = 5\%$ of B_0 in (a), (c) and (d), $\phi = 3\%$ in (a), (b) and (d), and $U_c = 1$ m/s in (a)-(c).

2.3.4 Poiseuille Flow Results

For ease of comparison with the case of Couette flow, Poiseuille flow conditions are implemented by means of an imposed parabolic flow profile on the left-most entry to the channel of Fig. 2-1 rather than defining the imposed pressure differential across the channel. This approach allowed the maximum flow velocity in the channel to be defined in each case, U_c for Couette flow conditions and U_p for Poiseuille flow conditions. Finite element simulation and solution of the variables in the channel is achieved using *Comsol Multiphysics* from Comsol Inc., Burlington, Massachusetts where (2.17) through (2.22) are the equations of interest. Boundary conditions on the upper and lower plates are given by (2.34) as is the case for no imposed flow. Inlet flow (defined from the left side) is x-directed and defined by the parabolic distribution of (2.58) where d is the channel width while the outlet boundary condition defines the pressure $p = 0$.

$$v_{in,x}(y) = \frac{4U_p y(y-d)}{d^2} \tag{2.58}$$

The result of the imposed parabolic flow profile in the channel is that the spin-velocity is no longer spatially invariant as in the previous cases. The total spin-velocity in the channel is now the sum of contributions from the Poiseuille imposed flow condition and $\langle T_{m,z} \rangle$. Since the flow-induced spin-velocity changes sign as y varies from 0 to d along the channel width, the two contributions will sum on one side of $y = d/2$ and subtract on the other. At $y = d/2$, the spin-velocity is zero. For the geometry of Fig. 2-1, where flow is directed along $+\boldsymbol{i}_x$, the contributions to ω_z from the imposed rotating field, $B_e > 0$, and that due to Poiseuille flow, add at the lower plate and subtract at the top so that the maximum value of $|\omega_z|\tau$ occurs at $y = 0$. It is this lower plate velocity which is plotted in the results of Fig. 2-6. Similarly, the instantaneous transverse magnetization in the channel is no longer spatially invariant as in the prior

cases but varies with y. Again, the maximum instantaneous value is plotted in the results of Fig. 2-7 and in all cases, the x-axis is the normalized transverse rotating field frequency $\Omega\tau$. As for the previous cases, the effect of changing B_0, B_e, ϕ, and U_p is investigated for both $\omega_z\tau$ and normalized M_{trans} and the results are shown in Figs. 2-6 and 2-7. Unlike the previous cases, analytical solutions are not possible so, instead, numerical solutions are presented at discrete points along the $\Omega\tau$ axis. The phase plots are not included but follow closely those for Couette flow.

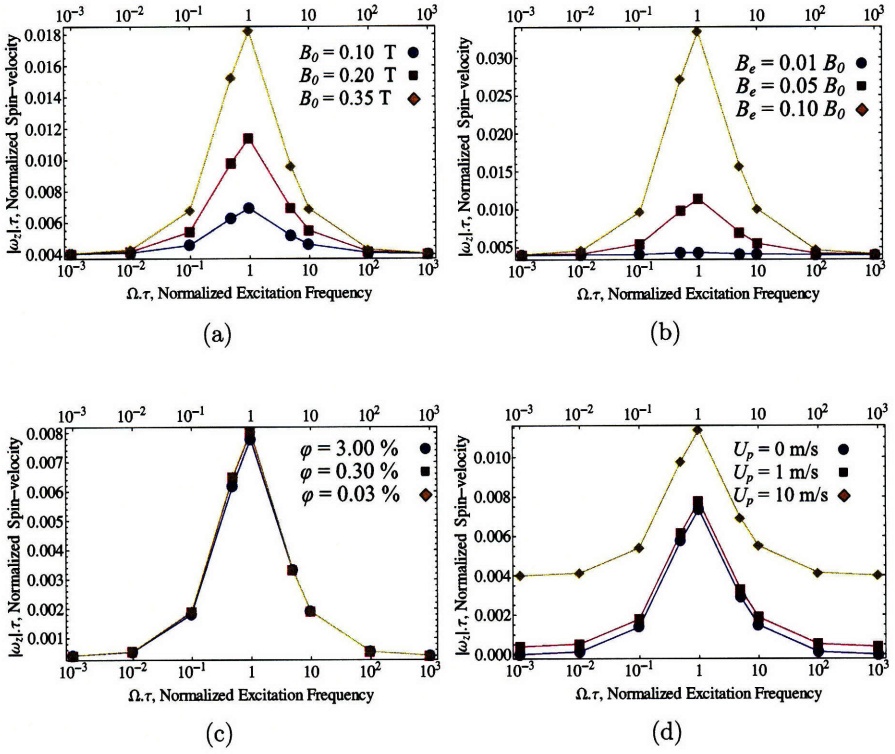

Figure 2-6: Frequency dependence of $|\omega_z|\tau$ on (a) B_0 (b) B_e (c) ϕ and (d) U_p is presented under conditions of Poiseuille flow. Unless otherwise noted $B_0 = 0.2$ T for (b)-(d), $B_e = 5\%$ of B_0 for (a), (c) and (d), $\phi = 3\%$ for (a), (b) and (d), and $U_p = 1$ m/s for (a)-(c). Note that for $\tau = 1\,\mu$s, $\Omega/(2\pi) \approx 160$kHz.

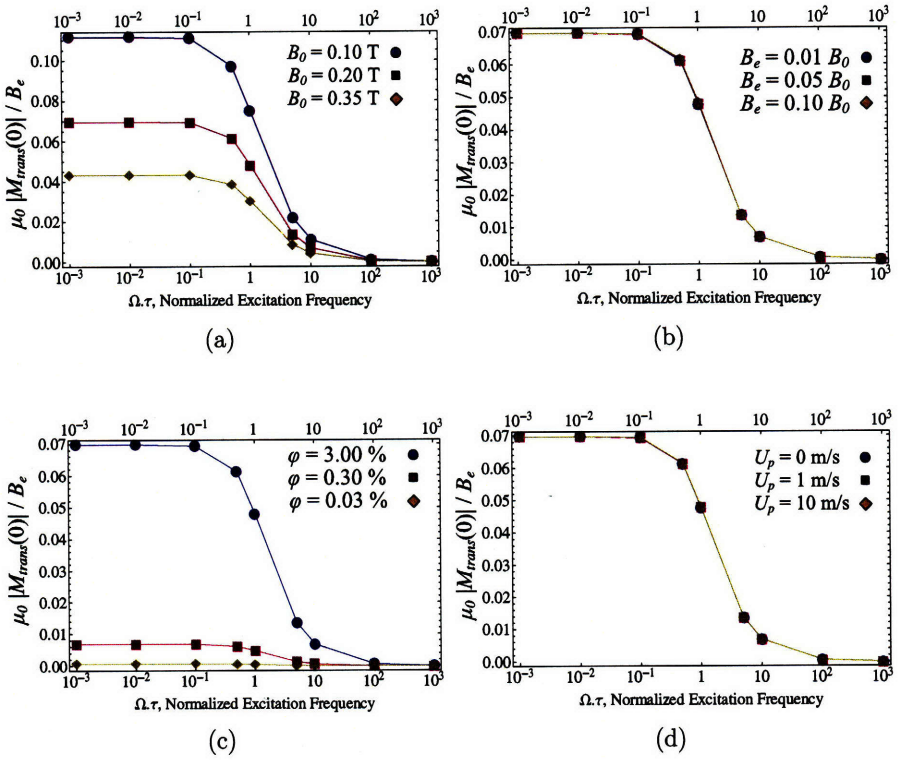

Figure 2-7: Frequency dependence of normalized, instantaneous, transverse magnetization's magnitude $|M_{trans}|$ on (a) B_0 (b) B_e (c) ϕ and (d) U_c is presented under conditions of Poiseuille flow. Unless otherwise noted $B_0 = 0.2$ T for (b)-(d), $B_e = 5\%$ of B_0 for (a), (c) and (d), $\phi = 3\%$ for (a), (b) and (d), and $U_p = 1$ m/s for (a)-(c).

2.4 Discussion

2.4.1 Spin-velocity dependence on rotating field frequency Ω

The dependence of the ferrofluid spin-velocity, ω_z, is closely related to the ferrofluid time constant, τ, as should be expected from the expressions of (2.17) and (2.18) since $\omega_z\tau$ is a term that appears in both the numerator and denominator of each expression. For low-frequencies where $\Omega\tau \ll 1$ and $\omega_z\tau \ll 1$, the effect of spin-velocity on the ferrofluid's transverse magnetization is negligible. Physically this low-frequency limit corresponds to a ferrofluid with a small-signal transverse susceptibility given by M_0/H_0 and the instantaneous transverse **M** and **H** vectors are collinear.

As $\Omega\tau$ approaches unity, the spin-velocity becomes increasingly significant. For example, as seen in Fig 2-2(a), the value of ω_z is negligible until $\Omega\tau \approx 1$ and then approaches a maximum of 1.4×10^3 rad/s for $B_0 = 0.35$ T, at $\Omega\tau = 1$. This is because the ferrofluid time constant τ is no longer fast enough to allow the particles to reestablish transverse equilibrium before the excitation changes direction, due to the rotating transverse field. Instead, synchronism is maintained at a constant lag angle between the transverse components of **M** and **H** for a particular rotating field frequency Ω. The lag angle, plotted, in the absence of any imposed pressure differential, in Figures 2-3(b), (d), (f) and (h) for varying parameters, has a value of $\pi/4$ when $\Omega\tau \approx 1$. Mathematically, this is shown by the on-axis magnetization (both $\hat{m}_x$ and $\hat{m}_y$) given by (2.17) and (2.18) becoming increasingly dependent on the orthogonal transverse field component, $\hat{h}_x$ for the case of $\hat{m}_y$ and $\hat{b}_y$ for the case of $\hat{m}_x$. This cross-coupling results in a non-symmetric, small-signal transverse susceptibility, which relates the instantaneous transverse magnetization M_{trans} to the applied transverse rotating field due to $\hat{h}_x$ and $\hat{b}_y$, denoted H_{trans}, causing M_{trans} to lag H_{trans} as previously noted.

In the high-frequency limit, where $\Omega\tau \gg 1$, the lag angle between M_{trans} and H_{trans} approaches $\pi/2$, as plotted in Figure 2-3 and the denominators of (2.17) and (2.18) become the dominant terms. The spin-velocity is less significant in the transverse magnetization and in the limit of $\Omega\tau \gg 1$, the transverse magnetization disappears entirely so that the ferrofluid no longer appears magnetic in the transverse xy plane. It is noted that this scenario is very difficult to achieve in reality since the typical time constant of 1 μs requires $\Omega/(2\pi)$ on the order of 0.1 MHz before $\Omega\tau \gg 1$. Even more critical is the note from Shliomis [48] that his formulation is no longer valid in the frequency range of $\Omega\tau \gg 1$, where for $\tau \approx 1\mu$s, $\Omega/(2\pi)$ approaches tens of MHz. The plots should be treated with some skepticism beyond $\Omega\tau \approx 1$. The z-directed magnetization is not frequency dependent as previously noted and is given by (A.20) throughout.

2.4.2 Field-Driven Results

In the absence of externally imposed flow, the ferrofluid spin-velocity is spatially constant in the channel of Fig. 2-1. As noted, the maximum spin-velocity occurs when $\Omega\tau = 1$ and increases linearly with the main z-directed B_0 field, as shown in Fig. 2-2(a). The dependence on the rotating field amplitude B_e, shown in Fig. 2-2(b) is non-linear however. When B_e is increased relative to B_0, the relationship between ω_z and B_e is approximately quadratic. Dependence of spin-velocity on percentage solid volume ϕ, shown in Fig. 2-2(c), is minimal since spin-velocity is a volume-averaged quantity. The maximum spin velocity occurs, as expected when B_e is a maximum, 10% of B_0, although for none of the scenarios investigated does $\omega_z\tau$ approach unity. The instantaneous magnetization shows similar dependence to ω_z on B_0 and B_e, as seen from Figs. 2-3(a) and (c) although the effect of ϕ, shown in Fig. 2-3(e), is

pronounced where the normalized M_{trans} increases linearly with ϕ. Throughout the field-driven results, the value of transverse magnetization does not become comparable to B_e. Even for the conditions of Fig. 2-3(a) where $B_0 = 0.35$ T and $B_e = 5\%$ of B_0 the normalized magnetization is only 11% of B_e for the low-frequency limit discussed previously. This transverse magnetization decreases as $\Omega\tau$ approaches unity since the increasing misalignment of the M and H fields is accompanied by a decrease in the absolute magnitude of the transverse magnetization. This decrease results from the dominance of the denominator in (2.17) and (2.18) as $\Omega\tau$ increases.

2.4.3 Couette Flow Results

Imposing Couette flow conditions on the system of Fig. 2-1, the results of Fig. 2-4(a) through (c) and Fig. 2-5(a) through (c) show remarkably little difference from the prior case with no imposed flow although the top-plate of Fig. 2-1 now moves at 1 m/s compared to the previous case where it is fixed. However, as shown in Fig. 2-4(d), the top-plate velocity needs to be increased beyond 1 m/s before a perceptible change is observed in the value of ω_z. Referring to (2.42) and noting that the channel width d of Fig. 2-1 is 5 mm, it is noted that for Couette flow conditions to dominate the internal magnetic torque density of (2.25), it is required that U_c/d exceed $\langle T_{m,z} \rangle$. As shown in Fig. 2-5(g), this condition is not satisfied in the analysis above, even when $U_c = 10$ m/s. Values beyond this were not considered physiologically relevant as the maximum pulmonary flow velocity is approximately 1 m/s.

2.4.4 Poiseuille Flow Results

Imposing conditions of Poiseuille flow on the channel of Fig. 2-1 results in broadly similar results for both ω_z and M_{trans} as in the prior cases. Again, $\omega_z\tau$ shows linear

dependence on B_0, a quadratic dependence on B_e and little change with the value of ϕ. Similar dependence is also observed for the instantaneous transverse magnetization to both the previous cases. However, as clearly demonstrated by comparing Fig. 2-4(d) with Fig. 2-6(d), the Couette flow regime has a more significant impact on ω_z when the values of U_c and U_p are equal. Setting U_c =10 m/s for the Couette flow regime leads to a maximum value for $\omega_z\tau$ approaching 0.018 while setting U_p =10 m/s under Poiseuille flow conditions yields $\omega_z\tau = 0.013$. However since in neither case the flow-induced spin-velocity is significant enough to exceed the internal magnetic torque density, the values of M_{trans} shown in Figs. 2-5 and 2-7 are almost identical.

2.5 Conclusion

Current simulation results show that the ferrohydrodynamics of magnetite suspensions may be a source of frequency-controlled ferrofluid magnetization in the presence of a rotating magnetic field. This has important implications for MRI image contrast since the local magnetization can have an enormous impact on the MR image intensity (see chapter 25 of [35]). Foreseeable difficulties in the realization of this finding are (i) the large rotating field amplitudes required to show an appreciable transverse magnetization compared to the applied B_e excitation, (ii) the high fraction solid concentration, ϕ, required to see the effect and (iii) the disappearance of the effect once the rotating field is removed. However, in the event that these difficulties are overcome, based on the work of this thesis, it is to be expected that any change in the MRI phase measurement (the most convenient measure of changes in local field) will be less than 5%, compared to the phase measured in the absence of the rotating field. This estimate assumes a low-field MRI on the order of 0.2 T and a rotating field at 10% of B_0 with particle concentrations on the order of 1 to 5% solid magnetic volume.

An independent transverse excitation field is required in addition to the current B_1 field, used for RF excitation, in order to see appreciable transverse magnetization effects and the accompanying frequency dependence of the ferrofluid's transverse susceptibility. This second transverse field would require significant input power for fields on the order of 5% of B_0 as well as a controllable frequency of excitation. This means that demonstration of the effect is not feasible using the currently available B_1 and gradient fields in a low-field, open MRI system. Concentrations of contrast agent on the order of 3% solid volume are unlikely to be permitted *in vivo*. The recommended contrast agent dosage for Feridex corresponds to approximately 1.3×10^{-4}% solid volume after dilution in the subject's bloodstream (see Table B.1 of Appendix B). However, in the presence of suitable rotating field excitation, the effect may be shown *in vitro* or in MRI animal studies with the development of appropriate custom hardware. Finally, in order to maintain the effect on image contrast in MRI, the rotating field would need to remain on during the duration of the image readout. This is not true of the current B_1 field which is usually off during the image readout.

A recent development [110] in ultra-low field (ULF) MRI offers a new imaging method that uses SQUID sensors to measure the spatially encoded precession of prepolarized nuclear spin populations at a microtesla-range measurement field. ULF-MRI is attracting increasing interest since it enables simultaneous MRI and magnetoencephalography (MEG) imaging. The main B_0 for Zotev's work has a value of 46 μT and a B_1 field of 30 mT. Imaging results from [110] are shown in Figure 2-8.

The ultra-low field eliminates entirely any possibility of ferrofluid saturation and represents an enormous advantage over the previously considered low-field MRI (B_0 between 0.1 T and 0.35 T). However, the Larmor frequency at $B_0 = 46$ μT is 1940 Hz which now lies below the range where $\Omega\tau = 1$ for particles with τ on the order of

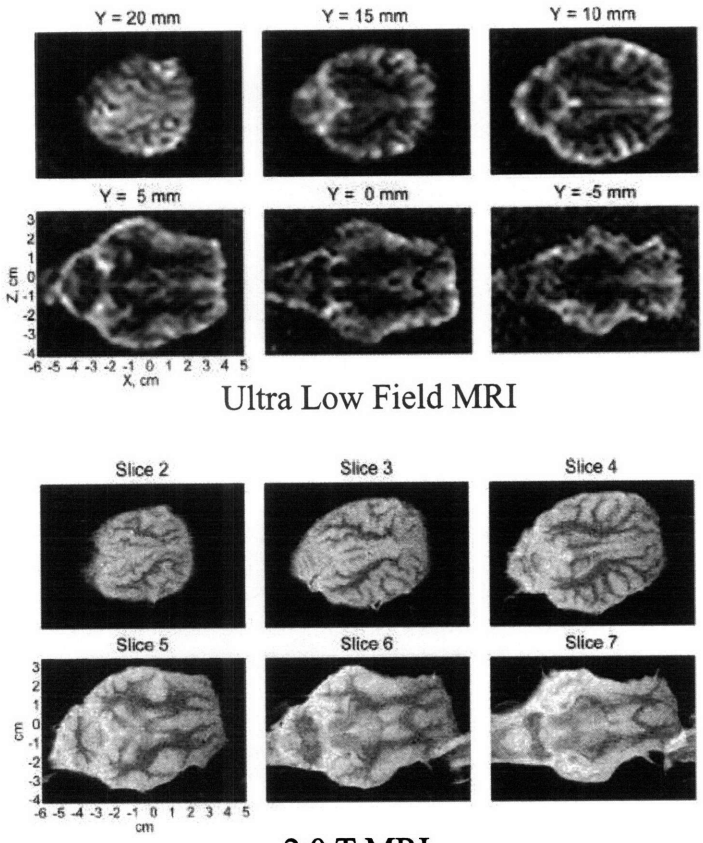

Figure 2-8: Imaging results from [110] for preserved sheep brain acquired (top) by 3D Fourier transform from the ULF-MRI and (bottom) from a 2T MRI with slice selection. Reproduced with the kind permission of Dr. Vadim Zotev, Los Alamos National Laboratory.

$1\mu s$. Larger particles would allow for longer values of τ but, ideally, the rotating field source should be of variable frequency to demonstrate image contrast as a function of frequency. This is not currently the case for Zotev's design. Notwithstanding this fact, the design may represent the most promising means of demonstrating MR image contrast due to the spin-velocity effects in ferrofluids due to a rotating magnetic field.

Chapter 3

Longitudinal Field Excitation

3.1 Introduction

The previous chapter explores the impact of ferrofluid spin-velocity effects in the presence of a rotating field excitation transverse to the main B_0 field. This chapter investigates the effect when the rotating field is no longer transverse to the main field but one component lies collinear with the B_0 field.

3.1.1 Governing Equations

As previously, the geometry shown in Fig. 2-1 is selected to allow the imposition of fields along all three axes. In this case, the main B_0 is y-directed while the rotating field excitation responsible for the presence of a ferrofluid spin-velocity is in the xy plane, such that one component is collinear with the main DC field. The situation is shown in Fig. 3-1.

The geometry is consistent with the analysis of the preceding chapter although, the DC field has been changed to point along the y axis. By convention, the main

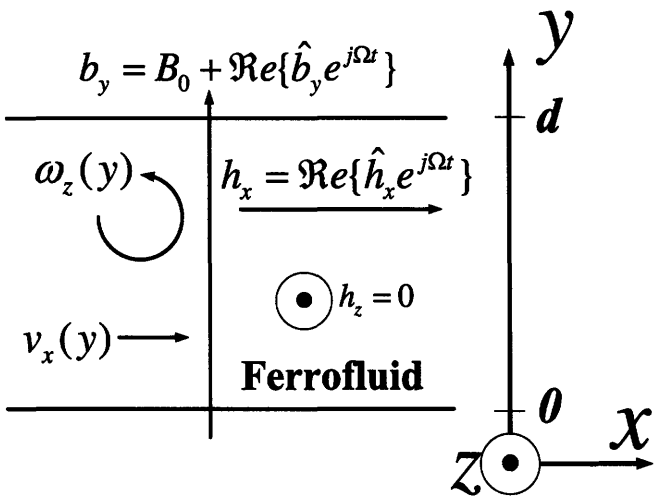

Figure 3-1: A planar ferrofluid layer between rigid walls is magnetically stressed by a uniform DC y-directed magnetic flux density B_0, a complex x-directed magnetic field of complex amplitude $\tilde{h}_x$ and a complex y-directed magnetic flux density of complex amplitude $\tilde{b}_y$. The complex x and y components vary sinusoidally at frequency Ω.

DC field in MRI is z-directed although in this chapter, it is written as y-directed for convenience. As previously, the flow velocity can only be x-directed and the spin-velocity may only be z-directed. Both quantities may vary spatially with y. The *transverse* plane in this case refers to the plane orthogonal to the main B_0 field, which is the $\{xz\}$ plane. There are no field components along $\boldsymbol{i}_z$ so only the field component along $\boldsymbol{i}_x$ constitutes a transverse field component.

$$\boldsymbol{v} = v_x(y)\boldsymbol{i}_x \tag{3.1}$$

$$\boldsymbol{\omega} = \omega_z(y)\boldsymbol{i}_z \tag{3.2}$$

Again, the governing equation for relaxation of the ferrofluid magnetization, **M**, is given by the expression of magnetic relaxation developed by Shliomis, in Eq. (2.2).

3.1.2 Magnetic Fields

Considering the geometric arrangement of Fig. 3-1, the imposed magnetic field intensities along $\boldsymbol{i}_x$ is spatially uniform and similarly for the imposed magnetic flux density along $\boldsymbol{i}_y$. Gauss's Law for the magnetic flux density and Ampère's Law for the magnetic field intensity require that this is the case. In light of this observation, one might write the total magnetic flux density $\mathbf{B}$ and the total magnetic field $\mathbf{H}$ as (3.3) and (3.4) respectively where $\tilde{h}_x$ and $\tilde{h}_y$ are now sinusoidally time-varying quantities and $\tilde{h}_z = 0$. As before, complex notation is used for convenience. The $\hat{}$ symbol denotes a complex amplitude, $\Re e$ signifies the real component of a complex quantity, Ω is the frequency of excitation in rad·s^{-1} and $\jmath = \sqrt{-1}$. The relationship between $\mathbf{B}$, $\mathbf{H}$ and $\mathbf{M}$ is given by the familiar expression of (3.6).

$$\mathbf{B} = \Re e\{(\hat{b}_x(y)\boldsymbol{i}_x + \hat{b}_y\boldsymbol{i}_y)\mathrm{e}^{\jmath\Omega t}\} + B_0\boldsymbol{i}_y \tag{3.3}$$

$$\mathbf{H} = \Re e\{(\hat{h}_x\boldsymbol{i}_x + \hat{h}_y(y)\boldsymbol{i}_y)\mathrm{e}^{\jmath\Omega t}\} + H_0(y)\boldsymbol{i}_y \tag{3.4}$$

$$\mathbf{M} = \Re e\{(\hat{m}_x(y)\boldsymbol{i}_x + \hat{m}_y(y)\boldsymbol{i}_y)\mathrm{e}^{\jmath\Omega t}\} + M_0(y)\boldsymbol{i}_y \tag{3.5}$$

$$\mathbf{B} = \mu_0(\mathbf{H} + \mathbf{M}) \tag{3.6}$$

The relationship between M_0 and H_0, the y-directed components of DC magnetization and magnetic field intensity respectively, has been established in (A.20). In seeking a solution for the instantaneous magnetization, the imposed fields $\hat{b}_y$ and $\hat{h}_x$ are assumed known. Substituting for $\mathbf{M}_{eq}$ from (A.17) through (A.20) and for $\mathbf{M}$

from (3.5) one might rewrite the x and y components resulting from the Shliomis Relaxation Equation using (3.6) as given by (3.7) and (3.8).

$$\hat{m}_x = \frac{(\jmath\Omega\tau + 1 + \frac{\partial M_0}{\partial H_0})\frac{M_0}{H_0}\hat{h}_x - (\omega_z\tau)\frac{\partial M_0}{\partial H_0}\frac{\hat{b}_y}{\mu_0}}{(\jmath\Omega\tau + 1)(\jmath\Omega\tau + 1 + \frac{\partial M_0}{\partial H_0}) + (\omega_z\tau)^2} \tag{3.7}$$

$$\hat{m}_y = \frac{(\omega_z\tau)\frac{M_0}{H_0}\hat{h}_x + (\jmath\Omega\tau + 1)\frac{\partial M_0}{\partial H_0}\frac{\hat{b}_y}{\mu_0}}{(\jmath\Omega\tau + 1)(\jmath\Omega\tau + 1 + \frac{\partial M_0}{\partial H_0}) + (\omega_z\tau)^2} \tag{3.8}$$

The only unknowns are the complex amplitudes of transverse magnetization $\hat{m}_x$ and $\hat{m}_y$ which are a function of the yet undetermined spin-velocity ω_z. Also, as given by Eq. (A.19), the y-directed small-signal magnetization, $\hat{m}_y$ shows strong dependence on the slope of the Langevin relation evaluated at the operating point established by B_0, *i.e.*, $\frac{\partial M_0}{\partial H_0}$.

As previously, the second term of (2.2) does not contribute any terms to the expressions of (3.7) and (3.8) since the flow velocity is along $\boldsymbol{i}_x$ and can only vary with y. The DC y-component of magnetization is given by the equilibrium value of M_0. However, it is the small-signal magnetization in the ferrofluid that gives rise to a torque which, in turn, is responsible for fluid motion causing a non-zero value for spin-velocity ω_z. This ω_z changes the magnetization. However, unlike the previous case when excitation was transverse to the main DC field, the transverse magnetization will no longer be ecliptically polarized in the transverse plain.

3.1.3 Fluid Mechanics

As for the previous analysis, the principles of conservation of linear and angular momentum are the equations of interest in defining a closed set of equations. These expressions, given in (2.19) and (2.22) are repeated here for convenience in Eqs. (3.9)

through (3.12).

$$-\nabla p' + \mu_0(\mathbf{M}\cdot\nabla)\mathbf{H} + 2\zeta\nabla\times\boldsymbol{\omega} + (\zeta+\eta)\nabla^2\boldsymbol{v} = 0 \tag{3.9}$$

$$p' = p + \rho g y \tag{3.10}$$

$$\boldsymbol{T}_m + 2\zeta(\nabla\times\boldsymbol{v} - 2\boldsymbol{\omega}) = 0 \tag{3.11}$$

$$\boldsymbol{T}_m = \mu_0(\mathbf{M}\times\mathbf{H}) \tag{3.12}$$

As before, these expressions represent simplifications of the more general expressions of He [45] and Elborai [44] although they are more than sufficient for the analysis which follows.

Beginning with the expression for the magnetic force density, $\mathbf{F}_m$, given by $\mu_0(\mathbf{M}\cdot\nabla)\mathbf{H}$ in Eq. (3.13), this can be rewritten as follows in Eq. (3.13) for the field expressions of Eqs. (3.3) through (3.5). Since the field variables only show a spatial dependence in the y direction, then the force density only has a y component for the geometry considered; $\mathbf{F}_m = F_{m,y}\boldsymbol{i}_y$.

$$F_{m,y} = \mu_0[\Re e\{\hat{m}_y e^{j\Omega t}\}\frac{\partial}{\partial y} + M_0\frac{\partial}{\partial y}][H_0 + \Re e\{\hat{h}_y\, e^{j\Omega t}\}] \tag{3.13}$$

Considering the x-directed H field to be spatially invariant and only considering the time-averaged, non-zero components of force density, one finds the reduced expression of Eq. (3.14).

$$\langle F_{m,y} \rangle = \mu_0 \langle \Re e\{\hat{m}_y \frac{\partial \hat{h}_y^*}{\partial y}\} + M_0 \frac{\partial H_0^*}{\partial y} \rangle \tag{3.14}$$

Since the y-directed $\mathbf{B}$ field is invariant in space, the derivative of the $\mathbf{H}$ field with respect y is equal and opposite to the derivative of the $\mathbf{M}$ field with respect to y. Note that M_0 is a real-valued expression so that it's complex conjugate is equal to M_0.

$$\langle F_{m,y} \rangle = \mu_0 \langle \Re e\{-\hat{m}_y \frac{\partial \hat{m}_y^*}{\partial y}\} - M_0 \frac{\partial M_0}{\partial y} \rangle \tag{3.15}$$

The expression is further simplified by application of the product rule for derivatives. As already noted in the case of a transverse rotating field, (3.17) only affects the pressure distribution and the flow profile can be solved independently.

$$\langle F_{m,y} \rangle = \mu_0 \langle \Re e\{-\frac{1}{2} \frac{\partial |\hat{m}_y|^2}{\partial y}\} - \frac{1}{2} \frac{\partial |M_0|^2}{\partial y} \rangle \tag{3.16}$$

$$\langle F_{m,y} \rangle = -\frac{\mu_0}{2} \frac{\partial |\hat{m}_y|^2}{\partial y} - \frac{\mu_0}{2} \frac{\partial |M_0|^2}{\partial y} \tag{3.17}$$

Considering Eq. (3.12), some considerable simplification is possible in the expression of the magnetic torque density, arising due to the omission of zero time-averaged terms and the geometry presented in Figure 3-1. Considering only the time averaged components, the expression of Eq. (3.12) can be rewritten as Eq. (3.18) where the expressions for $\mathbf{H}$ and $\mathbf{M}$ are given by Eq. (3.4) and Eq. (3.5) respectively. The only time-averaged, non-zero torque is z-directed, as expected.

$$\mathbf{T}_{m,z} = T_{m,z} \boldsymbol{i}_z = \mu_0 \Re e\{(\hat{m}_x \hat{h}_y^* - \hat{h}_x \hat{m}_y^*)\} \boldsymbol{i}_z \tag{3.18}$$

Time-averaging of a complex exponential requires the use of the complex conjugate, denoted by *. The expression of (3.18) contains no dependence on the DC H_0 field since there can be no non-zero, time-averaged component resulting from the cross-product of a DC and an AC quantity. The dependence on the term $\hat{h}_y$ is eliminated by reference to Eq. (3.6) leading to the final simplified expression given by Eq. (3.20).

$$\langle T_{m,z} \rangle = \frac{\mu_0}{2} \Re e\{(\hat{m}_x(\frac{\hat{b}_y}{\mu_0} - \hat{m}_y)^* - \hat{h}_x \hat{m}_y^*)\} \tag{3.19}$$

$$\langle T_{m,z} \rangle = \frac{1}{2} \Re e\{\hat{m}_x \hat{b}_y^* - \mu_0(\hat{m}_x + \hat{h}_x)\hat{m}_y^*\} \tag{3.20}$$

In light of the simplifications of (3.20) and (3.17), one might write the non-zero components for (3.9) and (3.11) as given by (3.21) through (3.23). Conservation of linear momentum yields components along both $\boldsymbol{i}_x$ and $\boldsymbol{i}_y$, given by (3.21) and (3.22) respectively. There is no component from the principle of conservation of linear momentum along $\boldsymbol{i}_z$. Also, there are no components along $\boldsymbol{i}_x$ or $\boldsymbol{i}_y$ from the principle of conservation of angular momentum and the z-component is given by (3.23).

$$-\frac{\partial p}{\partial x} + 2\zeta \frac{\partial \omega_z}{\partial y} + (\zeta + \eta)\frac{\partial^2 v_x}{\partial y^2} = 0 \tag{3.21}$$

$$\frac{\partial(p + \rho g y)}{\partial y} + \frac{\mu_0}{4}\frac{\partial |\hat{m}_y|^2}{\partial y} + \frac{\mu_0}{2}\frac{\partial |M_0|^2}{\partial y} = 0 \tag{3.22}$$

$$2\zeta \frac{\partial v_x}{\partial y} + 4\zeta \omega_z - \frac{1}{2}\Re e\{\hat{m}_x \hat{b}_y^* - \mu_0(\hat{m}_x + \hat{h}_x)\hat{m}_y^*\} = 0 \tag{3.23}$$

Similar to the previous chapter examining transverse rotating field excitation,

Eqs. (3.7), (3.8), (3.21) and (3.23) now constitute a closed system of equations with 4 unknown quantities: spin-velocity ω_z, flow velocity v_x and the two complex amplitudes of magnetization along $\boldsymbol{i}_x$ and $\boldsymbol{i}_y$ denoted $\hat{m}_x$ and $\hat{m}_y$ respectively. It is again noted that $\hat{b}_y$ and $\hat{h}_x$ are imposed fields and therefore known. While Eq. (3.22) is an additional equation of interest, it only changes the pressure distribution and not flow.

3.1.4 General Solutions

Field Driven Solution

Generalized analytical solutions are possible considering (3.7), (3.8), (3.21) and (3.23) when boundary conditions are defined. When both plates in Fig. 3-1 are fixed, the flow velocity is necessarily zero at the boundaries $y = 0$ and $y = d$. In the absence of any imposed flow or pressure differential in the channel, the first term of (3.21) is zero. As in the previous case of a transverse applied field, it it is not necessary to define boundary conditions on ω_z.

$$v_x(0) = v_x(d) = 0 \tag{3.24}$$

As outlined previously, additional boundary conditions for the field components follow the continuity law of electromagnetics such that normal components of $\mathbf{B}$ are continuous and tangential components of $\mathbf{H}$ are determined by the surface current, $\mathbf{K_s}$, at the boundaries $y = 0$ and $y = d$. Integrating (3.21) with respect to y and some rearranging leads to (3.25) where C_1 is a constant of integration.

$$\frac{\partial v_x}{\partial y} = -\frac{1}{\zeta + \eta}(C_1 + 2\zeta\omega_z) \tag{3.25}$$

Substituting this expression for the derivative of v_x in (2.26) and solving for ω_z

leads to (3.26).

$$\omega_z = \frac{\zeta + \eta}{8\eta\zeta}\Re e(\hat{m}_x\,\hat{b}_y^* - \mu_0(\hat{h}_x + \hat{m}_x)\,\hat{m}_y^*) + \frac{C_1}{2\eta} \tag{3.26}$$

After substituting the expressions for $\hat{m}_x$ and $\hat{m}_y$ from (3.7) and (3.8), the expression for ω_z from (3.26) shows no y dependence. The spin-velocity, ω_z, is necessarily a constant in space, thereby also setting the second term in (3.21) to zero. Solving the remaining non-zero term of (3.21) by integration with respect to y (since ζ and η are both assumed non-zero) and applying the boundary conditions of (3.24) shows that the flow velocity in the channel is zero. C_2 and C_3 are again constants of integration, which are zero to satisfy the zero velocity boundary conditions at $y = 0, d$.

$$\frac{\partial^2 v_x}{\partial y^2} = 0 \tag{3.27}$$

$$\frac{\partial v_x}{\partial y} = C_2 \tag{3.28}$$

$$v_x(y) = C_2 y + C_3 \tag{3.29}$$

$$v_x(0) = v_x(d) = 0 \Rightarrow C_2 = C_3 = 0 \Rightarrow v_x(y) = 0 \tag{3.30}$$

Applying this result to (3.25), one can solve $C_1 = -2\zeta\omega_z$ and substituting for C_1 in (3.25), the spin-velocity ω_z is given in terms of $\hat{m}_x$ and $\hat{m}_y$.

$$\omega_z = \frac{1}{8\zeta}\Re e(\hat{m}_x\,\hat{b}_y^* - \mu_0(\hat{m}_x + \hat{h}_x)\,\hat{m}_y^*) \tag{3.31}$$

While (3.31), (3.7) and (3.8) do not facilitate closed form solutions for ω_z, $\hat{m}_x$, and $\hat{m}_y$ the equations were solved using *Mathematica 5.2* (Wolfram Research, Champaign, Illinois) and numerical results are included in the following section.

Couette Flow Solution

The only difference between the case of an imposed Couette flow and the previous solution is the changed boundary condition at $y = d$ where $v_x(d) = U_c$ and U_c is the imposed linear velocity of the upper plate in $\mathrm{m{\cdot}s^{-1}}$. In addition to the imposed Couette flow, the applied rotating transverse field excitation remains present so that the spin-velocity is due to a combination of the magnetic driving field and fluid flow. There is no imposed pressure differential along $\boldsymbol{i}_x$ so the analysis is identical up until (3.25). However since the non-slip boundary condition at $y = d$ requires $v_x(d) = U_c$ this leads to a solution with $C_3 = 0$ and $C_2 = U_c/d$. Substituting into (3.25) one finds the revised form of (3.31) for imposed Couette flow conditions, given in (3.32).

$$\omega_z = \frac{1}{8\zeta}\Re e(\hat{m}_x\,\hat{b}_y^* - \mu_0(\hat{m}_x + \hat{h}_x)\,\hat{m}_y^*) - \frac{U_c}{2d} \tag{3.32}$$

Similarly to the no-flow solution, (3.32), (3.7) and (3.8) were solved using *Mathematica 5.2.* Explicit results are not included since, as will be outlined in the following discussion, these results will be coincident with the case of field-driven excitation in all practically achievable circumstances.

Poiseuille Flow Solution

Poiseuille flow is achieved in the channel by means of an x-directed pressure differential which, in the absence of a magnetic torque density in the fluid, results in a parabolic flow profile along $\boldsymbol{i}_y$. The imposed flow is, again, in addition to the rotating

field excitation in the $\{xy\}$ plane due to B_e. This complicates the previous solution and leads to the expression of (3.34) after twice integrating (3.21) with respect to y. Note that the first term of (3.21) is now non-zero, K_1 and K_2 are constants of integration while $\langle T_{m,z} \rangle$ is still given by (3.20).

$$-\frac{\partial p}{\partial x} y + \frac{1}{2}\langle T_{m,z} \rangle + \eta \frac{\partial v_x}{\partial y} + K_1 = 0 \tag{3.33}$$

$$-\frac{\partial p}{\partial x}\frac{y^2}{2} + \frac{1}{2}\int_0^y \langle T_{m,z} \rangle \, dy + \eta v_x + K_1 y + K_2 = 0 \tag{3.34}$$

Applying the non-slip boundary conditions on v_x at $y = 0$ and d allows for the solution of K_1 and K_2.

$$v_x(0) = 0 \Rightarrow K_2 = 0 \tag{3.35}$$

$$v_x(d) = 0 \Rightarrow K_1 = \frac{d}{2}\frac{\partial p}{\partial x} - \frac{1}{2d}\int_0^d \langle T_{m,z} \rangle \, dy \tag{3.36}$$

Substituting the results of (3.35) and (3.36) into (3.34) and rearranging, one arrives at (3.37).

$$\frac{\partial v_x}{\partial y} = \frac{1}{2\eta}\frac{\partial p}{\partial x}(2y - d) - \frac{1}{2\eta}\langle T_{m,z} \rangle + \frac{1}{2d\eta}\int_0^d \langle T_{m,z} \rangle \, dy \tag{3.37}$$

Substituting for the derivative of v_x given by (3.37) into (3.34) and substituting for K_1 and K_2 leads to an expression for ω_z which is independent of v_x and where $\langle T_{m,z} \rangle$ is given by (3.20).

$$\omega_z = -\frac{1}{4}\frac{\partial p}{\partial x}(2y - d) + \langle T_{m,z} \rangle \frac{\eta + \zeta}{4\zeta\eta} - \frac{1}{4d\eta}\int_0^d \langle T_{m,z} \rangle \, dy \tag{3.38}$$

Simplification of (3.38) is possible in the limit where the pressure differential dominates $\langle T_{m,z} \rangle$, the internal magnetic torque density after time-averaging. In such a scenario ω_z is a maximum or minimum at $y = \{0, d\}$, where the sign depends on the direction of the pressure differential and $\omega_z = 0$ at $y = d/2$. For x-directed flow, the differential is negative and ω_z is a positive maximum at $y = 0$ as given by (3.39).

$$\omega_z(0, d) = \pm \frac{d}{4\eta} \frac{\partial p}{\partial x} \tag{3.39}$$

Similarly for v_x which has a maximum value at $y = d/2$ given by (3.40).

$$v_x(d/2) = -\frac{d^2}{8\eta} \frac{\partial p}{\partial x} \tag{3.40}$$

As noted in the case of Couette flow and as will be outlined in the following discussion, explicit results for the case of Pouseille flow-driven magnetization are not included as it is shown that these will be coincident with the case of field-driven excitation in all practically achievable circumstances.

3.2 Results

3.2.1 Physical Parameters

The physical ferrofluid parameters are again selected for application of SPIO agents in low-field MRI scanners (0.1 T-0.3 T). The nominal values are identical to those investigated in the case of transverse rotating field excitation. The nominal parameters are repeated in Table 3.1 for convenience.

The main DC B_0 field is directed along $\boldsymbol{i}_y$. A rotating field of constant amplitude is generated in the longitudinal xy plane by setting $\hat{h}_x = H_e$ and $\hat{b}_y = jB_e$ where

Table 3.1: Table of Nominal Physical Parameters

Symbol	Value	Quantity
B_0	0.2	Main Flux Density in T
H_0	B_0/μ_0	Main Field Intensity in water in A·m^{-1}
B_e	5% of $B_0 = -j\hat{b}_y$	Rotating Flux Density Amplitude in T
H_e	$B_e/\mu_0 = \hat{h}_x$	Rotating Field Intensity in water in A·m^{-1}
μ_0	$4\pi \times 10^{-7}$	Permeability of free space in H·m^{-1}
R	4×10^{-9}	Mean particle radius in m
V_p	$4/3\,\pi R^3$	Magnetic particle volume in m^3
f	$1/(2\pi\tau)$	Frequency of transverse B_e field rotation in Hz
Ω	$2\pi f$	Frequency of electrical field rotation rad·s^{-1}
ϕ	0.03	Ferrofluid volume fraction of solids
α_0	$M_d V_p \mu_0 H_0/(kT)$	Equilibrium Langevin Parameter
M_0	$M_s L(\alpha_0)$	Equilibrium Ferrofluid Magnetization in A·m^{-1}
M_d	446×10^3	Single-domain magnetization (Fe_3O_4) in A·m^{-1}
M_s	ϕM_d	Saturation magnetization of ferrofluid in A·m^{-1}
τ	10^{-6}	Ferrofluid Time Constant in s
η	0.00202	Ferrofluid Kinematic Viscosity in Pa·s [44] [45]
ζ	$1.5\,\eta\,\phi$	Ferrofluid Vortex Viscosity in Pa·s [42]
T	295	Absolute temperature in K
k	1.381×10^{-23}	Boltzmann Constant in JK^{-1}
d	0.005	Channel width in m
U_c	1	Top plate velocity (Couette flow) in m·s^{-1}
U_p	1	Maximum flow velocity (Poiseuille flow) in m·s^{-1}

B_e and H_e are real-valued quantities. The resultant field rotates in a clockwise sense about the z axis. As before, the effect of varying the physical system parameters is examined for the normalized spin-velocity $\omega\tau$ and the magnitude of the instantaneous transverse magnetization $|M_{trans}(t)|$. It is noted that, unlike in Chapter 2 where the applied rotating field was in the transverse plane so that both components contributed

to $|M_{trans}(t)|$, for the case of a longitudinal rotating field, only the x component will contribute to the transverse magnetization (*i.e.*, the magnetization component perpendicular to the B_0 field). The y component represents a small deviation from the DC y-directed magnetization, denoted M_0 and is not expected to have any appreciable impact while $B_e \ll B_0$. Accordingly, $|M_{trans}(t)|$ is simply the instantaneous value of the x-directed magnetization with associated complex amplitude $\hat{m}_x$. As in the case of transverse field excitation, the transverse magnetization is normalized with respect to B_e by dividing by B_e/μ_0 for non-dimensionalized plotting.

$$M_{trans}(t) = \Re e\{(\hat{m}_x \boldsymbol{i}_x)\mathrm{e}^{\jmath\Omega t}\} \tag{3.41}$$

For simplicity, the instantaneous magnitude is evaluated at time $t = 0$ so that $|M_{trans}(0)|$ is given by (3.42).

$$|M_{trans}(0)| = \Re e\{\hat{m}_x\} \tag{3.42}$$

A further notable difference is apparent between the cases of transverse and longitudinal field excitation. While in the former case, the transverse magnetization is an elliptically polarized magnetization, in the latter case, the transverse magnetization will vary with time, since the orthogonal component responsible for the ferrofluid spin-velocity no longer lies in the transverse plane but parallel to the B_0 field along the $\boldsymbol{i}_y$ axis. To clarify this distinction, the instantaneous transverse magnetization is plotted over an entire cycle of the electrical frequency, Ω.

3.2.2 Field-Driven Results

The conditions of longitudinal field-driven excitation are simulated using the nominal values of Table 3.1 unless otherwise stated and the effect of changing B_0, B_e, and ϕ on both the normalized spin velocity $\omega_z\tau$ and the instantaneous transverse magnetization, normalized with respect to B_e, are investigated. The results are shown in Figs. 3-2 and 3-3 respectively. The plots are achieved using *Mathematica 5.2* with reference to (3.7), (3.8) and (3.31). In all cases, the x-axis is the normalized transverse rotating field frequency $\Omega\tau$.

The instantaneous transverse magnetization is plotted over an entire period of electrical frequency excitation, and is shown in Figure 3-4. In this plot, $B_0 = 0.2$ T, $B_e = 5\%$ of B_0 and $\phi = 3\%$. The excitation frequency varies as indicated.

3.3 Discussion

Many of the comments at the end of the preceding chapter are relevant to this discussion. These include the observation that for low-frequencies where $\Omega\tau \ll 1$, the effect of spin-velocity on the ferrofluid's transverse magnetization is negligible and $\omega_z\tau \ll 1$. Physically this low-frequency limit corresponds to a ferrofluid with a small-signal transverse susceptibility given by M_0/H_0 and the instantaneous transverse $\mathbf{M}$ and $\mathbf{H}$ vectors are collinear. This mimics the case of a transverse rotating field excitation.

As before, when $\Omega\tau$ approaches unity, the spin-velocity becomes increasingly significant since the ferrofluid time constant τ is no longer fast enough to allow the particles to reestablish transverse equilibrium before the excitation, now due to the rotating longitudinal field, changes direction. Instead, synchronism is maintained at

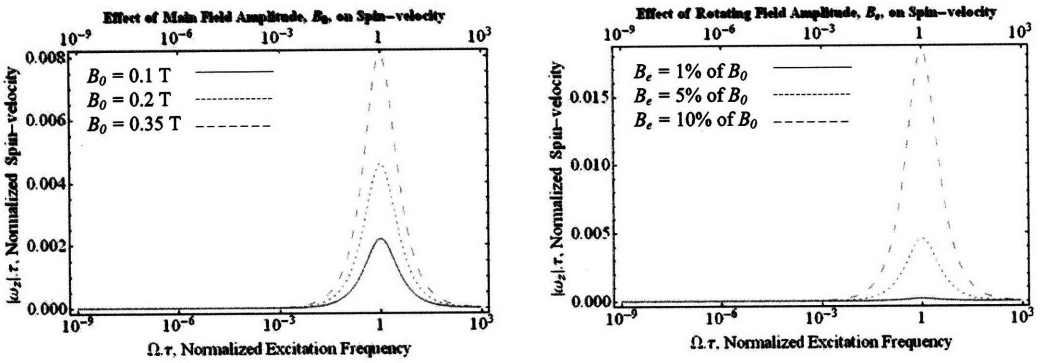

(a)

(b)

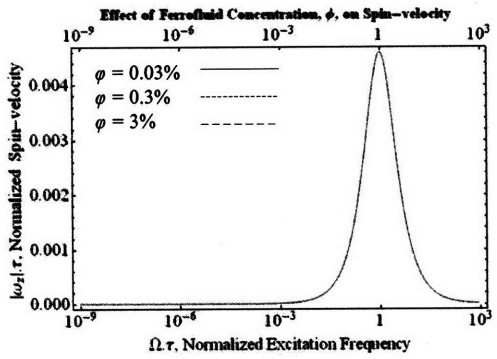

(c)

Figure 3-2: Frequency dependence of $\omega_z\tau$ on (a) B_0 (b) B_e and (c) ϕ is presented in the presence of longitudinal rotating field excitation and in the absence of any imposed fluid flow. Unless otherwise noted $B_0 = 0.2$ T, $B_e = 5\%$ of B_0 and $\phi = 3\%$.

a constant lag angle between the transverse components of **M** and **H** for a particular rotating field frequency Ω. Mathematically, this is shown by the on-axis magnetization (both $\hat{m}_x$ and $\hat{m}_y$) given by (3.7) and (3.8) becoming increasingly dependent on the orthogonal field component, $\hat{h}_x$ for the case of $\hat{m}_y$ and $\hat{b}_y$ for the case of $\hat{m}_x$. This cross-coupling results in an instantaneous transverse magnetization M_{trans} which lags the applied transverse rotating field, denoted H_{trans}.

As already noted, the high-frequency limit, where $\Omega\tau \gg 1$, is not acceptably modeled by Shliomis' Relaxation Equation and the plots are only included for com-

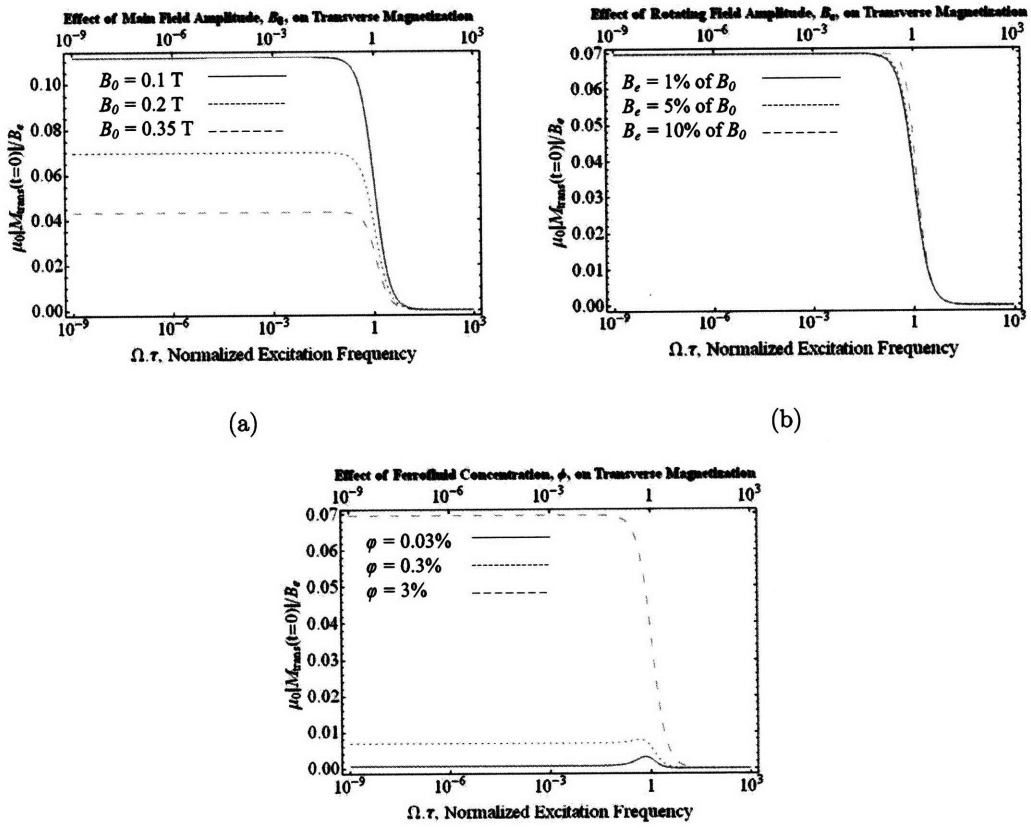

Figure 3-3: Frequency dependence of normalized, instantaneous, transverse magnetization, M_{trans} on (a) B_0 (b) B_e and (c) ϕ is presented in the presence of a longitudinal rotating field excitation and in the absence of any imposed fluid flow. Again, unless otherwise noted $B_0 = 0.2$ T, $B_e = 5\%$ of B_0 and $\phi = 3\%$.

pleteness. The y-directed DC magnetization, M_0, is not frequency dependent as before and is given by (A.20) throughout.

3.3.1 Field-Driven Results

In the absence of externally imposed flow, the ferrofluid spin-velocity is spatially constant in the channel of Fig. 2-1. As noted, the maximum spin-velocity occurs when $\Omega\tau = 1$ and increases linearly with the main y-directed B_0 field, as shown in

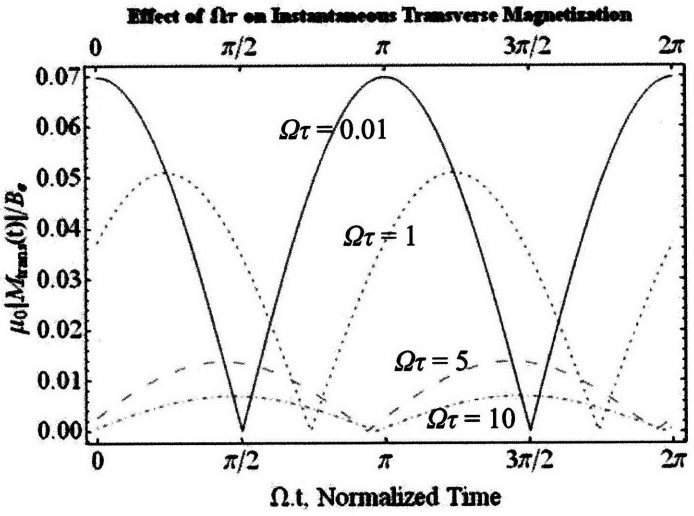

Figure 3-4: Time variation of the normalized, instantaneous, transverse magnetization, M_{trans} is presented in the presence of a longitudinal rotating field excitation and in the absence of any imposed fluid flow. Four different excitation frequencies are examined: (i) $\Omega\tau = 0.01$, (ii) $\Omega\tau = 1$, (iii) $\Omega\tau = 5$ and (iv) $\Omega\tau = 10$. The other parameters are $B_0 = 0.2$ T, $B_e = 5\%$ of B_0 and $\phi = 3\%$.

Figure 3-2(a). However, the maximum value of the normalized spin velocity is reduced almost by a factor of 2 compared to the case of transverse rotating field excitation. This is because of the difference between the small-signal transverse and longitudinal susceptibilities for a representative 4 nm radius magnetic particle. This low-frequency, small-signal susceptibility in the transverse plane is given by M_0/H_0 whereas the low-frequency, small-signal susceptibility in the longitudinal plane is given by $\frac{\partial M_0}{\partial H_0}$. The relationships are plotted in Figure A-1 of Appendix A for the values of Table 3.1 as the main B_0 field varies.

At a main field strength of 0.2 T, the difference between M_0/H_0 and $\frac{\partial M_0}{\partial H_0}$ is a factor of 2 although this also depends on the particle radius. For this reason, the associated spin-velocity is halved when the rotating field is swapped from the transverse to longitudinal plane. This is seen by comparing Figures 2-2 and 3-2. The relative dependencies on B_0, the rotating field amplitude B_e and the ferrofluid solid volume

percentage ϕ correspond to the case where B_e is transverse to the B_0 field.

The instantaneous magnetization shows similar dependence of ω_z on B_0 and B_e to the former case of transverse excitation, as seen from Figs. 3-3(a) and (b). However, the value of the maximum transverse magnetization is significantly reduced when the rotating field excitation is moved to the longitudinal plane, for the reason already outlined. This is not evident from comparison of Figures 2-3 and 3-3 because while the transverse field excitation results in a constant-amplitude transverse magnetization, the longitudinal rotating field excitation does not. Rather, it peaks once every cycle at a maximum value that is equal to the constant value in the transverse excitation case. Such a maximum occurs at time $t = 0$ and for this reason, the transverse magnetization does not appear significantly altered with the reorientation of the rotating field. The new, time-dependence of the transverse magnetization is well described in Figure 3-4. Also clearly visible in Figure 3-4 is the temporal phase shift associated with the transverse magnetization as the value of Ω is increased. At low-frequency, where $\Omega\tau \ll 1$ the transverse M and H fields are in phase but this is increasingly not the case as $\Omega\tau$ increases towards unity.

3.3.2 Flow Driven Excitation and Longitudinal Fields

Imposing Couette or Poiseuille flow conditions on the system of Figure 3-1 results in an additional source for the spin-velocity in the ferrofluid, as given by Eq. (3.32) for Couette flow and Eq. (3.38) for Poiseuille flow. However, as noted for the case of transverse rotating field excitation, it is very difficult to envisage a physically realizable scenario in which the flow-induced contribution to spin-velocity may be comparable or equal to the contribution from the magnetic torque density. While the magnetic torque density is somewhat reduced by the reorientation of the rotating field

to the longitudinal plane, it cannot be expected that this will result in any appreciable change to the conclusion of the previous analysis for the transverse excitation. Accordingly, the application of either Couette or Poiseuille flow is not pursued further in this treatment.

3.4 Conclusion

In comparing the resulting spin-velocity and transverse magnetization in the two orientations of applied rotating field excitation, a number of points are worth noting.

- The ferrofluid spin-velocity is approximately halved by the reorientation of the applied rotating field from the transverse to longitudinal planes. This difference corresponds to the difference between the values of M_0/H_0 and $\frac{\partial M_0}{\partial H_0}$ evaluated at the operating point defined by the B_0 field.

- The transverse magnetization is a constant-amplitude rotating field in the case of a transverse rotating field excitation. However, in the case of longitudinal rotating field excitation, the transverse magnetization is no longer constant in amplitude but varies with time at the same frequency as the applied electrical frequency, Ω, since the x-directed component no longer lies in the longitudinal rather than in the transverse plain.

- In order to see a more appreciable change in the transverse magnetization, it appears that the transverse rotating field is a more attractive alternative. This is because the value of the transverse magnetization in this case represents a larger, and hence easier to detect, quantity relative to the amplitude of the rotating field which causes it. However, in either case, the application of the

ferrofluid spin-velocity as a source of image contrast in MRI would require the use of custom hardware. Further experimental investigation was judged beyond the scope of this work.

- The impact on MR image intensity in the presence of ferrofluid is expected to be difficult to detect due to a rotating field with one component aligned with B_0. This is because the change in magnetization is even smaller than the case where the field rotates in a plane perpendicular to B_0 since now one component of the rotating field represents a deviation from the already partly-saturated DC magnetization. The same comments regarding ULF-MRI apply to this approach but the approach of Chapter 2 is recommended for any further experimental work.

Chapter 4

Spin Velocity and Mechanical Rotation

4.1 Introduction

In addition to spin-velocity due to electrically rotating magnetic field excitation, the phenomenon is also observed due to mechanical rotation of a ferrofluid sample [107–109]. In particular, the arrangement of concentric cylinders has been investigated since this readily facilitates Taylor-Couette flow where the inner cylinder is driven by a mechanical rotation about its central axis and the outer cylinder is maintained at rest. Under these conditions, the magnetization of the ferrofluid in the inner cylinder is a function of the rotating frequency, the ferrofluid time constant and the mechanical rotation frequency, as determined by Shliomis' Relaxation Equation, repeated in Eq. (4.1)

$$\frac{\partial \mathbf{M}}{\partial t} + \boldsymbol{v} \cdot \nabla \mathbf{M} - \boldsymbol{\omega} \times \mathbf{M} + (\mathbf{M} - \mathbf{M}_{eq})/\tau = 0 \tag{4.1}$$

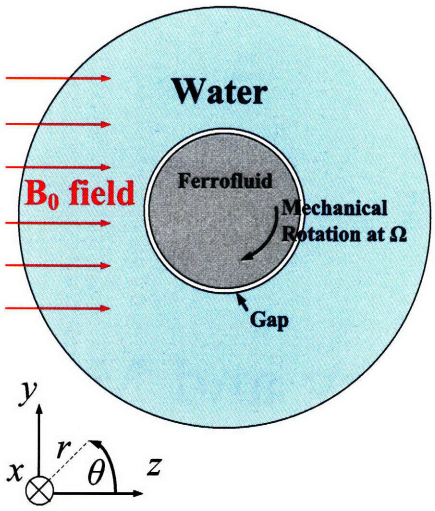

Figure 4-1: The arrangement to facilitate Taylor Couette flow in the inner cylinder requires that the inner cylinder be rotated at an angular frequency of Ω rad/s. For the numerical results which follow, the gap approaches 0 and the ferrofluid container radius is 1.2 cm.

4.2 Governing Equations

To investigate the feasibility of spin-velocity generation in the MRI environment by means of mechanical rotation, the arrangement of Figure 4-1 was simulated in *Comsol Multiphysics*. The main DC B_0 field is z-directed and transverse to the cylinder's axis of rotation, which is along $\boldsymbol{i}_x$. Many of the simplifications applied in the earlier analysis of a simple channel geometry no longer apply and only a numerical solution is possible. This is due to a non-zero spatial-derivative given by the second term in Shliomis' Relaxation Equation. The value of Ω which previously represented the electrical frequency of excitation is now representative of the mechanical rotation frequency of the inner cylinder.

In Chapters 2 and 3, the $\boldsymbol{v} \cdot \nabla \mathbf{M}$ term was eliminated by means of the channel

geometry previously employed to investigate the effect of electrical rotating fields. However, in the presence of mechanical rotation with the arrangement of Figure 4-1, this is no longer the case. A further complication is that it is no longer possible to write an analytical expression for the ferrofluid susceptibility in the presence of Taylor-Couette flow due to this spatial derivative. To avoid this problem, and without undue loss of generality, the analysis which follows assumes a saturated ferrofluid such that the equilibrium magnetization is z-directed and given by M_s, the saturation magnetization of the suspension in $\mathrm{A{\cdot}m^{-1}}$. As has been previously shown in Figure 1-4, saturation is virtually assured in almost all common clinical MRI environments (1.5 T and 3 T) and is only avoided in the case of low-field open MRI (0.1 T to 0.35 T). Furthermore, the assumption of magnetic saturation does not jeopardize any resulting conclusions of the analysis which follow since the absence of saturation simply adds a non-zero x-directed ferrofluid magnetization component in equilibrium. Saturation also results in torque and force densities that are dominated by the field in the ferrofluid rather than the flow. This means that the second term of Eq. (4.1) has only limited impact on the ferrofluid spin-velocity.

In the presence of Taylor-Couette flow, the dominant flow direction will be parallel to the cylinder wall in the same sense as the mechanical rotation. In cylindrical coordinates, this corresponds to the negative θ direction[1], and the azimuthal flow velocity, v_θ is as indicated in Figure 4-1. Accordingly, it can be expected that the spatial variations in the flow will be along the radial r axis and the induced spin-velocity will be x-directed; $\boldsymbol{\omega} = \omega_x \boldsymbol{i}_x$.

In light of these simplifications, Eq. (4.1) may be rewritten in cylindrical coor-

[1]By convention, this direction is denoted ϕ in cylindrical coordinates. However, to avoid confusion with the ferrofluid solid volume concentration, ϕ, it is denoted θ here. Also, in the orientation of Figure 4-1, the x axis is left-handed with respect to the cylindrical unit vectors, $\boldsymbol{i}_\theta$ and $\boldsymbol{i}_r$.

dinates, where Eq. (4.2) realates the radial components while Eq. (4.3) gives the azimuthal directed components. The analysis assumes sinusoidal steady state.

$$\frac{\partial M_r}{\partial t} + \frac{v_\theta}{r}\frac{\partial M_r}{\partial \theta} + \Omega_x M_\theta + \frac{1}{\tau}(M_r - M_s \cos\theta) = 0 \tag{4.2}$$

$$\frac{\partial M_\theta}{\partial t} + \frac{v_\theta}{r}\frac{\partial M_\theta}{\partial \theta} - \Omega_x M_r + \frac{1}{\tau}(M_\theta + M_s \sin\theta) = 0 \tag{4.3}$$

In conjunction with Shliomis' Relaxation Equation, the principles of conservation of linear and angular momentum are the governing mechanical equations. These are identical to those given in Eqs. (2.19) and (2.21) although considerable simplification results from the replacement of $\boldsymbol{\omega}$ with Ω in the absence of any magnetic torque, thus eliminating an unknown quantity in the case of mechanically-driven flow. The construction of the differential equations for a cylindrical geometry follow the form employed by He [45]. Following He's approach, only time-averaged quantities are considered, thus considerably reducing the numerical burden on the *Comsol Multiphysics* software.

Another advantage of considering a saturated ferrofluid is that the magnetic field inside the ferrofluid can be written directly, where the demagnetizing field, denoted M_D, in an infinitely long cylinder is given by half the magnetization in the direction opposing the applied field outside the ferrofluid. Since the region outside the ferrofluid is water, and the magnetization vector in this region is zero, the **H** field inside the ferrofluid is given by Eq. (4.6) in cylindrical coordinates. For Figure 4-1, $r < R_1$ corresponds to the region inside the gap while $r > R_1$ is that region outside the gap.

$$\mathbf{H}(r < R_1) = H_0 \boldsymbol{i}_x - M_D \boldsymbol{i}_x \tag{4.4}$$

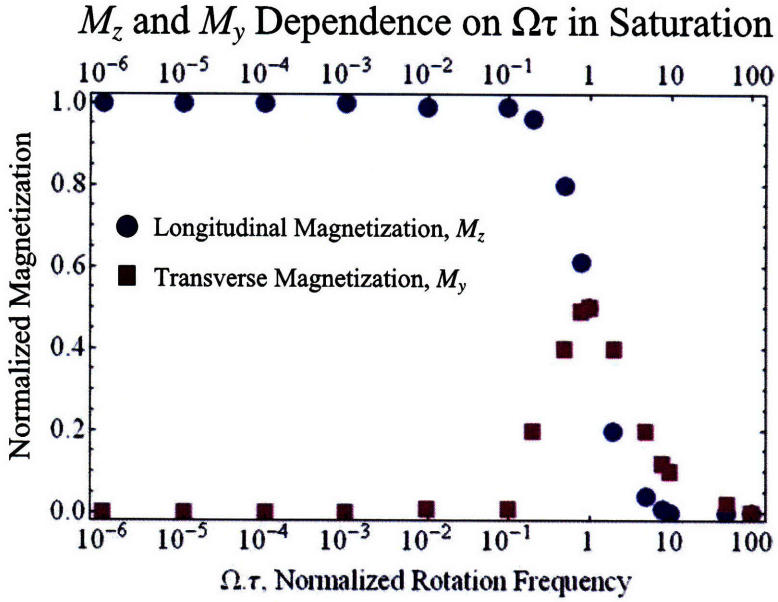

Figure 4-2: The time-averaged magnetization is plotted as $\Omega\tau$ is increased for the transverse and longitudinal magnetization components.

$$\mathbf{H}(r < R_1) = H_0 \boldsymbol{i}_x - \frac{1}{2} M_s \boldsymbol{i}_x \tag{4.5}$$

$$\mathbf{H}(r < R_1) = (H_0 \cos\theta - \frac{\mathrm{M_s}}{2}\cos\theta)\boldsymbol{i}_\mathrm{r} + (-\mathrm{H_0}\cos\theta - \frac{\mathrm{M_s}}{2}\sin\theta)\boldsymbol{i}_\theta \tag{4.6}$$

The results of Figure 4-2 only show time-averaged magnetization components. When $\Omega\tau \ll 1$, the time constant of the ferrofluid is sufficiently responsive to allow the ferrofluid magnetization to never become misaligned with the applied B_0 field acting along $\boldsymbol{i}_x$. The x-component of magnetization is given by the saturation magnetization and there exists no appreciable magnetization component transverse to the B_0 field. As $\Omega\tau$ approaches unity, the nanoparticles are no longer able to realign themselves instantaneously with the B_0 field so a small transverse magnetization component emerges. This component, M_y increases with $\Omega\tau$ until $\Omega\tau \approx 1$. At this point, the system enters a new domain of operation where the ferrofluid is no longer responsive

to the B_0 field and the magnetization instead follows the applied mechanical rotation. The nanoparticles will rotate in unison with the applied rotation Ω and no realignment is possible with the B_0 field. In these circumstances, the magnetization will be a rotating vector at the same frequency as the applied mechanical rotation, Ω and there is zero time-averaged component of magnetization as $\Omega\tau$ is increased beyond unity. It should be noted that it is extremely difficult to envisage a physical experiment where this scenario is achievable since mechanical rotation on the order of 10^6 rpm would be required for $\tau = 1\mu$s. Nonetheless, the numerical simulation is instructive to validate the outlined intuitive understanding. The *Comsol* results show the time-averaged transverse and longitudinal magnetization components in Figure 4-2.

For the MRI environment, it is clearly shown that the ferrofluid magnetization only shows dependence on the applied mechanical rotational frequency when $\Omega\tau \approx 1$. Although some variation is seen from $\Omega\tau \approx 0.1$, even this would necessitate an applied rotation of 10^5 rpm for a particle with $\tau \approx 10\ \mu s$. Such an experimental scenario seems unlikely and therefore the concept of mechanical rotation as a means for demonstration in the MRI environment is not pursued further in this thesis.

Chapter 5

Experimental Imaging Results in 1.5 T and 3 T MRI

5.1 Introduction

In conjunction with the effect of rotational or spin velocity effects on ferrofluids in the MRI environment, the passive characterization and the linear dynamics of superparamagnetic nanoparticles have also been examined. This chapter is divided in two sections; the first examines the passive characterization of the magnetization of commercial MRI contrast agents at 3T. This includes a method to determine the magnetization of the agents at this field strength using B_0 phase maps in MRI. The second section follows from the discussion in chapter 2 of Rosensweig's text [42] where the stability criteria for magnetic nanoparticles are outlined. Two categories of stability are considered in this work. They are (i) the stability of the nanoparticles in a magnetic field gradient and (ii) the stability against chaining in a high-field.

5.2 Magnetization Characterization at 3 T

The goal of this portion of the work was to demonstrate the ability of MRI to accurately measure the magnetization associated with two commercial MRI contrast agents. These agents were Feridex (AMAG Pharmaceuticals, Cambridge, MA), a superparamagnetic iron oxide suspension used primarily for liver imaging [59,62] and Magnevist (Bayer HealthCare AG, Leverkausen, Germany) [61], a paramagnetic, Gd-based compound used mainly as a gastrointestinal contrast agent to visualize the bowel in MRI.

5.2.1 Phase and B_0 Maps for Commercial Contrast Agents

To examine magnetic saturation effects in a commercial SPIO contrast agent, we took a sample of Feridex MRI contrast agent and using a vibrating sample magnetometer, measured the magnetic moment per unit volume. The result is shown in Figure 5-1(a) where the units of magnetic moment are given as Am^2/kg of Fe. Feridex is the only commercial SPIO contrast agent for use in clinical MRI which is FDA approved. Feridex is a superparamagnetic agent which saturates at high field. The saturation magnetization of the agent was estimated to be in the region of 84 Am^2/kg Fe. One of the drawbacks of VSM and SQUID magnetometery is that the maximum field strength is usually limited. For the Feridex VSM measurements shown in Figure 5-1(a), there was no data beyond 1.2 T. Magnevist is a paramagnetic agent which exhibits a linear magnetic susceptibility up to DC fields of 50 T [25]. The mass susceptibility, χ_m, was estimated by a linear curve fit to be 2.06×10^{-6} m^3/kg Gd from the VSM measurements shown in Figure 5-1(b). Again, there was no available data beyond 1.2 T.

In order to estimate the magnetization in MRI, B_0 maps were obtained in a 3 T

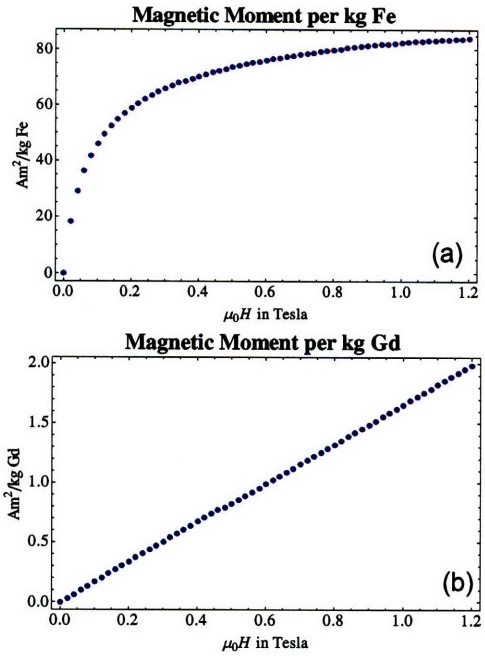

Figure 5-1: Measured magnetization using a VSM for (a) Feridex and (b) Magnevist MRI contrast agents. The units of magnetic moment are (a) Am^2/kg Fe for Feridex and (b) Am^2/kg Gd for Magnevist.

Siemens Trio MRI. The agent was placed in a long, narrow NMR tube: 10 cm in length and 3.43 mm inside diameter. The walls of the tube were 0.41 mm thick. The tube was fixed to lie horizontally in a water tank for imaging and positioned so that the B_0 field lay transverse to the tube's principle axis. The tube's center slice was imaged at 3 T with an imaging resolution of 256×256 pixels, a 180mm FOV, a slice thickness of 7 mm and a repetition time, TR = 100 ms. Using 10 averages, the total scan time was 4.25 minutes. The phase maps and B_0 maps are shown in Figures 5-2 and 5-3 for the Feridex contrast agent, where TE = 2.83 ms for the phase map and ΔTE = 0.9 ms for the B_0 map. The B_0 map was corrected for edge effects and shimming by taking a second B_0 map in the absence of the tube and identical

imaging parameters including the same shimming fields. The second B_0 map was then subtracted from that due to the tube. The original result before correction is shown in Figure 5-2 for the Feridex agent. The corrected B_0 map is shown in Figure 5-3. An identical procedure was employed to obtain a similar result for the Magnevist agent.

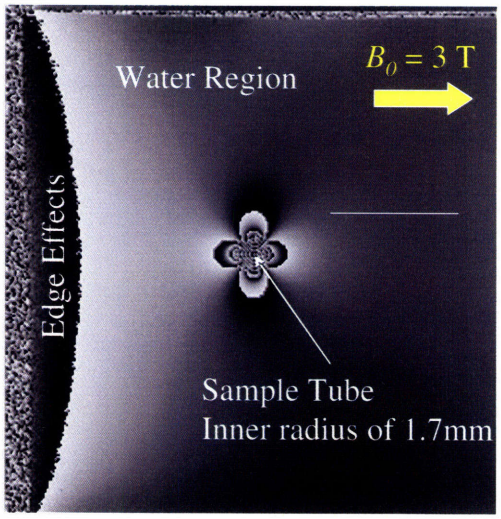

Figure 5-2: The phase map is shown for the center slice of a tube of Feridex agent surrounded by water. The phase map only shows the net field component along the z-axis, *i.e.*, B_z. The B_0 field is left to right and has a value of 3 T.

Next, the theoretical solution for the dipole field surrounding the tube was simulated with the same geometric values using a 3D model in Comsol Multiphysics and the results compared over the same frequency range as in Figure 5-3. The Comsol result used a saturation magnetization of 74 Am^2/kg Fe, the result which most accurately replicated the results from the MRI measurements. The resulting simulated dipole distribution is shown in Figure 5-4(a). It should be noted that this represents the change in the z component of the B_0 field rather than the magnitude of the magnetic field. Therefore, the distribution is quadrapolar rather than dipolar as given by Equation 5.3 for an infinite cylinder in an x-directed field following the example

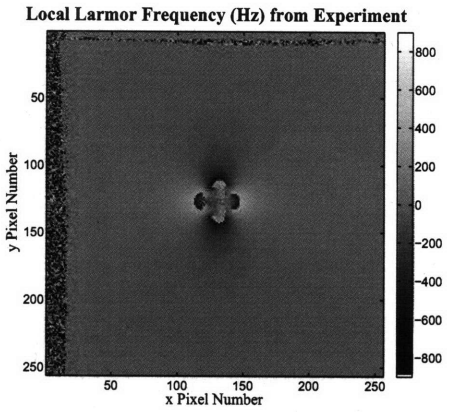

Figure 5-3: The B_0 map is shown for the center slice of a tube of Feridex agent surrounded by water. Edge and shim effects were eliminated by means of a subtraction of the B_0 maps measured in the absence of any tube.

of problem 5.32(c) in Zahn's text [43]. For the numerical results, the vial radius, a, is 3.43 mm, corresponding to the inner diameter of the vials and r represents the axial radius measured from the vial's center. The main field is denoted $H_0\,\boldsymbol{i}_x$, the saturation magnetization (assumed x-directed for consistency with Zahn's solution) has a value of M_s and $\phi = \arctan(y/x)$.

$$\boldsymbol{H}(r > a) = (H_0 + \frac{M_s a^2}{2r^2})\cos\phi\boldsymbol{i}_r - (H_0 - \frac{M_s a^2}{2r^2})\sin\phi\boldsymbol{i}_\phi \tag{5.1}$$

$$\boldsymbol{H}(r > a) = (H_0 + \frac{M_s a^2}{2r^2})\cos 2\phi\boldsymbol{i}_x + \frac{M_s a^2}{2r^2}\sin 2\phi\boldsymbol{i}_y \tag{5.2}$$

$$\Delta H_x(r > a) = \frac{M_s a^2}{2r^2}\cos 2\phi \tag{5.3}$$

The experimental result of Figure 5-4(b) is the field map from Figure 5-3 after windowing (140×140 pixels) and adding a colormap in Matlab (Mathworks Corp., Natick MA). Clearly some phase wrapping occurs in the region around the tube as

the field varies too rapidly to be captured accurately by the field map. This means that the field immediately surrounding the tube itself is severely distorted from the actual value. However, the dipole fields are closely matched in areas which do not suffer from phase wrapping.

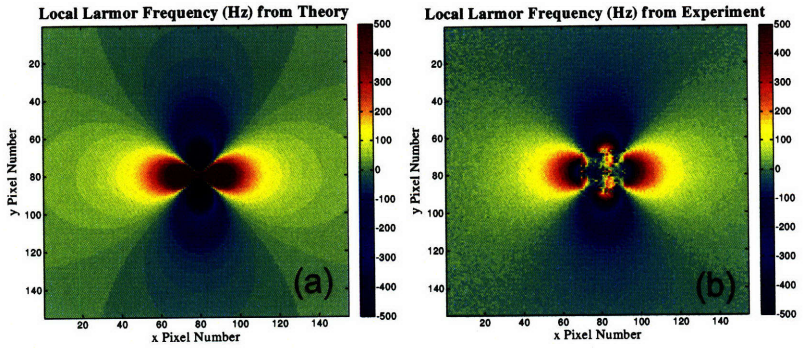

Figure 5-4: Comparing (a) theoretical results from Comsol Multiphysics and (b) B_0 maps from the scanner at 3 T for Feridex contrast agent.

The results of Figure 5-4 were compared for the line of maximum field variation along the x axis. The results are shown in Figure 5-5 where the black solid line indicates the measured result for the change in local Larmor frequency using MRI, the red line represents a least-squares fit of the MRI result assuming M_s =74 Am^2/kg Fe and the blue line represents the result based on the VSM measurement of M_s =84 Am^2/kg Fe. We can compare these results with the only available similar analysis, as detailed in [60]. Here, the magnetization of Feridex-like ferumoxides was estimated at 0.6 T and 5 T. The resulting mean value of the magnetization was measured to be 69.8 Am^2/kg Fe at 0.6 T and 93.6 Am^2/kg Fe at 5 T.

Using an identical procedure to that outlined to obtain the results of Figure 5-4, the B_0 and phase maps were obtained for the Gd-based contrast agent, Magnevist. The theoretical results from Comsol (using a value for the susceptibility as estimated

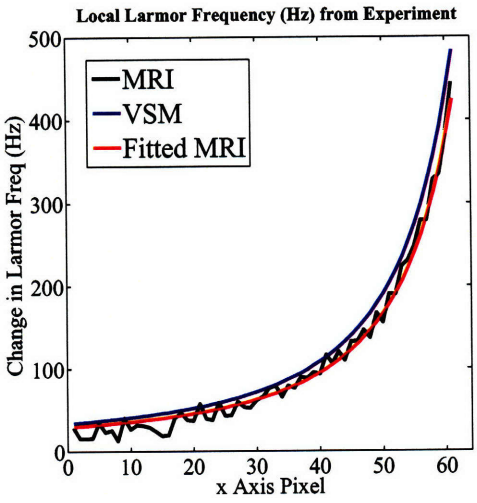

Figure 5-5: Comparing experimental results from the MRI (black), extrapolated results from the VSM at 1.2 T (blue) and theoretical results from Comsol Multiphysics (red) based on a least-squares fit of the MRI data for the change in local Larmor frequency due to the SPIO agent, Feridex.

from the VSM results) and B_0 map at 3 T are shown in Figure 5-6. The results in Figure 5-6 are compared along the line of maximum field variation along the x axis, as was the case for the Feridex results. The results are shown in Figure 5-7 where the black solid line indicates the measured result for the change in local Larmor frequency using MRI, the red line represents a least-squares fit of the MRI result assuming $\chi_m = 1.8 \times 10^{-6}$ m^3/kg Gd and the blue line represents the result from the VSM measurement of 2.06×10^{-6} m^3/kg Gd. It should be noted that the mass susceptibility, χ_m in m^3/kg, is related to the absolute susceptibility, χ (unitless), by the concentration of the magnetic material in the fluid in kg Gd/m^3. For Magnevist contrast agent, the supplied concentration [61] is 78 kg Gd/m^3 although this is diluted for clinical administration as indicated in Appendix B. Jung et al. [60] listed a mass susceptibility for Magnevist of 2.72×10^{-2} cgs/mol or 2.13×10^{-6} m^3/kg Gd which is comparable to our results.

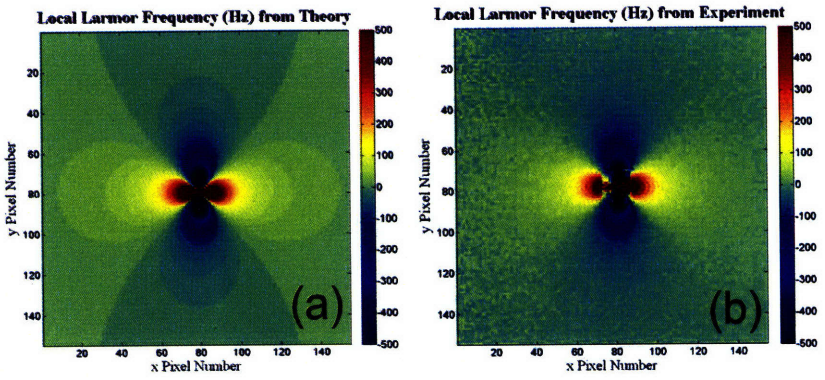

Figure 5-6: Comparing (a) theoretical results from Comsol Multiphysics and (b) B_0 maps from the scanner at 3 T for Magnevist contrast agent.

For the VSM measurements, it is worth noting that the susceptibility of deionized water was measured using the VSM to be -12×10^{-6}. The recorded and accepted result is -9×10^{-6} [93] indicating that there may be a small DC bias on the VSM measurements tending to skew the results as indicated above. This is one plausible source for the small error between the VSM measurements shown and the results from the MRI at 3 T. Another source of error is possible misalignment between the theoretical and experimental phase maps, resulting in the theoretical least-squares fit not correlating to the exact same point along the x axis in the experimental results.

Conclusions

Table 5.1: Comparison of Feridex Results for M_s

VSM Measurement	Fitted MRI Result	Published Result [60]
84 Am^2/kg Fe	74 Am^2/kg Fe	93.6 Am^2/kg Fe

The results for the saturation magnetization of Feridex contrast agent is compared in Table 5.1 using three different results. These are the VSM measurements which yielded a result of 84 Am^2 kg Fe at 1.2 T, the fitted MRI measurement which yielded

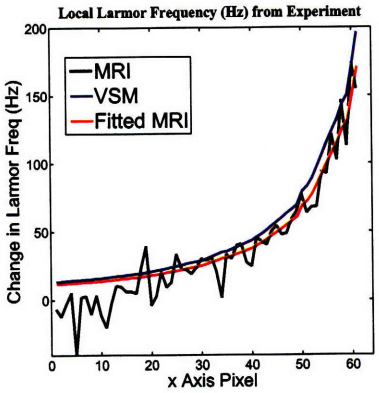

Figure 5-7: Comparing experimental results from the MRI (black), extraopolated results from the VSM at 1.2 T (blue) and theoretical results from Comsol Multiphysics (red) based on a least-squares fit of the MRI data for the change in local Larmor frequency due to the Gd-based contrast agent, Magnevist.

a value of 74 Am^2 kg Fe at 3 T and the published result of Jung et al. who cite a result of 93.6 Am^2 kg Fe at 5 T. One would expect that the results should increase with increasing field. However, this is not the case indicating some discrepancy in the results. As already noted, it was found that there was a slight DC bias on the VSM which was thought to skew results. However, this is not sufficient to account for the discrepancy. Therefore, it is most likely that some additional error is introduced in the MRI. This might include an inaccurate fit of the experimental data (for example, if datapoints closer the the vial tend to suffer more from uncompensated edge effects, this is not reflected in the least-squares fit) and a misalignment between the Comsol result and the MRI measurement (meaning that pixels were not exactly matched in space and therefore introducing an error in the predicted value for the saturation magnetization). However, it is also possible that there was some error associated with the result of Jung [60]. The results are, at least, broadly similar, as is seen in Figure 5-5 and the goal of the experiment, to show that MRI can be used to accurately measure contrast agent magnetization, has been verified.

The results for the mass susceptibility of Magnevist contrast agent is compared in Table 5.2 using the same three methods and again, good agreement is found. The comments of the previous paragraph are again applicable. Furthermore, the slight variation in the results of Table 5.2 is difficult to see in the imaging results of Figure 5-7.

Table 5.2: Comparison of Magnevist Results for χ_m

VSM Measurement	Fitted MRI Result	Published Result [60]
2.06×10^{-6} m^3/kg Gd	1.8×10^{-6} m^3/kg Gd	2.13×10^{-6} m^3/kg Gd

5.3 Gradient Field Effects and Instability at 1.5 T

In examining the effect of the MRI's gradient fields at 1.5 T, it is worth noting that several factors can influence the behavior of the fluid's magnetic nanoparticles. These factors include the effect of the earth's gravitational field effects and van der Waals attractive forces between the particles. Following the analysis of Rosensweig [42] (pg. 36), the relative influence of gravity to magnetism is described by the ratio of (5.4) where $\Delta\rho$ is the difference in density between the fluid and the nanoparticles ($\approx$ 4300 kg·m^{-3} for magnetite particles [42]), g is acceleration due to gravity (9.8 m·s^{-1}), L is the characteristic dimension of the container in m, μ_0 is magnetic permeability of free space, M is the single domain magnetization of magnetite (446×10^3 A·m^{-1}) and H is the local magnetic field in A·m^{-1}.

$$\frac{GravitationalEnergy}{MagneticEnergy} = \frac{\Delta\rho\, g\, L}{\mu_0 M H} \tag{5.4}$$

For $\mu_0 H = 1.5$ T and a 5 cm container height, the ratio is 0.0025, indicating that gravitational forces are less of a threat to segregation than is the magnetic

field. The van der Waals forces arise spontaneously between neutral particles because of the fluctuating electric dipole-dipole forces that are always present. This force is inversely proportional to the seventh power of the radial distance, d, from the particle ($\propto d^{-7}$) and therefore is not as significant as the interparticle forces associated with magnetic force of attraction which is proportional d^{-3} [42], except when particles are already in very close proximity. Therefore, this section focusses on effects which are expected to be of relevance to MRI, namely the effects of the MRI gradient fields on ferrofluid suspensions and the possibility of chaining and clustering of the magnetic nanoparticles in MRI.

This section also analyzes the sensitivity of cylindrical vials of contrast agent to transverse fields, where the vial is collinear to the B_0 field. The purpose of this investigation is to estimate at what point the transverse field begins to give rise to a dipolar field pattern in the vicinity of the agent, as viewed using MRI. The investigation takes place using a 1.5 T system but the results are more generally applicable since the transverse field is normalized with respect to the effective B_0 field along the vial's axis.

5.3.1 Theory of Gradient Field Effects

The motion of a magnetic nanoparticle in a magnetic field is governed by the principle of conservation of linear momentum, as given in Eq. (5.5), where p' is the modified pressure, given by (2.20), p is the absolute pressure in Pa, g is the gravitational acceleration in $\mathrm{m{\cdot}s^{-2}}$, ρ is the ferrofluid mass density in $\mathrm{kg{\cdot}m^{-3}}$, ζ is the ferrofluid vortex viscosity in $\mathrm{N{\cdot}s{\cdot}m^{-2}}$ and η is the dynamic shear viscosity of the ferrofluid in $\mathrm{N{\cdot}s{\cdot}m^{-2}}$. As noted previously, the expression considers the situation of sinusoidal steady state with viscosity-dominated flow conditions (so that inertia is negligible)

and the ferrofluid only responds to force and torque densities which have a time-averaged, non-zero component.

$$-\nabla p' + \mu_0(\mathbf{M}\cdot\nabla)\mathbf{H} + 2\zeta\nabla\times\boldsymbol{\omega} + (\zeta+\eta)\nabla^2\boldsymbol{v} = 0 \tag{5.5}$$

Clearly, in the presence of a gradient in the magnetic field, the second term is non-zero and there is a linear force density in the direction of the gradient. Since such a gradient is the means by which the image is encoded in MRI, as outlined in Chapter 1, some order of magnitude calculations are undertaken here. Furthermore, should the effect be significant enough to cause motion within the ferrofluid, there is the potential to control such an effect by selecting the direction of the gradient [88–91].

5.3.2 Numerical Calculations

The force density term of Eq. (5.5), $\mu_0(\mathbf{M}\cdot\nabla)\mathbf{H}$, and the associated magnetic energy density, U_m, become significant when they are comparable to the thermal energy density, $U_t = kT$, such that the random thermal fluctuations are no longer dominant over the gradient-directed magnetic force density. Therefore, when the ratio U_m/U_t approaches unity, the effect of gradient field forces can be significant. The value of U_m is the integral of the second term in Eq. (5.5) and is given in Eq. (5.11), where x is the characteristic dimension over which the gradient is exerted. For an MRI of human vasculature containing SPIO contrast agent, this is typically on the order of centimeters. For simplicity, a linear flux density gradient, G_x, is assumed, such that G_x has units of $\mathrm{T{\cdot}m^{-1}}$. As previously defined, V_p is the magnetic volume of the particle, M_d is the single domain magnetization of the particle, which for magnetite has a value of 446×10^3 $\mathrm{A{\cdot}m^{-1}}$. It is also assumed that spatial variations in the magnetic field intensity are dominated by the applied magnetic flux density gradient

and any spatial variation in magnetization (associated with concentration gradients) are not comparable (*i.e.*, $\frac{B}{\mu_0} - M \approx \frac{B}{\mu_0}$). The ratio of the magnetic and thermal energy densities is finally given by Eq. (5.12)

$$U_t = kT \tag{5.6}$$

$$U_m = \int \mu_0 V_p M_d \frac{\partial H}{\partial x} dx \tag{5.7}$$

$$U_m = \int \mu_0 V_p M_d \frac{\partial}{\partial x} (\frac{B}{\mu_0} - M) dx \tag{5.8}$$

$$U_m \approx \int V_p M_d \frac{\partial B}{\partial x} dx \tag{5.9}$$

$$U_m \approx \int V_p M_d G_x dx \tag{5.10}$$

$$U_m \approx V_p M_d G_x x \tag{5.11}$$

$$\frac{U_m}{U_t} \approx \frac{V_p M_d G_x x}{kT} \tag{5.12}$$

The ratio is plotted for a number of typical gradient fields in MRI. On the typical 1.5 T and 3 T MRI systems, the Siemens' gradient system allows for gradients up to 40 $\mathrm{mT \cdot m^{-1}}$. Typical particle radii are considered and the results are included in Figures 5-8 and 5-9 for various gradients and particle radii. The energy density is plotted versus the characteristic dimension in each case.

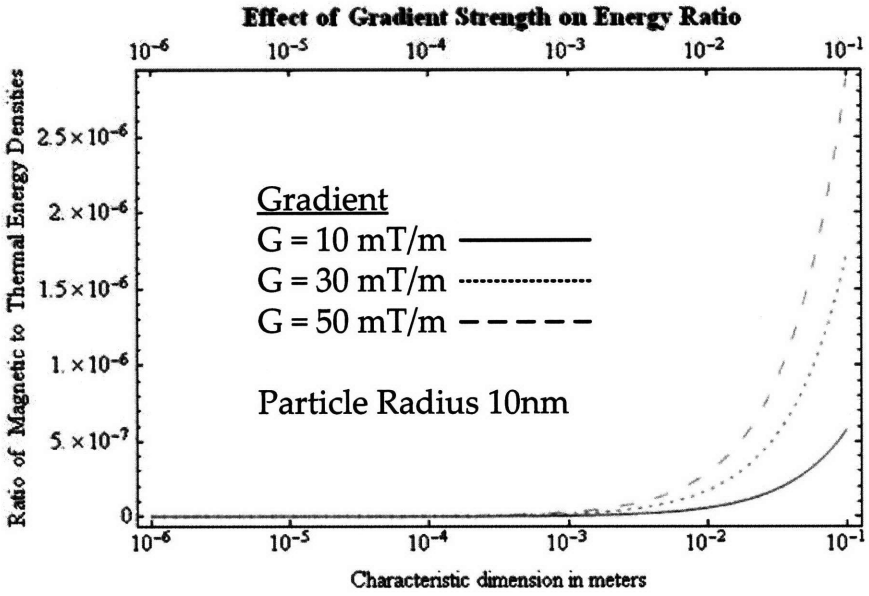

Figure 5-8: Ratio of Magnetic to Thermal Energy Densities for particles of 10 nm mean magnetic radius under varying gradient field conditions.

Inspection of Figures 5-8 and 5-9 shows that under no circumstances of realistic particle radii or gradient field is the magnetic energy density associated with the nanoparticles comparable to the thermal energy density, U_t. Accordingly, it is supposed that particle movement can be discounted as a source of image contrast due to the encoding gradient fields in MRI. However, this supposes that the particles remain discrete in the MRI environment and, as outlined in the following paragraphs, this is not necessarily the case due to chaining under conditions of high magnetic field. The potential for particle chaining and clustering is assessed in the following paragraphs.

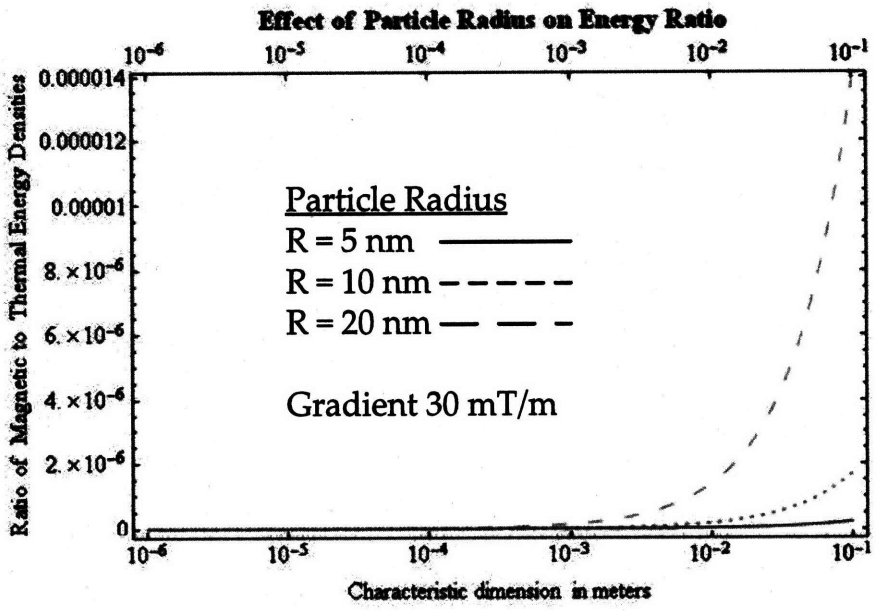

Figure 5-9: Ratio of Magnetic to Thermal Energy Densities for particles of varying magnetic radius in a magnetic flux density gradient of 30 $\mathrm{mT \cdot m^{-1}}$.

5.3.3 Clustering and Chaining Phenomena

Chaining of ferrofluids occurs when the dipole-dipole interaction between discrete particles is sufficient to overcome the steric repulsion associated with the particle's surfactant layer. The phenomena is more likely in strong external magnetic fields, such as those typical of MRI and when chaining occurs, the nanoparticles form long chains parallel to the applied field. Theoretical expressions, developed by de Gennes and Pincus [92], predict the mean number of particles per chain, N, depending on ferrofluid's concentration and physical parameters. The expression in the presence of large DC magnetic fields (such that the suspension is assumed to be saturated) is given by Eq. (5.13) where ϕ is the percentage solid volume in the suspension, and λ is given by Eq. (5.14).

$$N = (1 - \frac{2}{3}\frac{\phi}{\lambda^2} e^{2\lambda})^{-1}; \tag{5.13}$$

$$\lambda = \frac{\mu_0 M_d^2 V_p}{24 k T} \tag{5.14}$$

Typical contrast agents for MRI have values of ϕ in the range 10^{-7} to 10^{-5} *in vivo* (see Table B.1 of Appendix B) so chaining can be expected for particle sizes with magnetic radii in the range of 9 or 10 nm as predicted by Figure 5-10. Compartmentalization *in vivo* and improved steric hindrance may help alleviate chaining but this is a topic that has not been previously examined in the context of superparamagnetic contrast agents in MRI. The experimental results which follow this discussion use a value of $\phi = 0.004$ indicating that chaining is expected for any particles exceeding a magnetic radius of 6 or 7 nm. This value of ϕ is still over 3 orders of magnitude beyond the recommended dosage for Feridex, the only commercial SPIO agent, after dilution in the subject's bloodstream (see Table B.1 of Appendix B).

As noted by Rosensweig on page 68 of his text [42], only values of λ which exceed $+1$ are of physical significance. Chaining occurs very rapidly with increasing particle concentration. For a saturated ferrofluid, theoretical chain length can approach infinity. This is obviously non-physical due to the container constraints and compartmentalization that is inevitable *in vivo*.

5.3.4 Experimental work

While theoretical predications indicate that no individual particle motion is likely in the presence of the gradients typical of the MRI environment, the inevitable presence of some chains in the suspension might still result in a non-negligible magnetic

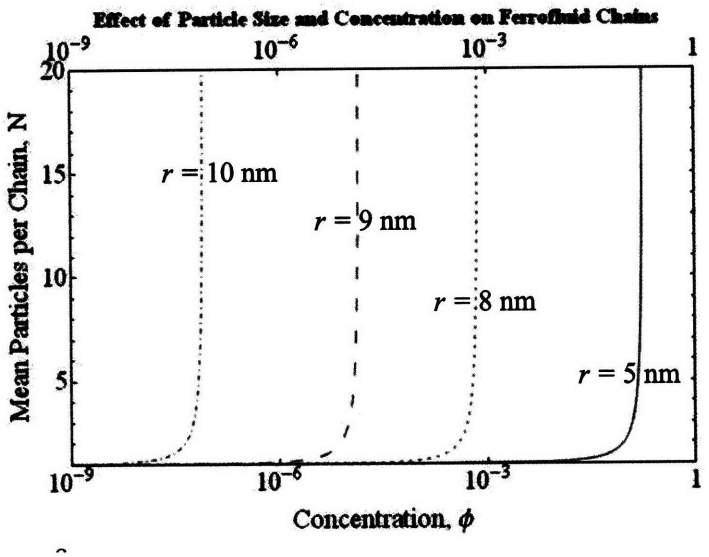

Figure 5-10: The dependence of mean number of particles per chain is shown for various mean particle radii. With reference to Table B.1, typical SPIO contrast agents (*e.g.*, Feridex) for MRI have values of ϕ in the range of 10^{-7} to 10^{-5} *in vivo*. The phenomenon of chaining occurs rapidly once particles of a given diameter are concentrated over a certain threshold.

force density. Experimental SPIO contrast agent was obtained[1] with a characteristic particle hydrodynamic radius of 10 nm and an estimated magnetic radius of 8 nm. The concentration was 15 mg Fe per ml corresponding to a fraction solid volume of approximately 0.004 when the particle volume is assumed to be 100% magnetite, corresponding to a concentration which is over 3 orders of magnitude greater than the recommended Feridex dosage after in vivo dilution (again, see Table B.1 of Appendix B). Since the specific mass of the typically hydrogen atom-rich surfactant coating used in the manufacture of SPIOs for MRI is about two orders of magnitude less than that of Fe, this is adjudged an acceptable approximation.

In order to induce linear motion in the ferrofluid contrast agent, the MRI sequence

[1]Sincere thanks is due to Dr. Young Kim at the Martinos Center for Biomedical Imaging for the use of his SPIO contrast agent.

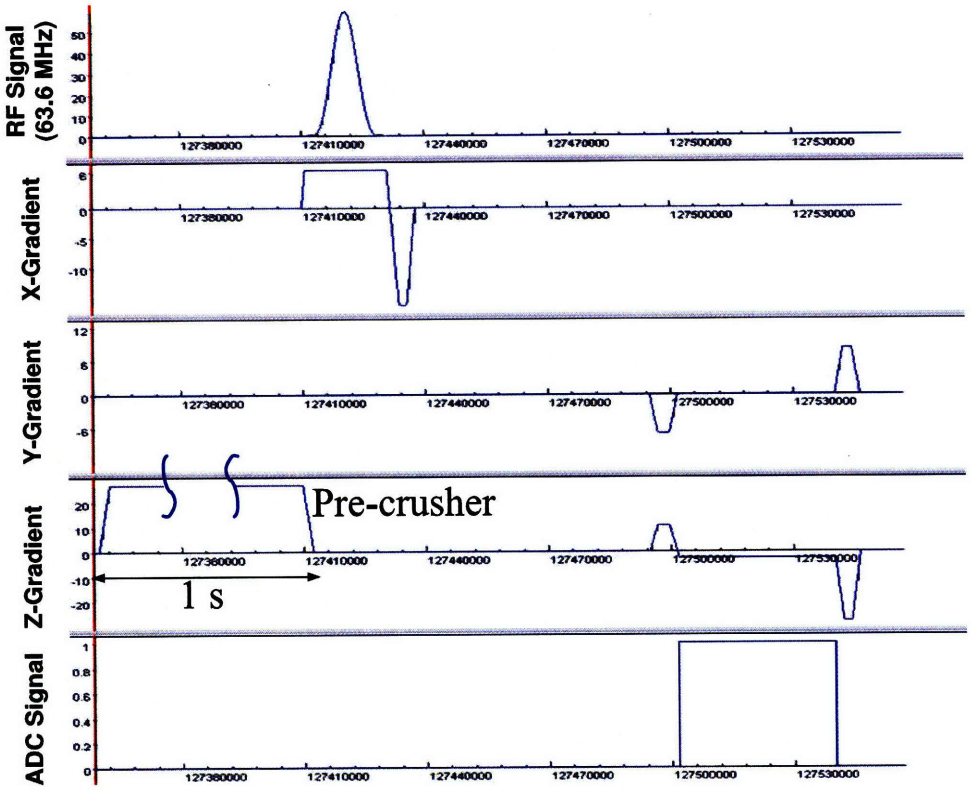

Figure 5-11: The timing diagram of the sequence used to investigate possible particle motion due to gradient fields by means of a pre-crusher pulse. In this example, the image is a sagittal slice so that the readout and pre-crusher are z-directed. The slice selection is along x and y is the phase-encode axis.

shown in Figure 5-11 was employed. The purpose of this excitation was to begin the movement of the nanoparticles in the ferrofluid prior to exciting the proton spins responsible for imaging. The "pre-crusher" was applied along the MRI readout direction with an amplitude that was limited by the physical constraints of the Siemens system. On the 1.5 T Siemens Trio, this is theoretically 40 $\text{mT}\cdot\text{m}^{-1}$ although in reality, the maximum used was 27 $\text{mT}\cdot\text{m}^{-1}$ due to the $\frac{\partial B}{\partial t}$ safety limits on the Siemens platform. Although an arbitrarily long pre-crusher time is possible, a value of 1 second was used.

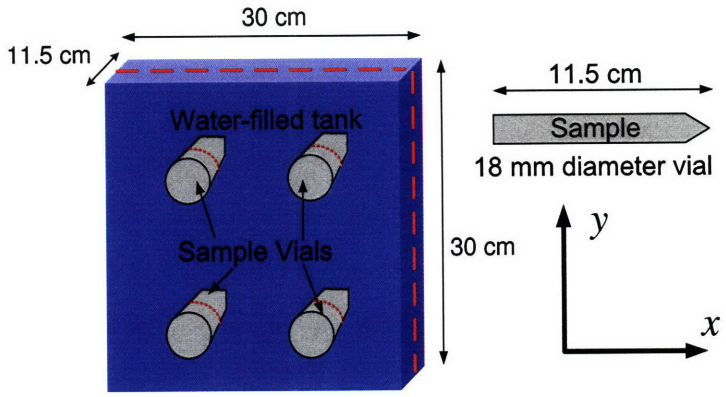

(a)

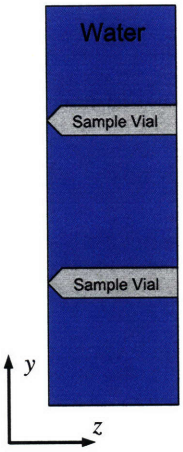

(b)

Figure 5-12: The vial orientation is shown for (a) sagittal and (b) coronal imaging positions.

After the end of the pre-crusher, a regular gradient-recalled echo (GRE) sequence was employed where the readout gradient was in the same direction as the pre-crusher.

Since the pre-crusher time is several orders of magnitude longer than the subsequent GRE excitation, the pre-crusher time has been shortened relative to the duration of the other gradients in the timing diagram of Figure 5-11 although a value of 1 s was used in the experiment. The total TR time of the GRE was 1200 ms with a flip angle of 15° and this was adjudged sufficient to allow sufficient relaxation of the imaging protons in the water between excitations. Although a true T2-weighted image would require TR$\gg$T1$\approx$3 s for water, TR=1.2 s allows sufficient SNR to support the conclusions which follow. The resolution was 256×256 pixels with a symmetric field of view of 300 mm. The readout bandwidth was 358 kHz (1400 Hz per pixel). The slice thickness varied with either sagittal (5 mm thick) or coronal (3 mm thick) imaging slices. The arrangement of long cylinders of ferrofluid in a water tank was employed as shown in Figure 5-12 for (a) sagittal and (b) coronal imaging. The cylinders were placed transverse to the B_0 field thus allowing for imaging slice cross-sections in both the coronal and sagittal orientations to investigate possible particle motion as outlined above. A control vial of water was placed adjacent to the ferrofluid vial in all experiments. Although larger imaging slices are desirable since SNR increases linearly with voxel size, a reduced slice thickness was used in coronal imaging to help mitigate against edge effects parallel to the cylinder's long axis. Clearly, this is not as much of a concern for sagittal imaging as the edge effects are due to the cylinder ends, and if the slice is chosen to be at the center of the cylinder, these should be reduced. For sagittal imaging, the readout and pre-crusher are z-directed. The slice selection is along x and y is the phase-encode axis. The image is a cross-sectional slice along the cylinder's short axis, transverse to the B_0 field in the $\{yz\}$ plane. In the following sagittal images, the y axis is vertical, from bottom to top, and the z axis is horizontal, from left to right. For the case of coronal imaging, slice selection is along the y axis,

phase encoding is along the x axis and the readout and pre-crusher are z-directed. The imaging slice is thus a cross-section along the cylinder's long axis, parallel to the B_0 field in the $\{xz\}$ plane. It is thought that any particle motion effects would be most evident in this orientation since the particles would have a longer characteristic dimension over which to diffuse. For the coronal images which follow, the x axis is vertical, from bottom to top, and the z axis is horizontal, from left to right.

In order to eliminate any confusion between effects due to inhomogeneities in the main B_0 field and effects due to the particle's motion, a so-called "B_0 map" was obtained using closely spaced TE times following the method described in Chapter 20 of Haacke's text [35]. The local resonant frequency, $\omega_0(x, y)$, is estimated by Eq. (5.15) where ΔTE is given by the difference in the two TE times and $\Delta\phi$ is the associated difference in the phase maps. In fact, the B_0 map is a measure of the local resonant frequency rather than the local B field in the absence of effects due to inhomogeneities associated with B_0. However, the two measures only differ by the constant factor, γ, the gyromagnetic ratio for the ^{1}H proton.

$$\omega_0(x, y) = \frac{\Delta\phi}{\Delta TE} \tag{5.15}$$

This work uses consecutive TE times of 3.9 and 4 ms allowing a frequency bandwidth of ± 5 kHz in the B_0 maps which follow. The phase maps show significant "phase wrapping", as is evident in Figures 5-13 and 5-15. Phase wrapping is the phenomenon where the frequency spectrum of the phase accumulated across the MRI image exceeds the bandwidth associated with $1/\Delta$TE used to estimate the phase map. When this occurs, phase wrapping results and the local phase shows discrete jumps of 2π radians whereas the real accumulated phase is continuous. Unwrapping these effects is an area of significant interest in MRI [35] but is not explored in any

detail in this work.

5.3.5 Phase and B_0 Maps

The phase maps of Figure 5-13 show sagittal slices for a center slice in both the control vial of deionized water (left) and the ferrofluid (right). The control vial is not readily visible since there is little or no phase shift associated with it. The left column shows the phase accumulated at TE = 3.9 ms and the right shows phase at TE = 4.0 ms. The top line is the phase in the absence of any pre-crusher. The middle line shows phase with the application of a positive pre-crusher of 1 s duration and an amplitude of 27 $\text{mT}\cdot\text{m}^{-1}$. The bottom line of images is the phase with a negative pre-crusher of the same amplitude. The resulting B_0 maps, as derived by Eq. (5.15) are shown in Figure 5-14 with a frequency scale of ± 5 kHz corresponding to $1/\Delta TE$. Since the pre-crusher is z-directed in the sagittal case, any particle motion is expected to be manifested in a shifting of the ferrofluid's dephasing pattern, to the left in the case of the positive crusher and to the right in the case of the negative crusher. No such shift is apparent and it is therefore concluded that there is no perceptible particle motion in the vial due to the MRI gradient fields. This result is in line with the predictions of Figures 5-8 and 5-9 where the characteristic length of the vial is 1.2 cm.

The phase maps of Figure 5-15 show the 2 coronal cross-sectional slices. Again, the left column shows the phase accumulated at TE = 3.9 ms and the right shows phase at TE = 4.0 ms. The top line is the phase in the absence of any pre-crusher. The middle line shows phase with the application of a positive pre-crusher of 1 s duration and an amplitude of 27 $\text{mT}\cdot\text{m}^{-1}$. The bottom line of images is the phase with a negative pre-crusher of the same amplitude. The resulting phase maps are shown in Figure 5-16. Since, in this case, the pre-crusher is z-directed, any particle motion is

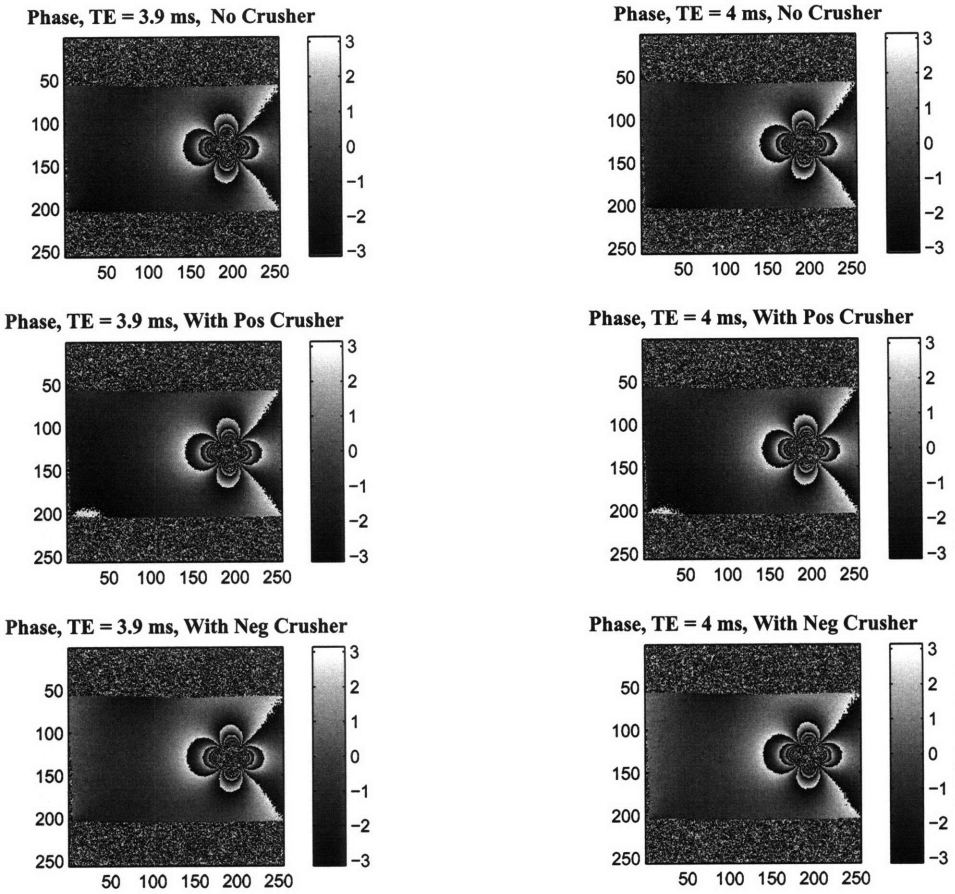

Figure 5-13: Phase maps (in radians) for sagittal imaging slices. The z axis is horizontal (left to right) and the y axis is vertical, from bottom to top. The pre-crusher and readout gradient are both z-directed. To the left of each ferrofluid vial is a control vial of deionized water. There is no perceptible change in the phase maps in the presence of the crushers indicating no gradient-induced magnetic force on the particles.

again expected to be seen in a shifting of the ferrofluid's dephasing pattern, to the left in the case of the positive crusher and to the right in the case of the negative crusher. As for the sagittal images, no such shift is apparent and it is therefore concluded that there is no perceptible particle motion in the vial due to the MRI gradient fields. Furthermore, while chaining may be present, it does not seem to represent a source of particle motion in MRI gradient fields.

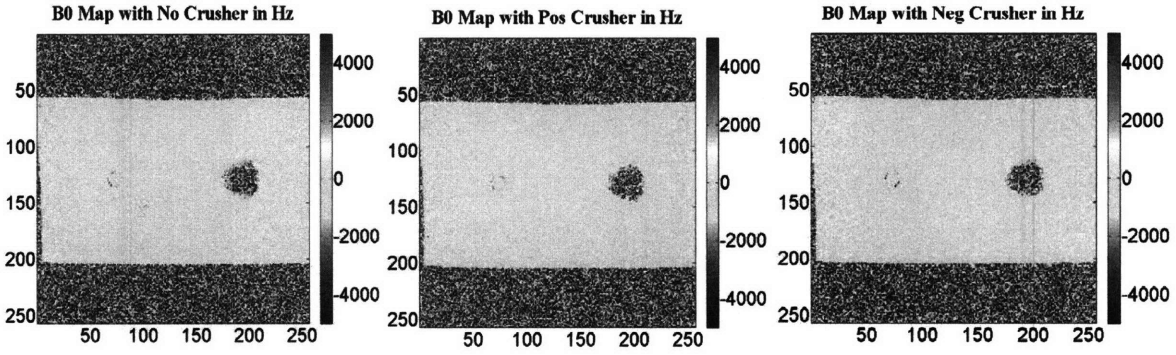

Figure 5-14: B_0 maps are shown for each of the three cases considered with a sagittal viewing slice: (i) in the absence of a pre-crusher, (ii) in the presence of a positive pre-crusher and (iii) in the presence of a negative pre-crusher. No perceptible change was observed in the presence of the pre-crusher.

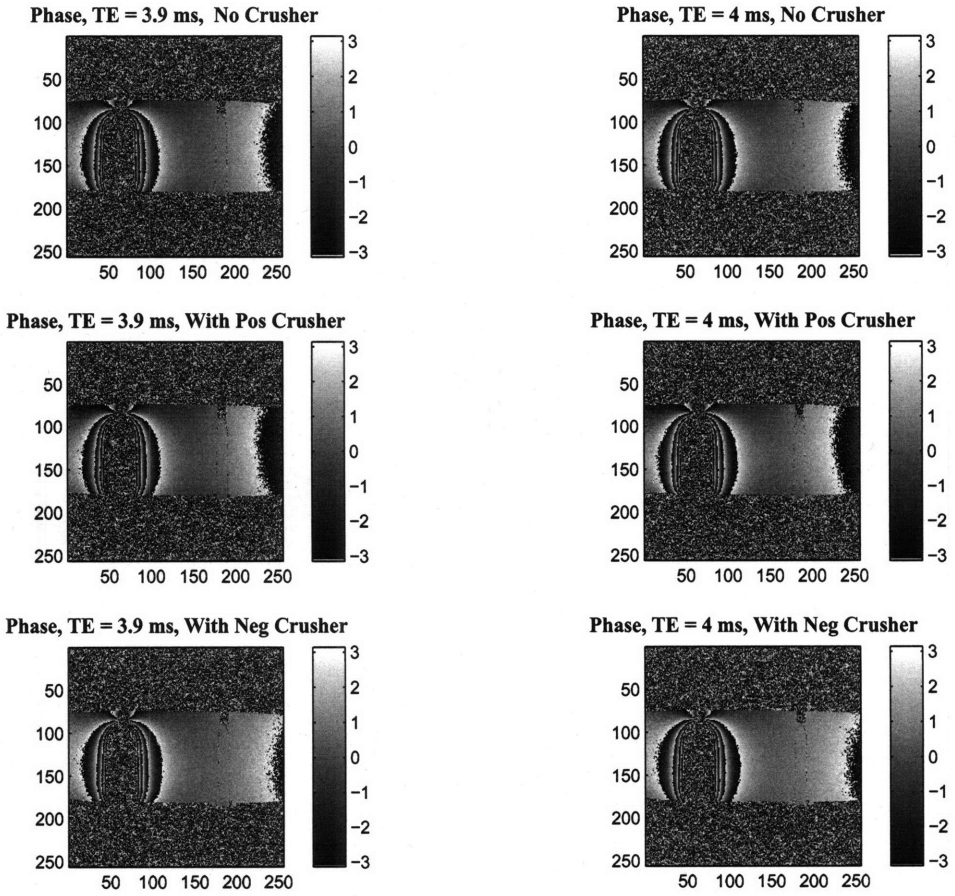

Figure 5-15: Phase maps for coronal (xz) slice images. The z axis is horizontal (left to right) and the x axis is vertical, from bottom to top. The pre-crusher and readout gradient are both x-directed. The control vial of deionized water lies to the right of the ferrofluid vial.

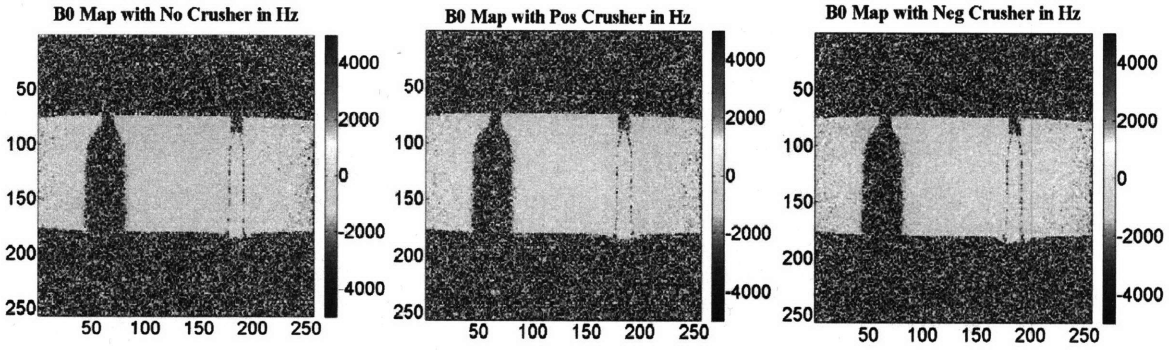

Figure 5-16: B_0 maps are shown for each of the three cases considered with a coronal viewing slice: (i) in the absence of a pre-crusher, (ii) in the presence of a positive pre-crusher and (iii) in the presence of a negative pre-crusher. The control vial of deionized water lies to the right of the ferrofluid vial. As in the previous case, no significant change in the B_0 maps was observed due to the pre-crusher.

5.3.6 Sensitivity to Transverse Fields

In order to estimate the sensitivity of the SPIO contrast agent to transverse magnetic fields, a vial of agent was placed parallel with the main field at 1.5 T and a series of experiments were undertaken. These involved positioning the vial at various angles of inclination (denoted θ where $\tan\theta$ is the ratio of the transverse to longitudinal components) to the main B_0 field such that there exists components both parallel and perpendicular to the vial's principal axis. The arrangement is simplified in Figure 5-17 where the vial is represented by an ideally infinite cylinder of radius R.

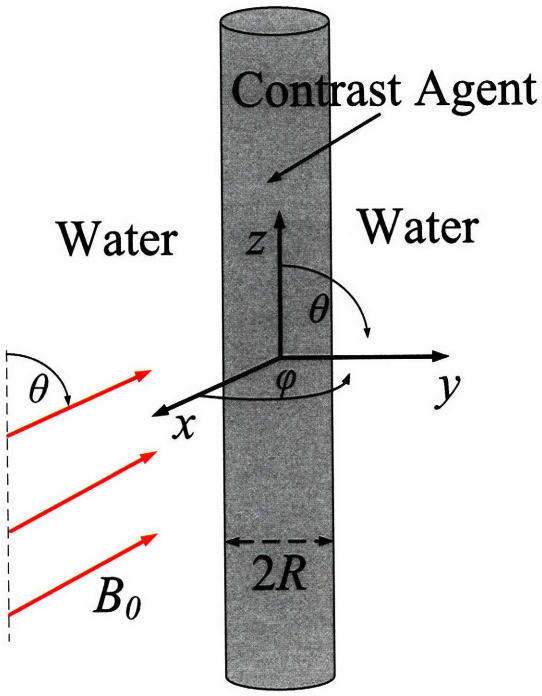

Figure 5-17: The angle between the applied B_0 field and vial's axis is denoted θ. Edge effects are neglected by assuming that the vial is infinitely long.

Four different orientations were investigated, as noted in Table 5.3, where the ratio

of the transverse to axial components is simply given by the tangent of the angle to the B_0 field.

Table 5.3: Table of Field Components as a Function of Angle, θ to B_0

Angle to B_0 in degrees	Transverse to Longitudinal Field Ratio
0	0
5.8	0.102
12.8	0.227
17.8	0.321

In the MRI imaging results which follow, the parameters are given in Table 5.4, except for the case where the angle of inclination is 0°, the resolution is 128×72 and TR = 500 ms.

Table 5.4: Table of MRI Parameters for B_0 experiments

Parameter	Value
Resolution	128×84
Slice Thickness	10 mm
TR	100 ms
TE	as indicated
Number of averages	1
Bandwidth per pixel	1955 Hz/Pixel
Flip Angle	25°
FOV	183 mm×280 mm

In each case, the bandwidth was maximized to minimize the effect of B_0 inhomogeneities. The low spatial resolution is a trade-off with short TE times, so the slice thickness is increased in order to increase SNR. The presence of edge effects and artifacts due to such a large slice thickness is subsequently accessed. A relatively low flip angle allows for shorter TR times and there is no expectation that increasing TR

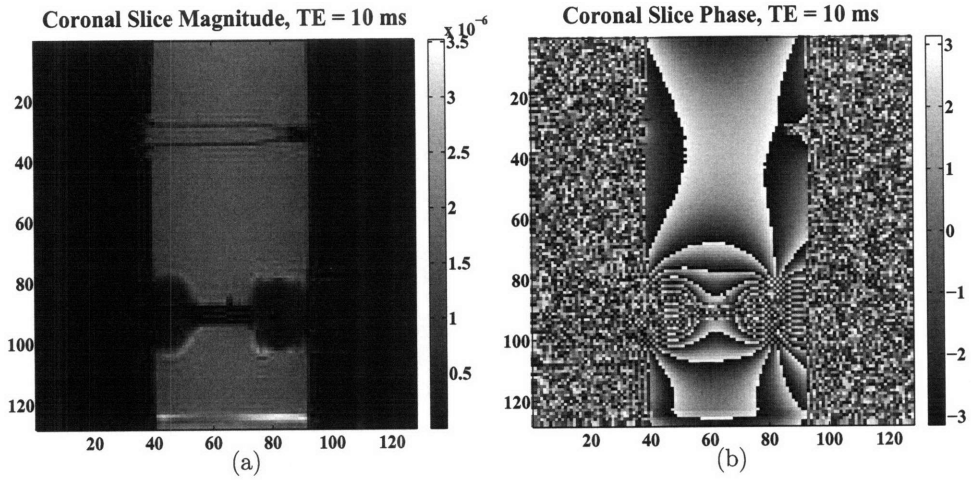

Figure 5-18: Magnitude (a) and phase (b) images collected when the vial is parallel to the main B_0 field with a coronal imaging view.

beyond 100 ms would significantly improve SNR.

5.3.7 Fringing Fields and Edge Effects

To investigate the fringing fields associated with the ends of the vial and the edge effects due to the surrounding walls of the water tank, the vial was imaged in a coronal orientation such that the imaging slice was in the $\{xz\}$ plane. The echo time was allowed to run to 10 ms to exaggerate any effects due to either the edges or the vial ends. The TR value is 100 ms and the field-of-view is 300 mm $\times$ 300 mm. The spatial resolution is 128 $\times$ 128 with a sagittal slice thickness of 5 mm and a readout bandwidth of 1955 Hz/pixel. The large readout bandwidth and short TE are used to minimize B_0 inhomogeneity effects from affecting the image. The resulting magnitude and phase images are shown in Figure 5-18.

The magnitude plot of Figure 5-18(a) shows that there is little disturbance of the image magnitude at the water vial, except due to edge effects from the perspex container and the end clamps. The vial of contrast agent shows significant end effects

at each end of the vial as expected but, again, the magnitude is largely unchanged at the center of the vial. The phase plot of Figure 5-18(b) shows some end effects for the water vial but nothing significant at the vial's center. The contrast agent vial shows significant phase disturbance at the vial center with widespread "phase wrapping" as evidenced by the alternating black, then white phase patterns as the phase flips from $-\pi$ to $+\pi$. The effect will be clearly seen regardless of how thin the transversal imaging slice becomes due to the severity of the wrapping and this is confirmed in the results of Figure 5-19 which follow.

5.3.8 Phase Maps and B_0 Fields

A series of phase maps were collected and the associated B_0 maps were estimated as previously outlined. The phase maps were collected for various short TE values to ensure a heavy T2* weighting in all the resultant images. The slice of most interest is that at the vial's center with a transversal orientation, such that it is always orthogonal to the vial's principal axis. The theoretical solution for the magnetic field and flux density inside and outside the vial is described below.

Theoretical Field Solutions

The problem under consideration is that of Figure 5-17. The main B_0 field is inclined at an angle θ to the vial's axis such that there are components of the main field applied along both the y and z axes given by $B_0 \sin\theta$ and $B_0 \cos\theta$ respectively. The vial of contrast agent is assumed to be of infinite extent along z and the agent is assumed saturated with a saturation magnetization of M_0 in A/m aligned with the B_0 field where M_0 is given by ϕM_s and M_s is the saturation magnetization of the magnetite. The percentage solid volume in the agent is denoted ϕ. The condition of

saturation is easily met when imaging at typical clinical fields of 1.5 and 3 T.

The resulting field solutions for the regions $0 < r < R$ and $r > R$ where R is the vial's radius and r is the radial distance from the center of the vial, is a combination of the effects due to the transverse field along $\boldsymbol{i}_y$ and the axial field along $\boldsymbol{i}_z$. The axial solution is trivial and the z-components are given in Eq. (5.16) and (5.17) by virtue of continuity of the tangential H field at $r = R$.

$$B_z = \begin{cases} B_0 \cos\theta + \mu_0 M_0 \cos\theta & \text{for} \quad 0 < r < R \\ B_0 \cos\theta & \text{for} \quad r > R \end{cases} \tag{5.16}$$

$$H_z = \begin{cases} \frac{B_0}{\mu_0} \cos\theta & \text{for} \quad 0 < r < R \\ \frac{B_0}{\mu_0} \cos\theta & \text{for} \quad r > R \end{cases} \tag{5.17}$$

The solutions for the y components are more involved. For an infinite vial, simplification arises with the consideration of a cylindrical coordinate set and the definition of a transverse magnetic potential which takes the form of Eq. (5.18) for a non-conducting, uniformly magnetized medium. The expression follows from $\nabla \boldsymbol{H} = -\nabla \boldsymbol{M}$ which is identically zero when $\boldsymbol{M}$ is uniform in space. Under this condition of uniform $\boldsymbol{M}$, the expression of Eq. (5.18) is true where $\boldsymbol{H} = -\nabla\Psi$.

$$\nabla^2\Psi = 0 \tag{5.18}$$

Eq. (5.18) has solutions in an azimuthal-symmetric geometry such as that of Figure 5-17 as given by Eq. (5.19) where A, B, C and D are constants to be evaluated by means of boundary conditions at $r = R$ and $\nabla\Psi = \mathbf{H}$.

$$\Psi(r,\varphi) = \begin{cases} (Ar + \frac{B}{r})\sin\varphi & \text{for} \quad 0 < r < R \\ (Cr + \frac{D}{r})\sin\varphi & \text{for} \quad r > R \end{cases} \tag{5.19}$$

Since Ψ cannot yield infinite field solutions at $r = 0$, we conclude that $B = 0$. Therefore, the y-component of $\mathbf{H}$ might be written using the del operator in cylindrical coordinates, as in Eq. (5.20), where $\boldsymbol{i}_r$ and $\boldsymbol{i}_\varphi$ are unit vectors in the cylindrical coordinate system.

$$H_y(r,\varphi) = \begin{cases} A\sin\varphi\boldsymbol{i}_r + A\cos\varphi\boldsymbol{i}_\varphi & \text{for} \quad 0 < r < R \\ (C - \frac{D}{r^2})\sin\varphi\boldsymbol{i}_r + (C - \frac{D}{r^2})\cos\varphi\boldsymbol{i}_\varphi & \text{for} \quad r > R \end{cases} \tag{5.20}$$

The y-component of the $\mathbf{B}$ field solutions are given by Eq. (5.21).

$$B_y(r,\varphi) = \begin{cases} \mu_0(H_y(r,\varphi) + M_y(r,\varphi)) & \text{for} \quad 0 < r < R \\ \mu_0 H_y(r,\varphi) & \text{for} \quad r > R \end{cases} \tag{5.21}$$

The constants are solved by considering the boundary conditions as follows where $B_y = B_0\sin\theta$ and $M_y = M_0\sin\theta$.

- $B_r(r = R^-) = B_r(r = R^+)$
- $H_\varphi(r = R^-) = H_\varphi(r = R^+)$
- $\mathbf{H}(r \to \infty) = \frac{B_y}{\mu_0}\boldsymbol{i}_y = \frac{B_y}{\mu_0}(\sin\varphi\boldsymbol{i}_r + \cos\varphi\boldsymbol{i}_\varphi)$

Applying these boundary conditions to Eqs. (5.20) and (5.21) yields the following solutions for A through D as given by Eqs. (5.22) through (5.24).

$$A = \frac{B_y}{\mu_0} - \frac{M_y}{2} \tag{5.22}$$

$$C = \frac{B_y}{\mu_0} \tag{5.23}$$

$$D = \frac{M_y R^2}{2} \tag{5.24}$$

Substitution yields the complete solution for the **H** and **B** fields by combining these solutions for the transverse fields with the solutions of Eqs. (5.16) and (5.17) where $B_y = B_0 \sin\theta$, $M_y = M_0 \sin\theta$, $B_z = B_0 \cos\theta$ and $M_z = M_0 \cos\theta$.

$$\mathbf{H} = \begin{cases} \frac{B_z}{\mu_0}\boldsymbol{i}_z + (\frac{B_y}{\mu_0} - \frac{M_y}{2})\boldsymbol{i}_y & \text{for} \quad 0 < r < R \\ \frac{B_z}{\mu_0}\boldsymbol{i}_z + \frac{B_y}{\mu_0}\boldsymbol{i}_y + \frac{M_y R^2}{2r^2}(\sin(2\varphi)\boldsymbol{i}_x - \cos(2\varphi)\boldsymbol{i}_y) & \text{for} \quad r > R \end{cases} \tag{5.25}$$

$$\mathbf{B} = \begin{cases} (B_z + \mu_0 M_z)\boldsymbol{i}_z + (B_y + \frac{\mu_0 M_y}{2})\boldsymbol{i}_y & \text{for} \quad 0 < r < R \\ B_z\boldsymbol{i}_z + B_y\boldsymbol{i}_y + \frac{\mu_0 M_y R^2}{2r^2}(\sin(2\varphi)\boldsymbol{i}_x - \cos(2\varphi)\boldsymbol{i}_y) & \text{for} \quad r > R \end{cases} \tag{5.26}$$

The solution is plotted for various values of φ and the results are shown in the plots which follow along with the accompanying experimental imaging results.

Experimental Imaging Results

When the vial is aligned with the B_0 field, the image results are shown in Figure 5-19. The images all capture the center of the vial with a transversal view, or the $\{xy\}$ plane in Figure 5-17. The phase map of Figure 5-19(a) shows significant shading in the water region surrounding the vial of contrast agent (rightmost vial) which is not present for the water vial. This is to be expected for a 10 mm slice given

the pronounced edge effects shown in Figure 5-18. The B_0 map of Figure 5-19(b) shows some inhomogeneity to the right of the contrast agent but, on the whole, is reasonably uniform in the water region surrounding the two vials. It is assumed that any disturbance to the phase maps are due to susceptibility effects caused by the contrast agent and not due to B_0 inhomogeneities. The theoretical solution for transverse magnetic flux density, plotted using *Comsol Multiphysics* and shown in Figure 5-19(c) along $\boldsymbol{i}_y$, is zero when the vial is aligned with the B_0 field.

In the MRI system, the vial is rotated to achieve the angle effect. At an angle of $\theta = 5.8°$, the imaging results are shown in Figure 5-19(d)-(f). This value of θ corresponds to an applied transverse flux density which is 10.2% of the axial magnetic flux density. As well as the previously noted shading, there appears a clear dipolar phasing pattern around the vial of contrast agent in Figure 5-19(d). There is also some evidence of phase wrapping as signified by abrupt change from $-\pi$ to $+\pi$ above and below the vial of contrast agent. No such dipole pattern is evidenced around the water vial, so it is assumed that the disturbance correlates to the theoretical transverse dipolar field solution shown in Figure 5-19(f). Again, no significant B_0 inhomogeneity effects are found, as shown in the B_0 map of Figure 5-19(e).

Increasing the angle θ to 12.8°, the imaging results, given by Figure 5-19(g)-(i) show increased dipolar-shaped field disturbance due to the increased component of B_0 that lies perpendicular to the vial's principal axis. This value of θ corresponds to an applied transverse flux density which is 22.7% of the axial magnetic flux density. The experimental imaging results of Figure 5-19(g) and the predicted theoretical field pattern of Figure 5-19(i) correlate closely. Furthermore, the presence of B_0 inhomogeneities is again discounted as a source of dephasing as evidenced by Figure 5-19(h).

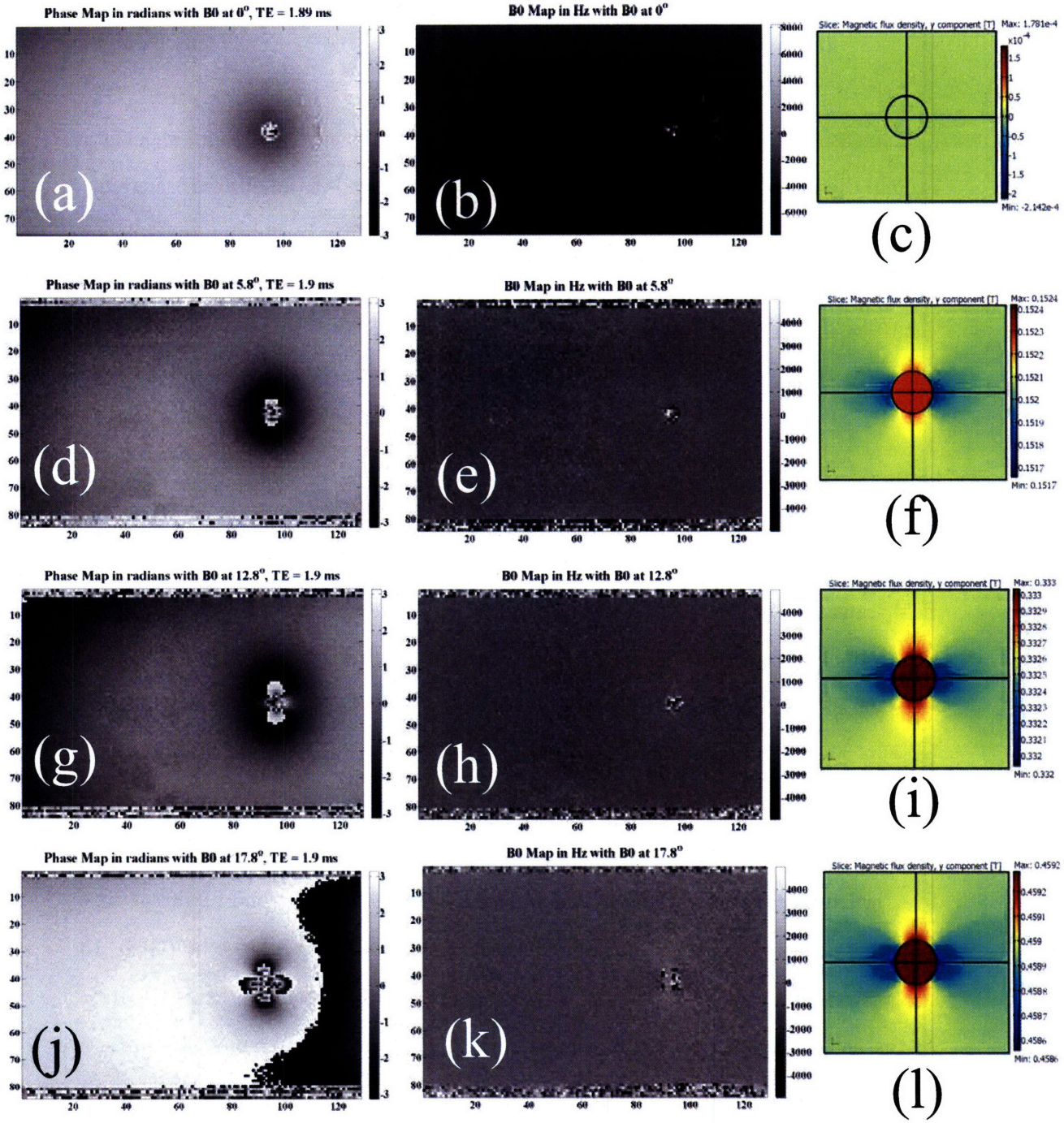

Figure 5-19: Phase Maps, (a),(d),(g) and (j), and B_0 maps, (b),(e),(h) and (k), collected when the vial is at various angles to the main B_0 field. The theoretical transverse magnetic flux density was plotted using Comsol and shown in (c),(f),(i) and (l). The angle of inclination is 0° for (a)-(c), 5.8° for (d)-(f), 12.8° for (g)-(i) and 17.8° for (j)-(l). The phase maps only show changes parallel to the B_0 field.

Increasing θ again, now to 17.8° results in a further increased dipolar pattern around the vial of contrast agent. This value of θ corresponds to an applied transverse flux density which is 32.1% of the axial magnetic flux density. In addition to the lobes above and below the vial in Figure 5-19(j), the lobes to the right and left are now clearly visible also. Again the result is closely correlated to the theoretical solution in Figure 5-19(l) with little or no B_0 inhomogeneity effects as shown in Figure 5-19(k).

Comments on Sensitivity to Transverse Fields

The purpose of the preceding experiment was to evaluate the effects of a magnetic field transverse to the vial's principal axis by tilting the vial in a 1.5 T MRI system. Two principal conclusions were reached. Firstly, the presence of dephasing due to edge effects is unavoidable with the current vial and test setup. This results in the shading around the vial of contrast agent in a T2*-weighted image when the vial is parallel to the B_0 field. While this effect is eliminated by means of a spin-echo experiment (see Chapter 1), it would also be alleviated with the use of vials of a greater length:radius ratio and by thinner imaging slices. The second finding is that sensitivity of the MR image intensity and phase in a gradient-recalled echo (GRE) to a transverse field was only just visible when the field represented approximately 10% of the field along the vial's axis. This finding has implications for any effort to use the transverse concomitant fields as a source of increased sensitivity in contrast agent detection. It is also worth noting that any approach that employs the transverse fields due to concomitance in Maxwell's Equations will have to be used outside of the saturation region of the agent, such that there exist some transverse component of susceptibility in order to see an imaging effect. Physically, this means the experiment would only be effective at modulating MR image intensity and phase at low-field open

MRI systems which typically operate at 0.2 or 0.35 T.

Chapter 6

Linear Forces on Magnetic Fluid Flow in MRI

6.1 Introduction

With the development of high-field MRI (*e.g.*, 3 T and 7 T human scanners), the potential for significant magnetic forces on magnetic fluids in MRI has increased. Prior work (Ch. 5) has assessed the force associated with the magnetic gradients in MRI. The purpose of this chapter of the thesis was to assess the potential impact of commercial gadolinium and SPIO contrast agents (Magnevist and Feridex) on *in vivo* blood flow in the presence of the large fringing field associated with high field MRI. The effects at both 3 T and 7 T systems were investigated using a flow phantom to replicate *in vivo* flow. The investigations consider pressure-driven Poiseuille flow in a long pipe. The flow velocity was examined in the presence and in the absence of the B_0 magnetic field for a variety of pressure conditions. The effect of varying contrast agent concentration and B_0 was also examined. The results show that neither agent

present measurable magnetic forces on blood flow *in vivo* even when three times the recommended dosage is administered (*i.e.*, 0.3 mmol Gd/kg for Magnevist and 0.03 mmol Fe/kg for Feridex, as given in Appendix B).

6.2 Theory of Magnetic Fluid Flow in MRI

Magnetomotive forces in magnetic fluid flow are governed by Maxwell's Equations, the conservation of linear momentum (6.1), and conservation of angular momentum (6.2) [42,97] where p is the pressure in Pa, ρ is the fluid mass density in kg·m^{-3}, ζ is the fluid vortex viscosity in N·s·m^{-2}, η is the dynamic shear viscosity in N·s·m^{-2}, $\mathbf{J}$ is the fluid's current density in A·m^{-2} (for conductive fluids), $\mathbf{I}$ is the moment of inertia per unit volume in kg·m^{-1}, $\mathbf{M}$ is the fluid's magnetization in A·m^{-1}, $\mathbf{H}$ its magnetic field intensity in A·m^{-1} and μ_0 the magnetic permeability of free space with a value of $4\pi \times 10^{-7}$ H/m. The flow velocity, $\boldsymbol{v}$, and so-called spin-velocity, $\boldsymbol{\omega}$, depend on the flow regime. In the linear limit, $\mathbf{M}$ and $\mathbf{H}$ are collinear and related, in the low field limit, by the susceptibility where $\mathbf{M} = \chi\mathbf{H}$. Spin-velocity will exist for flows with vorticity or when $\mathbf{M}$ and $\mathbf{H}$ become misaligned, resulting in a magnetic torque density acting to realign the magnetization and the magnetic field [42,97]. For incompressible flows, the divergence of the flow velocity is zero (*i.e.*, $\nabla \cdot \boldsymbol{v} = \mathbf{0}$).

$$-\nabla p + \mu_0(\mathbf{M}\cdot\nabla)\mathbf{H} + 2\zeta\nabla\times\boldsymbol{\omega} + (\zeta+\eta)\nabla^2\boldsymbol{v} + \mu_0\mathbf{J}\times\mathbf{H} = \rho\left(\frac{\partial \boldsymbol{v}}{\partial t} + (\boldsymbol{v}\cdot\nabla)\boldsymbol{v}\right) \quad (6.1)$$

$$\mu_0(\mathbf{M}\times\mathbf{H}) + 2\zeta(\nabla\times\boldsymbol{v} - 2\boldsymbol{\omega}) = \mathbf{I}\left(\frac{\partial \boldsymbol{\omega}}{\partial t} + (\boldsymbol{v}\cdot\nabla)\boldsymbol{\omega}\right) \quad (6.2)$$

Of particular interest are long cylindrical vessels, typical of the human leg vasculature, where Poiseuille flow dominates. These vessels may be exposed to high $\nabla \mathbf{H}$ effects in the fringe fields of MRI since, in the course of a typical MRI scan of the head or upper torso, the legs lie in the region of rapidly decreasing magnetic field intensity. The situation is illustrated in Figure 6-1 for the 3 T and 7 T Siemens MRI systems [104]. While Figure 6-1 shows the magnetic flux density, $\mathbf{B}$ (in Tesla) as a function of space, the strength of the main field in MRI is such that, for all realistic clinical scenarios, $\mathbf{M} \ll \mathbf{H}$ where $\nabla \mathbf{B} = \mu_0 \nabla(\mathbf{H} + \mathbf{M})$ and, therefore, $\nabla \mathbf{B} \approx \mu_0 \nabla \mathbf{H}$.

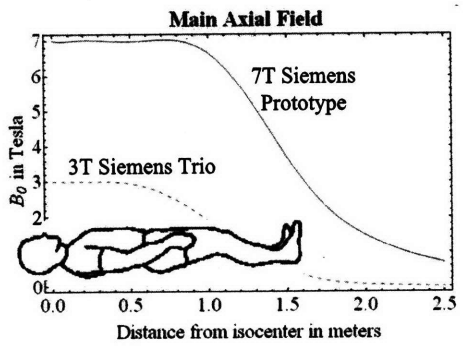

Figure 6-1: Fringing fields associated with the 3 T and 7 T Siemens MRI systems [104] are plotted as a function of distance (in meters) from the isocenter of the MRI magnet. For a typical MRI of the head, the subject (typically ≈ 1.7 m in length) is positioned as shown with the head at the magnet's isocenter ($z = 0$) where the B_0 field is most uniform.

The work which follows assumes steady state conditions so that all time-varying terms in (6.1) and (6.2) may be ignored. In addition, for z-directed pipe flow which only varies spatially in the radial direction along the pipe, the convective effects on the right hand side of (6.1) and (6.2) are zero. Under conditions of magnetic saturation, $\mathbf{M}$ and $\mathbf{H}$ are almost colinear so that $\mathbf{M} \times \mathbf{H}$ in (6.2) is also zero for any conventional MRI system (*i.e.*, $B_0 > 1$T). The spin-velocity only becomes comparable to pressure differentials typical *in vivo* when either the vorticity effects are considerably

increased or in the presence of a rotating magnetic field which might misalign the vectors $\mathbf{M}$ and $\mathbf{H}$ [97]. Neither scenario is considered in this work. Therefore, the spin-velocity is given by half the vorticity (*i.e.*, $\boldsymbol{\omega} = \frac{1}{2}\nabla \times \boldsymbol{v}$). Contrast agents, as well as human blood, do not have negligible conductivity [98] as is commonly assumed. However, since the magnetic Reynolds' Number in this experiment [99] (given by $\sigma\mu v l \approx (10^{-6})(\mu_0)(1)(1.8) \approx 10^{-5}$ where l is the longest dimension of interest (pipe length) and μ is the magnetic permeability) is very small, $\mathbf{J}$, the fluid's current density is also set to zero. Considering all these simplifications, (6.1) and (6.2) can be combined into the single expression, given by (6.3).

$$-\nabla p + \mu_0(\mathbf{M} \cdot \nabla)\mathbf{H} + \eta\nabla^2\boldsymbol{v} = 0 \tag{6.3}$$

Initially, the viscosity of the suspension was assumed to be given by the viscosity of the solvent, taken to be pure water at 20°C with a value of $\eta = 0.001$ N·s·m^{-2} [105]. However, since the viscosity is a strong function of temperature, decreasing to 0.0008 N·s·m^{-2} [105] at 30°C, these changes had to be subsequently considered in the work since the temperature changed considerably (up to 8°C or 10°C depending on the conditions) from inside to outside of the MRI field. This dependence led to misinterpretation of early results although the anomaly was eventually resolved.

The flow was considered fully developed, laminar, Poiseuille flow in the z-direction along the entire pipe. Since pressure increases in the positive z direction (*i.e.*, $\frac{\partial p}{\partial z} > 0$), the flow was in the negative z direction, as indicated in Figure 6-2. The analytical expression in the absence of the MRI field is given by (6.4) where r_n is the pipe radius [105] and r is the radial distance from the pipe's center.

$$v_z(r) = -\frac{r_n^2}{4\eta}\frac{\partial p}{\partial z}\left(1 - \frac{r^2}{r_n^2}\right) \tag{6.4}$$

For such flow, the average and maximum flow velocities are related by a factor of 2 [105], so that the average velocity, v_{av} is given by (6.5)

$$v_{av} = -\frac{r_n^2}{8\eta}\frac{\partial p}{\partial z} \tag{6.5}$$

In the presence of a gradient in the magnetic field (as shown in Figure 6-2), the solution is given by (6.6). Under virtually all conditions, $\mu_0 M \ll B_0$ and the expression reduces to (6.7). The velocity is negative since it flows in the negative z direction. In each case, the value of M depends on the agent. For the recommended Feridex dose, the effective *in vivo* magnetization is $M = \phi M_d = 1.115$ A·m^{-1}, where $M_d = 446 \times 10^3$ A/m and the unitless solid fraction, $\phi = 2.6 \times 10^{-6}$ as given in Table B.1.

$$v_{av} = -\frac{r_n^2}{8\eta}\left(\frac{\partial p}{\partial z} - \mu_0 M\frac{\partial H_0}{\partial z}\right) \tag{6.6}$$

$$v_{av} \approx -\frac{r_n^2}{8\eta}\left(\frac{\partial p}{\partial z} - M\frac{\partial B_0}{\partial z}\right) \tag{6.7}$$

As long as the B_0 field is sufficiently large that the Feridex remains in magnetic saturation, the magnetization is independent of field strength so that (6.7) can be rewritten as (6.8) where the bracketed term represents the modified pressure in the presence of the B_0 field.

$$v_{av} \approx \frac{r_n^2}{8\eta}\frac{\partial}{\partial z}\Big(-p + M\,B_0(z)\Big) \tag{6.8}$$

For Gd agents, the magnetization, M, is given by $\chi H \approx \chi B_0/\mu_0$. Since B_0 is a function of z, the magnetization is also a function of z for Gd agents. In this case, (6.7) can again be rewritten as given in (6.9) where the bracketed term is the modified fluid pressure due to the Gd contrast agent.

$$v_{av} \approx \frac{r_n^2}{8\eta}\frac{\partial}{\partial z}\left(-p + \frac{\chi}{2\mu_0} B_0^2(z)\right) \tag{6.9}$$

6.2.1 Measuring Magnetization

In the presence of a known pressure differential driving the fluid flow, the only remaining unknown quantity required to determine the expected fluid flow velocity from (6.3) is the magnitude of the contrast agent's magnetization, M. Gadolinium agents remain magnetically unsaturated up to main fields of about 50 T [25] so that the agent's magnetization is linearly proportional to the applied magnetic field intensity, $\mathbf{H}$ with the constant of proportionality being the magnetic susceptibility. Assuming that the agent's magnetization is significantly less than the strength of the main field ($M \ll B_0/\mu_0$), then the Gd agent's magnetization is given by (6.10), where C_m is the agent concentration in kg Gd/m^3 of solvent and χ_m is the mass susceptibility in m^3/kg.

$$M \approx \chi_m \frac{B_0}{\mu_0} C_m \tag{6.10}$$

The Magnevist's magnetization was investigated independently using a vibrating sample magnetometer (VSM) and MRI as detailed in Chapter 5 of this thesis. The results were a mass susceptibility of 2.06×10^{-6} m^3/kg Gd from VSM compared with 1.8×10^{-6} m^3/kg Gd for MRI. The prescribed dosage for Magnevist is 0.1 millimoles of agent per kg bodyweight [61]. However, recognizing that each mole of the agent (which has the complex molecular composition $C_{28}H_{54}GdN_5O_{20}$) corresponds to approximately the same mass as six moles of Gd, the recommended dosage is 0.6 millimoles Gd per kg. After the agent is injected into the subject, it is diluted in the subject's blood pool, which acts as the agent's solvent. For *in vivo* administration to a

normal, healthy adult with a total blood volume of 79 ml per kg bodyweight [103], this corresponds to 15.7 mg Gd in each 79 ml or $C_m = 201$ kg Gd/m^3. The corresponding *in vivo* magnetization with the recommended dose of Magnevist is B_0-dependent as given by (6.10).

For SPIO agents, it is easily shown by means of the well-known Langevin relation, that superparamagnetic particles of 6 to 8 nm magnetic core diameter (typical values for Feridex nanoparticles [59]) will be magnetically saturated at all common clinical values of B_0 (*e.g.*, 1.5 T, 3 T and 7 T). Unlike Gd agents, whose concentration is usually expressed in molarity, SPIO agents are defined by the Fe mass in the solution. The typical clinical dosage of Feridex is 0.56 mg Fe per kg of patient weight. Given the molecular composition of magnetite (Fe_3O_4), this corresponds to 0.77 mg Fe_3O_4 per kg or 1×10^{-8} m^3 Fe_3O_4 per kg assuming magnetite has a density of 5150 kg·m^{-3}. After the agent is injected into the subject, it is diluted in the subject's bloodflow, yielding an effective value for ϕ *in vivo*. For *in vivo* administration to a normal, healthy adult with a total blood volume of 79 ml per kg bodyweight [103], this corresponds to a fraction solid volume of $\phi \approx 2.5 \times 10^{-6}$. The resultant *in vivo* magnetization is given by ϕM_d and has a value of 1.115 A·m^{-1} for the recommended dosage. It is noted that, unlike Gd agents, the effective *in vivo* magnetization of SPIO agents is almost entirely independent of B_0 for typical MRI systems ($B_0 \gtrsim 1$ T). A full discussion of the various concentration units for MRI contrast agents is outlined in Appendix B.

6.3 Experiments at 7T

An experimental setup was constructed consisting of an elevated cistern, connected gate-valves and long (1.8 m), straight circular pipes, as shown in Figure 6-2. An elevated cistern maintained an increased input pressure to the pipes which was reg-

ulated by means of a manual gate-valve. Two pipes of diameters $d_1 = 4.32$ mm and $d_2 = 6.35$ mm were used and the effect of varying the input pressure, P_1 was investigated by varying the open fraction of the valves. The other end of each pipe was open, $P_2 = 0$.

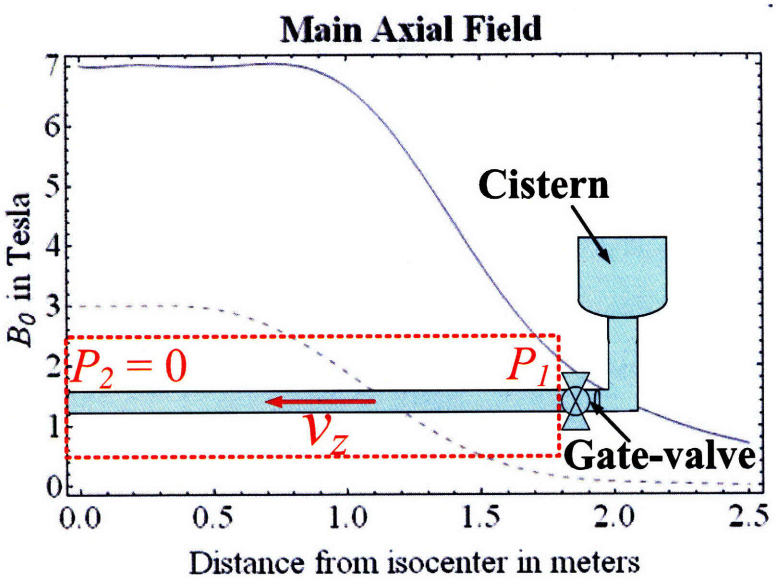

Figure 6-2: Schematic representation of the experimental setup used to investigate the effect on contrast agents of the fringing fields at 3 T and 7 T.

To correlate the input pressure, P_1 with the open valve fraction, f (f=1 $\Rightarrow$ open, f=0 $\Rightarrow$ closed), 4 liters of deionized water were added to the cistern and the valve opened by varying fractions, f ($0 < f < 1$). The total flow volume was collected at the other end of the pipe over a 3 minute time period and the average flow rate was calculated based on the pipe diameter in the absence of any magnetic field. Every attempt was made to minimize head losses in the cistern over this time by making the cistern diameter (28 cm) much larger than the pipe diameters ($d_1 = 4.32$ mm and $d_2 = 6.35$ mm). However, it was found that as the gate valve was opened ($f \rightarrow 1$), the

inlet pressure P_1 was increasingly a function of the changing pressure head and not of the valve open fraction, f. This is an undesirable situation since the flow velocity is no longer relatively constant over time but will vary the longer that the gate valve allows flow. The flow time was selected as 3 minutes to increase the net mass flow and, hence, minimize the variance due to experimental error.

A further complication is the presence of entrance effects at the gate valve. These tend to cause the flow to be more turbulent near the valve and result in a slowing of the average flow velocity compared to the case of fully developed laminar flow throughout the pipe's length. Instead, the flow velocity at entry from the gate-valve will be almost constant over the pipe's cross section. The velocity at the pipe wall, however, is zero so that a thin boundary layer is formed round the pipe walls. The thickness of this boundary layer increases downstream from the entry until it equals the radius of the pipe. The pipe length at which this occurs, L_e, has been found empirically to be given by (6.11) where r_n is the pipe radius [100].

$$L_e = 0.115\, r_n^2 \frac{v_{av}}{\eta} \tag{6.11}$$

It turns out that L_e can be a significant fraction of the overall pipe length for the work considered here. A corrected formulation for the relationship between v_{av} and the applied inlet pressure is now a discontinuous function [100] as given by the expressions of (6.12) in the absence of a magnetic field where $P(L_e)$ is the pressure at $z = L_e$ and ρ is the fluid density (assumed that of deionized water at room temperature, $\rho = 998\ \mathrm{kg{\cdot}m^{-3}}$). The entrance effects give rise to an additional pressure drop of $\frac{\rho v_{av}^2}{2}$ between $z = 0$ and $z = L_e$ in addition to the pressure drop for fully-developed laminar flow.

$$\frac{\partial p}{\partial z} = \frac{P_1 - P(L_e)}{-L_e} = \frac{8\eta v_{av}}{r_n^2} + \frac{\rho v_{av}^2}{2L_e} \quad \text{for} \quad 0 < z < L_e$$

$$\frac{\partial p}{\partial z} = \frac{P(L_e)}{L_e - L} = \frac{8\eta v_{av}}{r_n^2} \quad \text{for} \quad z > L_e \tag{6.12}$$

Deionized water was allowed to flow under a variety of inlet pressures by varying f. The relationship between P_1 and f was measured experimentally for various values of f by measuring v_{av} for deionized water flow in the absence of any magnetic field. This was achieved by measuring the mass flow rate over a 3 minute time period and estimating the corresponding average flow velocity from the pipe's cross-sectional diameter. The experiment was repeated three times and the resultant mean velocity measurements were used to estimate P_1 for each value of f. The results were fitted to the curve given by (6.12) and are shown in Figure 6-3. The plot also shows the linear relationship between P_1 and v_{av} as given by (6.5), where no account is taken for entrance effects and where it is assumed that $\frac{\partial p}{\partial z} = \frac{P_1}{L}$.

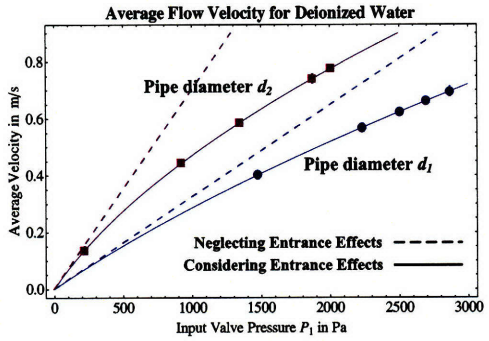

Figure 6-3: Measured flow velocity for deionized water in pipes of diameters $d_1 = 4.32$ mm and $d_2 = 6.35$ mm as a function of the inlet pressure, P_1, is fitted to the expressions of (6.12). The dashed lines show the linear relationship between P_1 and v_{av} when no account is taken for the entrance effects as given by (6.4). Velocities are plotted as positive values although the flow is in the negative z direction.

The experiment was then repeated using Magnevist and Feridex dilutions instead of deionized water. The recommended dosages (1x) of Magnevist and Feridex were added to 4 liters of deionized water, representative of the dilution which takes place when the contrast agents are administered *in vivo*. Two additional dosages of each agent, at twice and three times the recommended dose (2x and 3x) were also prepared in the same manner. Each of the six contrast agent solutions was subjected to the same experiment as the deionized water solution in the absence of any magnetic field. As might be expected, all the resultant measured flow velocities lay very close to the results of Figure 6-3.

To investigate the effect on flow velocity in the presence of a magnetic field, the experiment was moved into a 3 T Siemens Trio MRI scanner at the Athinoula A. Martinos Center for Biomedical Imaging (Massachusetts General Hospital). The profile of the main B_0 field as a function of distance from the scanner's isocenter at $z = 0$ is as shown in Figure 6-1 [104]. The pipe ends were positioned at the isocenter of the scanner, where pressure $P_2 = 0$. The other end of the pipe, where the gate valve is located, were positioned 1.8 m away, such that the pipe's principal axis ran parallel to the direction of the scanner's fringing field gradient. Again, the flow velocity was measured for various input pressures P_1, two different pipe diameters, d_1 and d_2, and each of the six dosages of contrast agent described above; 1x Magnevist, 2x Magnevist, 3x Magnevist, 1x Feridex, 2x Feridex and 3x Feridex. The entire procedure was repeated in a 7 T Siemens MRI scanner. In order to minimize the effects of head losses previously described, the pressure were limited at the gate valve where $f \approx 0.1$.

While initial results, such as the plots of Figure 6-4 (which shows the variation v_{av} as a function of magnetic field for various dosages of Magnevist agent) show significant

dependence on the B_0 field, it was subsequently found that these changes were due primarily to viscosity changes due to increasing temperature in the MRI.

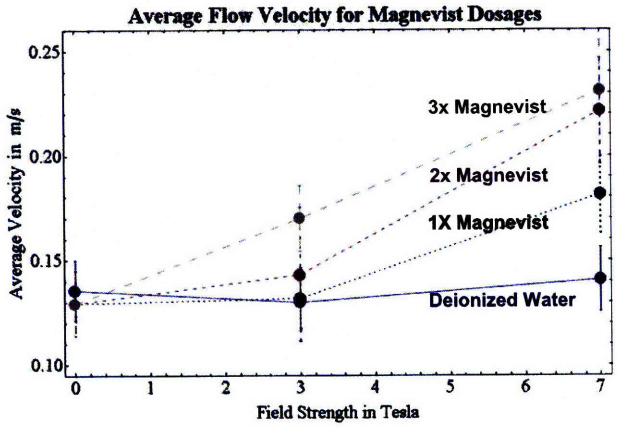

Figure 6-4: The average flow velocity recorded by experiment is shown for pipe with diameter d_2 when the inlet pressure, $P_1 \approx$ 250 Pa (as determined by (6.5) based on the measurements in the absence of B_0) for various dosages of Magnevist as a function of the magnetic field strength. Results for deionized water under the same field and pressure conditions are shown. It was subsequently found that these results could be accounted for by changes in the fluid viscosity due to changes in temperature rather than by the effet of the magnetic field.

Results shown in Figure 6-5 and Figure 6-6 show that the effects cease to be apparent when the effects of viscosity changes with temperature are considered. Changes in viscosity were accounted for by scaling the measured velocity by the appropriate temperature-dependent viscosity [105]. In general, results recorded outside of the MRI were recorded at 19°C where $\eta \approx 0.00105$ N·s·m^{-2} while the temperature in the 7 T scanner approached 28°C where $\eta \approx 0.00081$ N·s·m^{-2} [105]. Since viscosity is inversely proportional to fluid flow velocity in the pipe, this effect was found to be dominant over that of the magnetic field for the results of Figure 6-4.

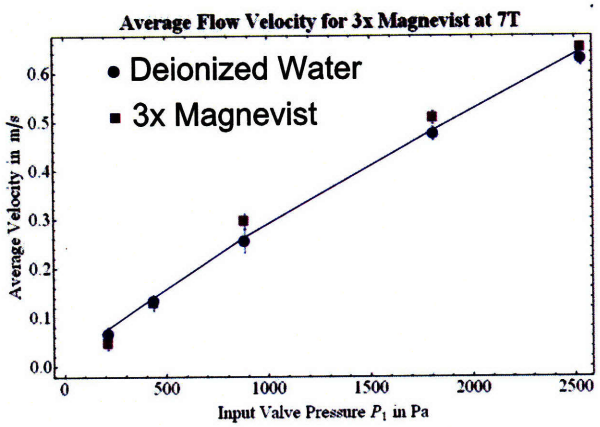

Figure 6-5: The average flow velocity from experiment at 7 T is shown for a pipe with diameter d_2 as a function of inlet pressure, P_1. Results for 3x Magnevist at 7T are shown by the purple squares. The solid line joins the blue datapoints, recorded for deionized water at 7T.

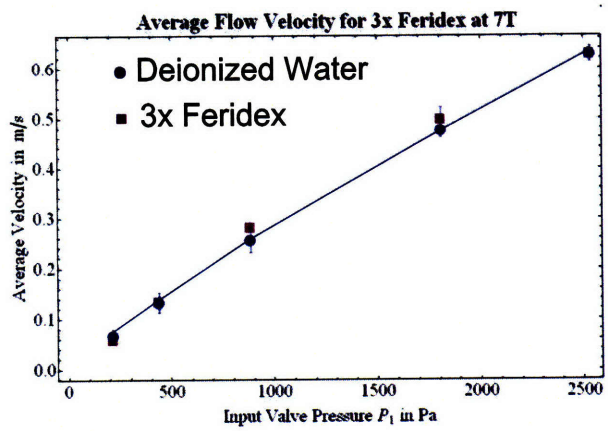

Figure 6-6: The average flow velocity from experiment at 7 T is shown for a pipe with diameter d_2 as a function of inlet pressure, P_1. Results for 3x Feridex at 7T are shown by the purple squares. The solid line joins the blue datapoints, recorded for deionized water at 7T.

6.4 Conclusions of Flow Experiments

As can be seen from Figure 6-3, the actual flow velocity varies significantly from that predicted for fully-developed flow when the pressure is increased. Therefore, the

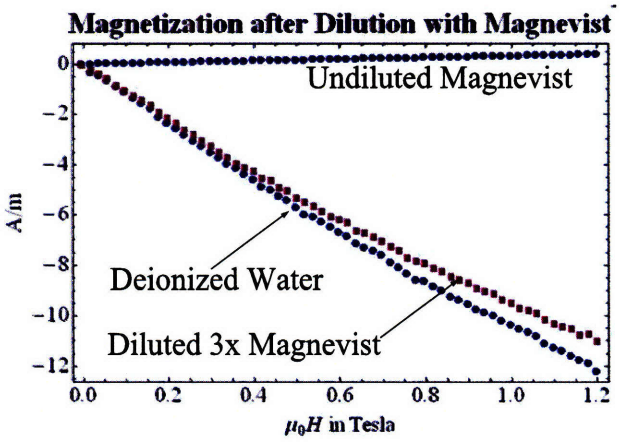

Figure 6-7: The measured M-H curves using vibrating sample magnetometry for deionized water, undiluted Magnevist and a 3x dosage of Magnevist diluted in deionized water.

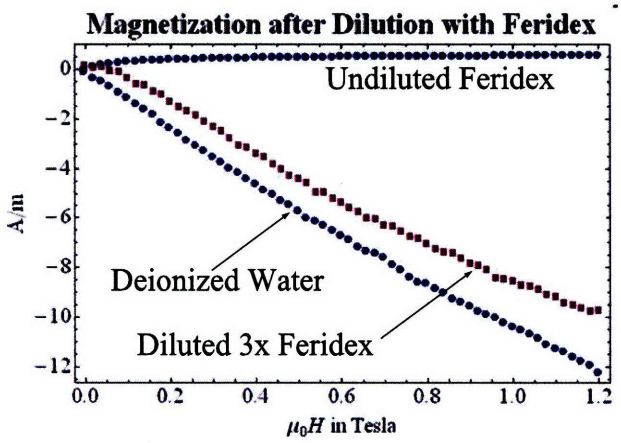

Figure 6-8: The measured M-H curves using VSM for deionized water, undiluted Feridex and a 3x dosage of Feridex diluted in deionized water.

additional experiments focussed on the low-pressure flow domain so that the magnetic forces would not be dominated by the pressure differential in the system. However, as shown in Figures 6-5 and 6-6, the results for the contrast agents and those for deionized water tend to be very similar even at 3x the recommended dosage and in

a 7T MRI field. Accordingly, it was concluded that contrast agents administered *in vivo* are unlikely to have any appreciable impact on the blood flow velocity due to the magnetic particles in the suspension being pulled into the region of strongest field. To confirm this conclusion, the magnetization of 3x dosages of both Magnevist and Feridex contrast agents were measured in the VSM for field strengths up to 1.2 T. The results are shown in Figures 6-7 and 6-8. Also included in these plots are the measured magnetization for deionized water and for the undiluted agent, as indicated on the plot. Since these measurements are beyond the threshold for which the instrument can be relied upon to provide accurate measurements, a quantitative interpretation is inexact. However, it is qualitatively apparent that the magnetization associated with both the Gd-based Magnevist and the SPIO Feridex is due to the combined effects of the diamagnetic deionized water and the (super)paramagnetic contrast agent. In both cases, the net result is that the diluted agent has a net diamagnetic magnetization, albeit less than that of deionized water. This evidence complimented the experimental results of Figures 6-5 and 6-6, clarifying why the contrast agents exert little or no force on the fluid flow for the dosages examined in this work. It remains to be seen if this result is true for higher dosages or for deoxygenated blood flow where deoxygenated blood has a diamagnetic susceptibility of -7.9×10^{6} [93] compared to -9×10^{6} for pure water.

Chapter 7

Heating with Contrast Agents in MRI

The Food and Drug Administration (FDA), who regulate MRI in the US, outlines four areas of safety concern in MRI [111]:

- Force and torque on magnetic materials due to the static magnetic field
- Heating caused by the RF magnetic fields
- Subject nerve stimulation due to the gradient magnetic fields used for spatial encoding
- Risks associated with implanted medical devices in conjunction with all of the above [112]

The proposals of Chapters 2 and 3 of this thesis propose the introduction of an additional RF excitation source in the MRI system. The goal of this additional source is to modify, as a function of excitation frequency, the local magnetization in the presence of magnetic nanoparticles. However, not considered is the considerable

heating associated with magnetic fluids in this field, in particular the non-ohmic heating that results when magnetic fluids interact with a rotating field. This is the primary concern of this chapter.

7.1 RF Heating due to Eddy Currents in MRI

The FDA stipulates that the "normal mode limit" (*i.e.*, suitable for all patients) for whole-body heating due to RF in MRI is 0.5°C or 2 W/kg of bodyweight. This increases to 1°C or 4 W/kg under the "first level controlled mode" (*i.e.*, under medical supervision). For human head scans in the normal mode limit, the temperature is not to exceed 38° C or 3.2 W/kg averaged over the head mass. However, in MRI, this heating effect is usually entirely due to the effect of eddy currents circulating in the subject. The effect is most pronounced where the electrical conductivity, σ, is significant, such as in the eyes, and where charge tends to accumulate (*e.g.*, the tip of the nose). However, since the conductivity of both ferrofluids and MRI contrast agents is so small ($\sigma \approx 28 \times 10^{-6}$ [73]) that the contrast agent has little or no effect on SAR due to eddy currents as discussed in various publications [76–79].

7.2 RF Heating due to Rotational Relaxation of Magnetic Nanoparticles in MRI

In the presence of sinusoidal or rotating magnetic fields, magnetic nanoparticles will act to realign their magnetization with the applied rotating field. The realignment is characterized by the time constant τ, as given by Eq. (1.1) and shown in Fig. 1-2. When the sinusoidal or rotating field frequency Ω is such that $\Omega\tau$ approaches unity,

the magnetization associated with the particles and the applied magnetic field are no longer collinear. When this occurs, there is power dissipation which results in the heating of the magnetic particles [42, 113]. This phenomenon has given rise to an entire field of research dedicated to the treatment of cancer patients, based on the localized heating effects of magnetic nanoparticles *in vivo* [80,81,83]. Treatment falls under one of two categories, hyperthermia and thermoablation.

7.2.1 Hyperthermia and Thermoablation

In hyperthermia, the target area is subjected to a local temperature in the range of 42°C to 45°C for periods of up to a few hours [80]. The end result is usually not sufficient to eradicate all the cancerous cells and is coupled with other techniques such as irradiation or chemotherapy [83]. Thermoablation aims at creating *in vivo* temperatures in excess of 50° in the tumor region and exposure time is limited to just minutes. Although this approach would appear preferred, there are concerns regarding the physiological effects of such a rapid, localized heating effect [82]. To date, particles that have been used are either injected in situ or are designed to bind selectively to cancerous cells. The majority of investigations use superparamagnetic magnetite or maghemite (γ-Fe_2O_3) in water based suspensions since these are well metabolized. Creating *in vivo* concentration to allow for sufficient heating is a major challenge due to heat conduction away from the target area as well as blood perfusion around the tumor [80]. A second significant challenge is the undesired heating associated with eddy currents in surrounding healthy tissue [85]. Brezovich [85] found that subjects had a sensation of warmth but were able to withstand the treatment for more than an hour when the product of the field amplitude H_e and the frequency $f = \Omega/(2\pi)$ did not exceed 4.85 $\times 10^8$ (A/m)/s. Superparamagnetic particles of mag-

netite and maghemite have been the preferred nanoparticle to date [81] but recent developments such as FeCo particles [70] would offer significant advantage due to the increased magnetic moment per particle if concerns regarding biocomparability can be overcome.

7.2.2 Heating in Superparamagnetic Fluids

Rosensweig [113] has examined the effect of RF fields on superparamagnetic fluid suspensions. His work develops dissipation relationships based on the rotational relaxation of single-domain magnetic nanoparticles dispersed in a solvent due to sinusoidal magnetic fields. Eddy current heating is assumed to be negligible due to the small size of the particles ($<$ 15 nm core diameter). Rosensweig showed volumetric power dissipation was closely related to the solution of Shlimois' Relaxation Equation [48]. This present work follows Rosensweig's approach and introduces two significant developments: (i) the analysis is revised for the presence of rotating as well as sinusoidal magnetic fields and (ii) the analysis is examined in the MRI environment where, it is expected that the heating effect will be limited due to the large B_0 field.

7.2.3 Theory

This analysis is based on the channel geometry shown in Figure 2-1, where a planar ferrofluid layer between rigid walls at $y = 0, d$, is magnetically stressed by a uniform DC z-directed magnetic field H_0, an alternating x-directed magnetic field of complex amplitude $\hat{h}_x$ and an alternating y-directed magnetic flux density of complex amplitude $\hat{b}_y$. The x and y components vary sinusoidally at frequency Ω. The walls are of infinite extent along the z axis and there is no ferrofluid outside the channel. It has been shown in Chapter 2 that in the absence of any applied pressure differential or

imposed linear flow, the solutions for the x and y directed magnetization components, associated with the applied transverse rotating field are given by (2.17) and (2.18), repeated for convenience in (7.1) and (7.2).

$$\hat{m}_x = \frac{M_0}{H_0} \frac{(\jmath\Omega\tau + 1 + M_0/H_0)\hat{h}_x - (\omega_z\tau)\hat{b}_y/\mu_0}{(\jmath\Omega\tau + 1)(\jmath\Omega\tau + 1 + M_0/H_0) + (\omega_z\tau)^2} \tag{7.1}$$

$$\hat{m}_y = \frac{M_0}{H_0} \frac{(\omega_z\tau)\hat{h}_x + (\jmath\Omega\tau + 1)\hat{b}_y/\mu_0}{(\jmath\Omega\tau + 1)(\jmath\Omega\tau + 1 + M_0/H_0) + (\omega_z\tau)^2} \tag{7.2}$$

The associated spin-velocity is z-directed and given by (2.41), repeated in (7.3)

$$\omega_z = \frac{1}{8\zeta} \Re e(\hat{m}_x \hat{b}_y^* - \mu_0(\hat{h}_x + \hat{m}_x)\hat{m}_y^*) \tag{7.3}$$

From the first law of thermodynamics, the differential internal heat density, dU for a closed system of constant density is given by (7.4) where δQ is the differential energy input and δW is the differential work done by the system.

$$dU = \delta Q - \delta W \tag{7.4}$$

For an adiabatic process, it can be assumed that δQ is zero so that all generated heat remains within the system. This ignores, for example, blood perfusion. The internal energy is then given by $-\delta W$, which, for a magnetic fluid with negligible conductivity is given by (7.5) where $\mathbf{H}$ and $\mathbf{B}$ are the magnetic field intensity and magnetic flux density respectively.

$$\delta W = -\mathbf{H} \cdot d\mathbf{B} \tag{7.5}$$

Simplification is possible using the relationship between $\mathbf{B}$, $\mathbf{H}$ and $\mathbf{M}$.

$$\mathbf{B} = \mu_0(\mathbf{H} + \mathbf{M})$$

$$\Rightarrow \quad \delta W \; = \; -\mu_0(\mathbf{H} \cdot d\mathbf{H} + \mathbf{H} \cdot d\mathbf{M}) \tag{7.6}$$

Rosensweig has shown [113] that integration by parts then yields the expression of (7.7) for the cyclic increase in work done, ΔW, which is the negative of the cyclic increase in internal energy per unit volume, ΔU.

$$\Rightarrow \quad \Delta U = -\Delta W = -\oint \delta W \; = \; \mu_0 \oint (\mathbf{M} \cdot d\mathbf{H}) \tag{7.7}$$

As noted by Rosensweig [113], ΔU is positive in a ferrofluid solution where $\mathbf{M}$ lags behind $\mathbf{H}$ as occurs when the rotating field is at sufficiently high frequency. The solution is expressed in terms of one complete time cycle, of period $T = 2\pi/\Omega$, in (7.8). It is noted that the partial time derivative of (7.8) is correct for a stationary medium. For moving media, the convective derivative should be employed.

$$\Delta U = -\mu_0 \int_0^T (\mathbf{M} \cdot \frac{\partial \mathbf{H}}{\partial t}) dt \tag{7.8}$$

The expression of (7.8) is evaluated where $\mathbf{M}$ is the vector whose components are the complex amplitudes, $\hat{m}_x$ and $\hat{m}_y$, given by (7.1) and (7.2). The time derivative of the $\mathbf{H}$ field is first evaluated in (7.10) where $\mathbf{H}$ is given by (7.9).

$$\boldsymbol{H} = \Re e\Big(e^{\jmath\Omega t}(\hat{h}_x \boldsymbol{i}_x + \hat{h}_y \boldsymbol{i}_y)\Big) \tag{7.9}$$

$$\frac{\partial \mathbf{H}}{\partial t} = \Re e\Big(\jmath\Omega e^{\jmath\Omega t}(\hat{h}_x \boldsymbol{i}_x + \hat{h}_y \boldsymbol{i}_y)\Big) \tag{7.10}$$

$$\frac{\partial \mathbf{H}}{\partial t} = \Re e\Big(\jmath\Omega e^{\jmath\Omega t}(\hat{h}_x \boldsymbol{i}_x + (\hat{b}_y/\mu_0 - \hat{m}_y)\boldsymbol{i}_y)\Big) \tag{7.11}$$

Substituting the expression of (7.11) into (7.8) eventually yields (7.16).

$$\Delta U = -\mu_0 \int_0^T (\mathbf{M} \cdot (\Re e(\jmath\Omega e^{\jmath\Omega t}(\hat{h}_x \boldsymbol{i}_x + (\hat{b}_y/\mu_0 - \hat{m}_y)\boldsymbol{i}_y))dt \tag{7.12}$$

$$\Delta U = -\mu_0 \Re e\Big(\int_0^T (\hat{m}_x \boldsymbol{i}_x + \hat{m}_y \boldsymbol{i}_y) e^{\jmath\Omega t} \cdot \jmath\Omega e^{\jmath\Omega t}(\hat{h}_x \boldsymbol{i}_x + (\hat{b}_y/\mu_0 - \hat{m}_y)\boldsymbol{i}_y)dt\Big) \tag{7.13}$$

$$\Delta U = -\mu_0 \Re e\Big(\int_0^T \Big(\frac{1}{2}\hat{m}_x(\jmath\Omega\hat{h}_x)^* + \frac{1}{2}\hat{m}_y(\jmath\Omega(\hat{b}_y/\mu_0 - \hat{m}_y))^*\Big)dt\Big) \tag{7.14}$$

$$\Delta U = -\mu_0 \Re e\Big(\int_0^T \Big(\frac{1}{2}\hat{m}_x(-\jmath\Omega\hat{h}_x^*) + \frac{1}{2}\hat{m}_y(-\jmath\Omega(\hat{b}_y^*/\mu_0 - \hat{m}_y^*))\Big)dt\Big) \tag{7.15}$$

The last term of (7.15) has $\hat{m}_y$ multiplied by its complex conjugate (purely real) which is then multiplied by $jmath$ so this term is purely imaginary and thus has no real part. It is eliminated from the expression.

$$\Delta U = -\mu_0 \Re e\Big(-\frac{\jmath\Omega}{2}\hat{m}_x\hat{h}_x^* - \frac{-\jmath\Omega}{2}\hat{m}_y(\hat{b}_y^*/\mu_0)\Big)T \tag{7.16}$$

The period T, is given by $2\pi/\Omega$ so further simplification is possible.

$$\Delta U = \mu_0 \Re e\Big(\jmath\pi(\hat{m}_x\hat{h}_x^* + \hat{m}_y(\hat{b}_y^*/\mu_0))\Big) \tag{7.17}$$

Substituting for $\hat{h}_x = H_e$ and $\hat{b}_y = \jmath B_e$ where H_e and B_e are real-valued quantities leads to (7.18), generating a rotating field in the transverse xy plane. For the analysis which follows B_e and H_e are related by $B_e = \mu_0 H_e$ and $\mu_0 = 4\pi \times 10^{-7}$, the magnetic permeability of free space.

$$\Delta U = \mu_0 \Re e\Big(\jmath\pi(\hat{m}_x H_e + \hat{m}_y(-\jmath B_e/\mu_0))\Big) \tag{7.18}$$

The volumetric power dissipation, P_v, in W/m^3 is then given by $f = \Omega/(2\pi)$ times the expression in (7.18), as in (7.19). This expression equals equation (6) of Rosensweig's work [113] when B_e is zero and the spin velocity in (7.1) and (7.2) is ignored.

$$P_v = \mu_0 \Re e\Big(\frac{\jmath\Omega}{2}(\hat{m}_x H_e + \hat{m}_y(-\jmath B_e/\mu_0))\Big) \tag{7.19}$$

While Rosensweig related this expression to the rate of temperature rise, the specific absorption rate (SAR) is the conventional measure of heating effects in human tissue. SAR is given by the volumetric power dissipation divided by the mass density, ρ_m, in kg/m^3, as in (7.20). As noted by Andra et al. [84], the value of ρ_m should be given by the mass of magnetic nanoparticles per unit mass of tissue rather than the value of the tissue mass density.

$$SAR = P_v/\rho = \mu_0 \Re e\Big(\frac{\jmath\Omega}{2\rho_m}(\hat{m}_x H_e + \hat{m}_y(-\jmath B_e/\mu_0))\Big) \tag{7.20}$$

The relation between SAR and temperature rise *in vivo* has been evaluated by Andra [84] for the particular case of small, spherical tumors in relatively homogenous tissue with low blood perfusion (*e.g.*, muscle tissue or fat). The situation is approximately realized in breast carcinomas. While the full expressions [84] relate SAR

to spatial and temporal variations, the steady-state temperature rise above ambient temperature in a spherical tumor of radius, R, is given by (7.21) where λ is the heat conductivity of tissue with an approximate value of 0.64 $\mathrm{W{\cdot}K^{-1}{\cdot}m^{-1}}$.

$$\Delta T = \frac{SAR \cdot R^2}{3\rho_m \lambda} = \frac{P_v R^2}{3\lambda} \tag{7.21}$$

The variation of the SAR and steady-state temperature rise is investigated for a number of cases of interest. The work represents two significant developments over that of Rosensweig [113]. Firstly, the case of rotating rather than purely sinusoidal magnetic field excitation is investigated. Secondly, the effect of excitation, with both sinusoidal and rotating fields, is investigated in the presence of a low-field MRI system (B_0 varying from 0.1 T to 0.35 T) as has been proposed in Chapter 2 of this work. The rotating and sinusoidal fields are applied orthogonal to the DC B_0 field. In each case, the effect of variation in (i) particle radius, r, (ii) field excitation frequency, Ω, (iii) field amplitude, $H_e = B_e/\mu_0$, (iv) B_0 field strength and (v) solid magnetic volume fraction ϕ is investigated. In estimating ΔT, the magnetic mass density is given by $\rho_m = \rho_{Fe_3O_4}\phi$ where the density of magnetite, $\rho_{Fe_3O_4}$, has a value of 5180 $\mathrm{kg/m^3}$ [113]. It is noted that while the results of Chapters 2 and 3 examined the variation of various parameters as the dimensionless product $\Omega\tau$ varied, this chapter explicitly plots the results versus particle radius since, as will be apparent, heating due to nanoparticle rotation is most pronounced at $\Omega\tau = 1$ only when the particles are close to magnetic saturation. However, since it is very difficult to manufacture a ferrofluid/SPIO suspension with a single characteristic radius (and hence characteristic time constant), showing results versus particle radius seems a more realistic scenario.

7.2.4 Sinusoidal Field Excitation in the absence of B_0

This section examines heating in the absence of MRI with a sinusoidal magnetic field excitation. Following the analysis of Rosensweig, spin-velocity is ignored (*i.e.*, $\omega_z = 0$) in the case of a sinusoidal driving magnetic field. This leads to a simplification in the expressions for $\hat{m}_x$ and $\hat{m}_y$ as given by (7.22) and (7.23) where the sinusoidal excitation has amplitude H_e and is applied along the x direction. The orthogonal field component, with amplitude B_e, is set to zero.

$$\hat{m}_x = \chi \frac{\hat{h}_x}{(\jmath\Omega\tau + 1)} \tag{7.22}$$

$$\hat{m}_y = 0 \tag{7.23}$$

The low-frequency limit of susceptibility, given by M_0/H_0 in the presence of the B_0 field characteristic of MRI, reduces to a simple susceptibility when B_0 is zero. This susceptibility, denoted χ, is given by (7.25) [42]. This expression for χ is the chord susceptibility employed by Rosensweig and written in terms of the full Langevin equation (see (1.5)) in the absence of any B_0 field. Approaching zero field, the chord susceptibility is zero as α, given by (7.24) also approaches zero.

$$\alpha = \frac{M_d V_p \mu_0 |\mathbf{H_0}|}{kT} \tag{7.24}$$

$$\chi = \frac{\mu_0 \phi M_d^2 V_p}{kT} \frac{3}{\alpha} \Big(\coth(\alpha) - 1/\alpha \Big) \tag{7.25}$$

The chord susceptibility is plotted in Figure 7-1 as a function of particle radius for various values of field strength, denoted H_e, in units of A/m. Clearly, as particle

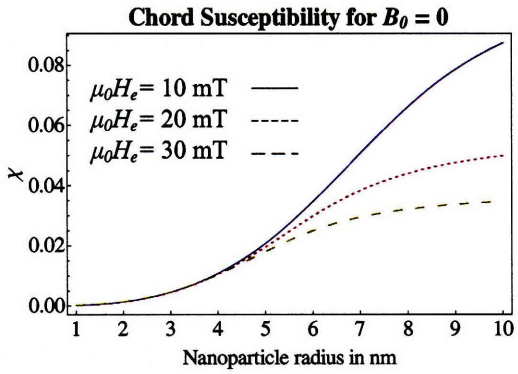

Figure 7-1: The effect of particle radius on the chord susceptibility, given by (7.25), is examined for three magnetic fields of interest: $\mu_0 H_e = 10$ mT, 20 mT and 30 mT.

radius increases, the slope of the Langevin relation, and hence the chord susceptibility, increases. This is also apparent from Figure 1-4 in Chapter 1, which shows the Langevin relation, plotted in the presence of increasing B_0. For the chord susceptibility, the dependence is not on B_0 (which is zero for now) but on the amplitude of the rotating field, H_e. As H_e increases, the slope of the Langevin curve, and hence chord susceptibility, decreases as the fluid slowly approaches magnetic saturation due to H_e. This is apparent in Figure 7-1 where, for any particular particle radius, an increasing H_e field results in increased susceptibility. The unitless Langevin parameter is $\alpha = \frac{\mu_0 V_p M_d H_e}{kT}$ in this case and all other quantities are as noted in relation to (1.5) of Chapter 1.

The results for SAR and ΔT, the change in temperature, are shown in Figure 7-2. The tissue was assumed to have the same mass density as water at room temperature (998 kg/m^3) and, unlike in Rosensweig's approach, the ferrofluid/SPIO solution was assumed water-based. The surfactant thickness was taken as 2nm throughout and the time constant's dependence on r is as plotted in Figure 1-2. All remaining parameters (field amplitude H_e, field frequency, Ω and particle concentration ϕ) were varied as

noted in the results of Figure 7-2. In the plots of ΔT, the tumor radius, R, is assumed to be 1 cm.

7.2.5 Rotating Field Excitation in the absence of B_0

This section examines heating due to a rotating magnetic field in the absence of the MRI's B_0 field. For a rotating field, the expressions for the complex magnetization amplitudes are now given, once again, by (7.1) and (7.2) where M_0/H_0 is again replaced by χ, as given by (7.25). The y-directed component of field excitation, with complex amplitude given by jB_e is now non-zero. All other parameters are unchanged from the prior case. The resulting variation in SAR and ΔT is shown in Figure 7-4, for varying parameters of interest. It is noted again that the x and y components of field excitation are related by $\mu_0 H_e = B_e$. As before, for the plots of ΔT, the tumor radius is assumed to be 1 cm.

7.2.6 Sinusoidal Field Excitation in the presence of B_0

This section examines the effect of heating due to a sinusoidal magnetic field in the presence of the B_0 field of MRI. In the MRI, the large, z-directed, B_0 field is applied in addition to the transverse x-directed sinusoidal magnetic field. The primary effect of B_0 on the SPIO magnetization is that the saturation of the nanoparticles is determined primarily by B_0 when $B_0 \gg \mu_0 H_e$. Since physically achievable AC rotating fields are unlikely to exceed 10 mT [80] due to power requirements, the assumption that saturation is determined by B_0 is reasonable for B_0 in the range of 0.1 T to 0.35 T. The expressions for the complex magnetization amplitudes $\hat{m}_x$ and $\hat{m}_y$ are identical to that of (7.22) and (7.23) where $\omega_z = 0$ in the absence of a y component of magnetic field. Also, χ is replaced by M_0/H_0 and M_0 is given by (A.20)

while H_0 is approximately equal to B_0/μ_0 for the B_0 fields considered in this work. The ratio of M_0/H_0 is plotted in Figure 7-3 versus the particle radius for three values of B_0 which are of interest. Clearly, as B_0 increases, the ratio of M_0/H_0 decreases in value.

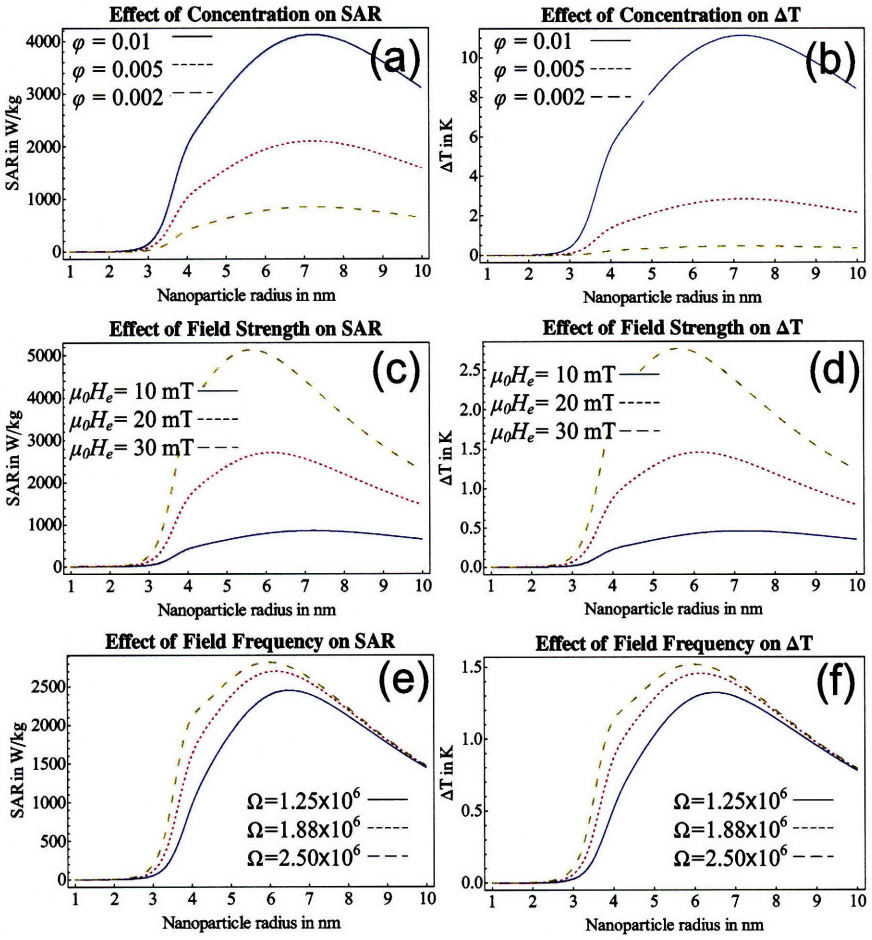

Figure 7-2: The effect on SAR and ΔT are shown for changing particle radius with varying (a) and (b) magnetic solid volume fraction, ϕ while $\Omega = 1.88 \times 10^6$ rad/s and $\mu_0 H_e = 10$ mT, (c) and (d) magnetic field amplitude while $\Omega = 1.88 \times 10^6$ rad/s and $\phi = 0.002$, and, (e) and (f), magnetic field frequency while $\mu_0 H_e = 20$ mT and $\phi = 0.002$. The excitation takes the form of a sinusoidally varying waveform and there is no DC MRI field, B_0.

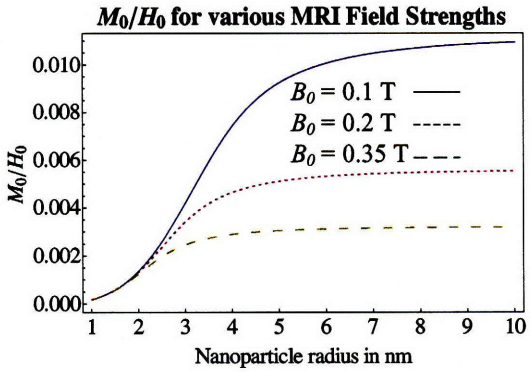

Figure 7-3: The effect of changing particle radius on the ratio of M_0 to H_0 is shown for increasing values of B_0, 0.1 T, 0.2 T and 0.35 T. The ratio saturates at large values of r as might be expected since the onset of magnetic saturation is earlier with increasing particle size. For this result, $\phi = 0.002$.

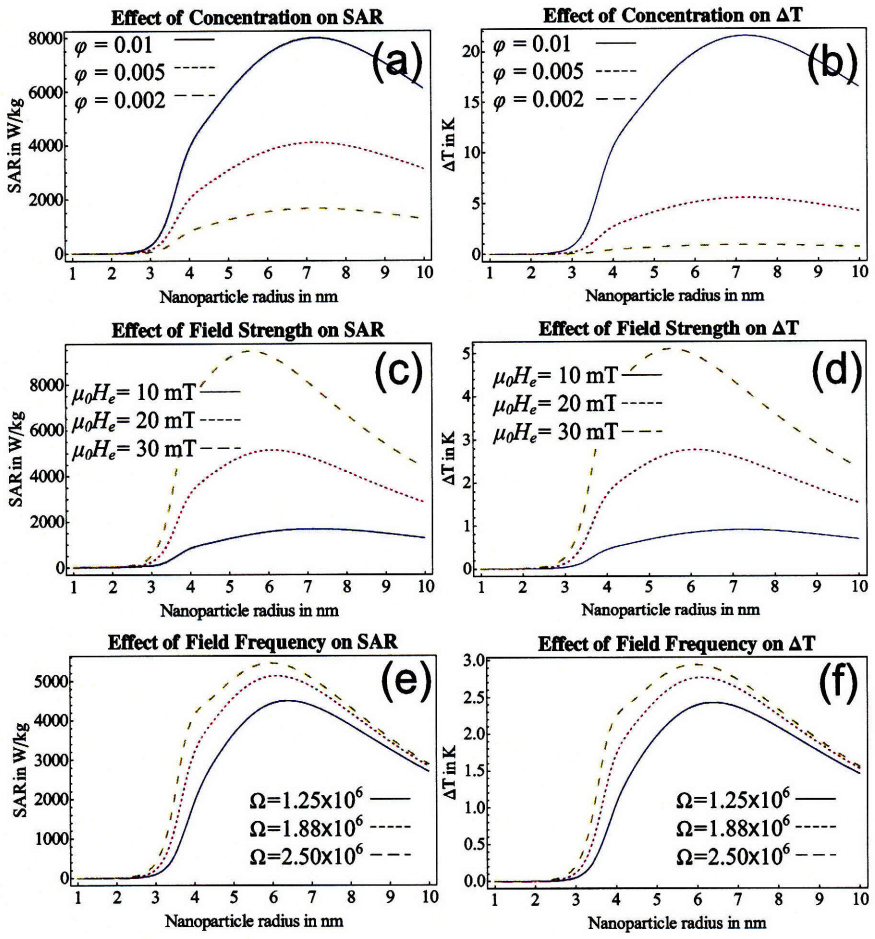

Figure 7-4: The effect on SAR and ΔT are shown for changing particle radius with varying (a) and (b) magnetic solid volume fraction, ϕ while $\Omega = 1.88 \times 10^6$ rad/s and $B_e = 10$ mT, (c) and (d) magnetic field amplitude while $\Omega = 1.88 \times 10^6$ rad/s and $\phi = 0.002$, and, (e) and (f), magnetic field frequency while $B_e = 20$ mT and $\phi = 0.002$. In this case, the excitation takes the form of a rotating waveform and there is no DC MRI field, B_0.

The effect on SAR and steady state temperature rise, ΔT, in a tumor of 1 cm radius is plotted for changing values of particle concentration ϕ, field amplitude, H_e, field frequency, Ω, and main field strength, B_0 and the results are shown in in Figure 7-5 for a sinusoidal field transverse to B_0. It is noted that the sinusoidal field could also be added in the z direction such that the χ is then replaced by the derivative of the Langevin function evaluated at B_0 (i.e, $\frac{\partial M_0}{\partial H_0}$). However, as shown in Figure A-1, the value of $\frac{\partial M_0}{\partial H_0}$ is less than M_0/H_0 for all values of B_0 except in the very low field limit ($B_0 \rightarrow 0$ T), where the two are approximately equal.

7.2.7 Rotating Field Excitation in the presence of B_0

The sinusoidal field is now replaced by a rotating field of amplitude H_e and frequency Ω while the B_0 field is maintained and the results with varying parameters of interest are shown in Figure 7-6. Again, in calculating ΔT, the tumor radius is assumed to be 1 cm. The expressions for the transverse complex magnetization amplitudes are identically (7.1) and (7.2) where it is assumed that saturation is determined primarily by the B_0 field and not the transverse rotating field amplitude.

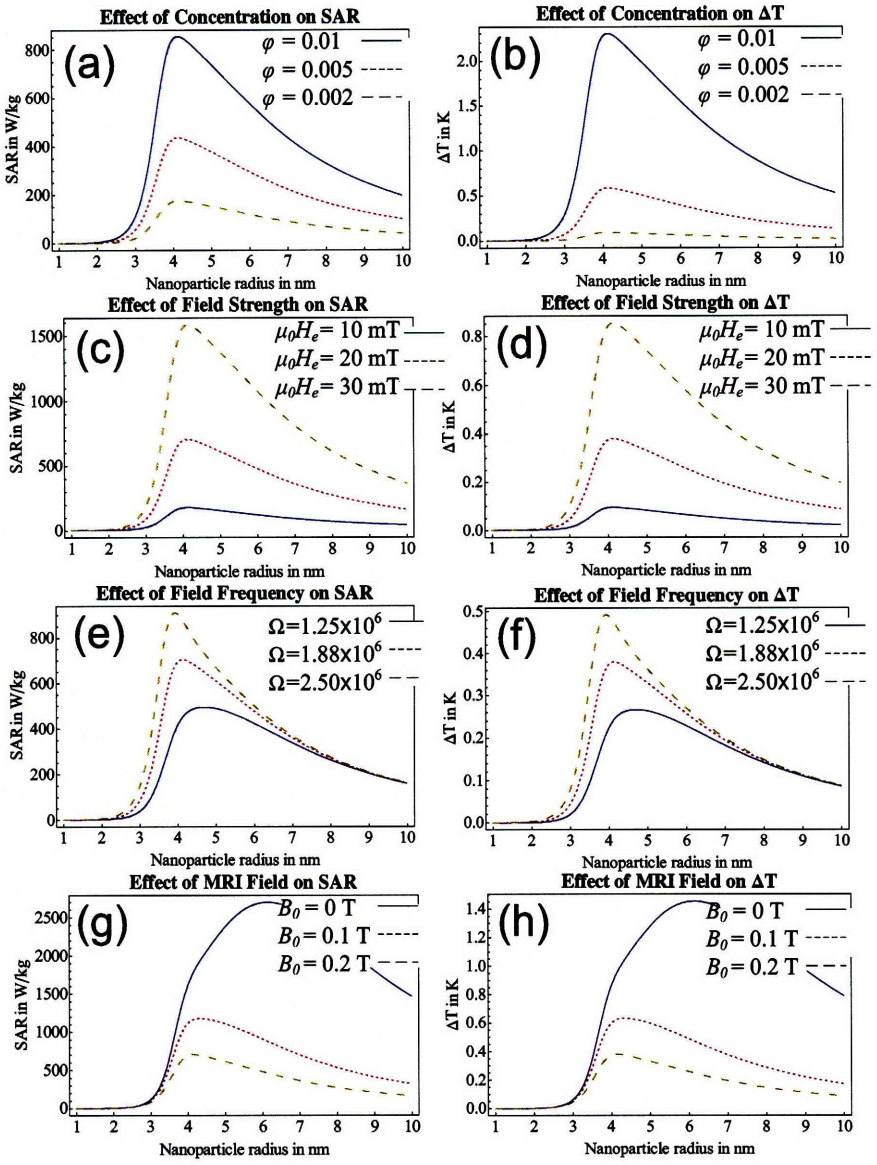

Figure 7-5: The effect on SAR and ΔT are shown for changing particle radius with varying (a) and (b) magnetic solid volume fraction, ϕ while $\Omega = 1.88 \times 10^6$ rad/s, $B_e = 10$ mT and $B_0 = 0.2$ T; (c) and (d) magnetic field amplitude while $\Omega = 1.88 \times 10^6$ rad/s, $\phi = 0.002$ and and $B_0 = 0.2$ T; (e) and (f), magnetic field frequency while $B_e = 20$ mT, $\phi = 0.002$ and $B_0 = 0.2$ T and; (g) and (h), main field strength with $\Omega = 1.88 \times 10^6$ rad/s, $B_e = 20$ mT and $\phi = 0.002$. The excitation takes the form of a sinusoidal, x-directed waveform and the B_0 field is assumed orthogonal (z-directed).

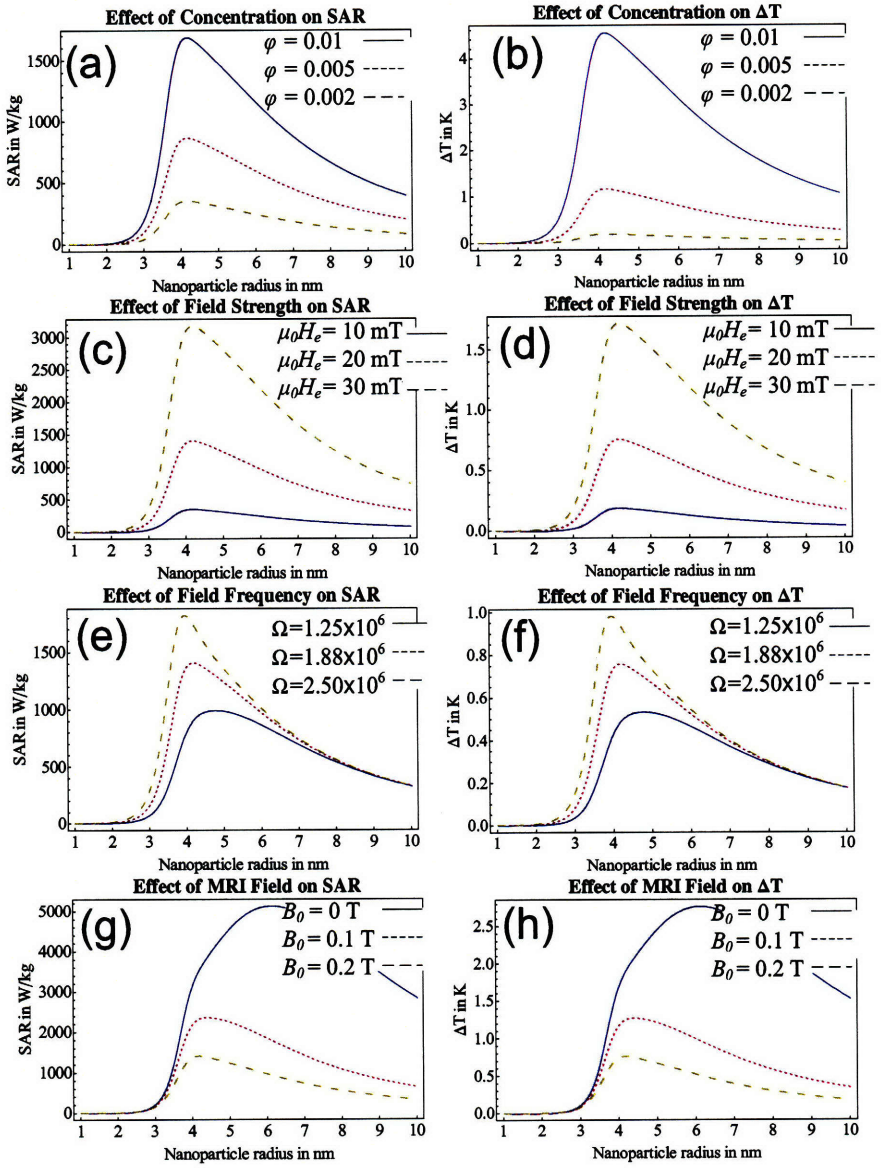

Figure 7-6: The effect on SAR and ΔT are shown for changing particle radius with varying (a) and (b) magnetic solid volume fraction, ϕ while $\Omega = 1.88 \times 10^6$ rad/s, $B_e = 10$ mT and $B_0 = 0.2$ T; (c) and (d) magnetic field amplitude while $\Omega = 1.88 \times 10^6$ rad/s, $\phi = 0.002$ and and $B_0 = 0.2$ T; (e) and (f), magnetic field frequency while $B_e = 20$ mT, $\phi = 0.002$ and $B_0 = 0.2$ T and; (g) and (h), main field strength while $\Omega = 1.88 \times 10^6$ rad/s, $B_e = 20$ mT and $\phi = 0.002$. The excitation takes the form of a rotating, transverse xy field and the B_0 field is assumed orthogonal (z-directed).

7.2.8 Discussion

Sinusoidal Field Excitation in the absence of B_0

The results of Figure 7-2 compliment those of Rosensweig although the solution is now a water-based rather than an oil-based solution [113]. As is evident from Figure 7-2(a) and (b), the SAR and temperature rise are a maximum at a particle radius of approximately 7nm for a rotating field frequency of 300 kHz. While one might suspect that this is where the product of $\Omega\tau$ approaches unity, this is only true in the case where the chord susceptibility, χ, is non-variant with particle radius, as is the case when the fluid approaches saturation. Otherwise, the dependence of SAR, and hence the change in temperature, is a non-linear function of the particle radius where the chord susceptibility tends to shift the peak value of SAR to the right of where $\Omega\tau = 1$. For an excitation frequency of 1.9×10^6 rad/s ($\approx$300 kHz), Figure 1-2 shows that the particle radius is approximately 4 nm when $\Omega\tau = 1$. Clearly, this does not correspond to the peaks of Figure 7-2, although as the sinusoidal field amplitude increases in Figure 7-2(c) and (d), the peak is seen to shift towards $\Omega\tau = 1$ as one would expect due to the increasingly saturated fluid.

The dependence of SAR on particle concentration, is linear, as shown in Figure 7-2(a) and (b), This is expected since the magnetization, on which SAR is linearly dependent, increases linearly with chord susceptibility and hence, on particle concentration, ϕ. However, the temperature change, ΔT, increases with the square of the particle concentration as is obvious from (7.21), which introduces a second ϕ factor in addition to that due to the chord susceptibility. These dependencies are clear in Figure 7-2(a) and (b).

SAR depends in a non-linear fashion on the sinusoidal field amplitude H_e, as shown in Figure 7-2(c) and (d). This relation is expected due to the non-linear

dependence of chord susceptibility on the field amplitude. However, with increasing H_e, the chord susceptibility becomes increasingly non-variant with particle radius, as has already been noted for the case of a fluid approaching saturation. As the fluid approaches saturation, the SAR shows a square dependence on H_e and this relation is visible in later plots with the addition of the B_0 field, where the fluid is increasingly saturated. Saturation is not achieved in the case of a sinusoidal field excitation with $\mu_0 H_e < 30\text{mT}$ as is the case here.

The variation of the applied field frequency, Ω, has two effects on SAR and ΔT. Firstly, the peak value tends to shift to lower values of particle radius as Ω increases. This is because, as Ω increases the maximum of the expression in (7.22) tends to shift to the left, corresponding to the peak of $\Omega\tau$ shifting with changing Ω. As already noted, the peaks are not centered on $\Omega\tau = 1$ while the chord susceptibility remains a function of r. The second effect is that, for any one value of r, both SAR and ΔT increase non-linearly with Ω. This is due to two competing terms: (i) from (7.19) and (7.20), SAR will increase linearly with Ω while (ii) SAR decreases with Ω due to the $\Omega\tau$ term in the denominator of (7.22). The first of the two effects dominates, resulting in increasing SAR and ΔT with increasing Ω. For $\Omega\tau \gg 1$ or $\Omega\tau \ll 1$, the second effect disappears and SAR (and ΔT) increase linearly with Ω. This is the reason why workers [80,81,83] developing hyperthermia systems seek to maximize Ω within physiological limits.

Rotating Field Excitation in the absence of B_0

With the addition of a second orthogonal (y-directed) component, which is a quarter cycle temporally displaced from the x-directed field (*i.e.*, 90° phase difference), a rotating field is created. This action doubles the magnitude squared of the applied

field, thereby doubling the power dissipated and is seen in the resulting increase in SAR. From the expression of (7.19), the addition of this second component (*i.e.*, a non-zero B_e) adds an approximate factor of two increase in SAR and ΔT. This is shown in the results of Figure 7-4(a) through (f). All other comments of the prior paragraphs remain true.

Sinusoidal Field Excitation in the presence of B_0

After the addition of the B_0 field which characterizes MRI, the most striking result is the large decrease in both SAR and ΔT. This decrease is greater as B_0 increases. The presence of B_0 causes the fluid to approach saturation far more rapidly than occurs in the presence of the rotating field. Saturation impedes nanoparticle rotation, and hence, heat generation, since one can imagine a larger fraction of the nanoparticles remain saturated, collinear with B_0, and do not respond to the sinusoidal field excitation orthogonal to B_0, along the x axis. This result is supported by comparing the resulting ΔT from Figures 7-2, where there is no B_0 field and 7-5, where the B_0 field is present. Since the DC B_0 field itself does not add or subtract heat from the fluid, the dramatic change in heating can only be accounted for by the partial magnetic saturation which occurs in its presence. Furthermore, with this increase in saturation of the fluid, the SAR dependence on particle radius is determined primarily by the denominators of (7.1) and (7.2) rather than the ratio of M_0/H_0 which tends to be invariant with r as field strength increases. For this reason, the peak SAR and ΔT tends to be much sharper than in the absence of B_0. Also, the peak is now increasingly centered around $\Omega\tau = 1$, and the peak tends to be closer to $\Omega\tau = 1$ as B_0 increases (thereby causing more saturation for any given particle radius).

SAR and ΔT still increase linearly in the presence of B_0 (see Figure 7-5(a) and (b))

although the dependence on H_e is approximately square so that when H_e is doubled, SAR quadruples etc. The relation is not perfect since there is still some dependence of M_0/H_0 on the particle radius. Finally, the relation to excitation frequency, Ω, is approximately linear, as expected from (7.20) although there is some influence from the $\Omega\tau$ term in the denominator of the magnetization expressions, as described in the previous sections.

Rotating Field Excitation in the presence of B_0

The results for a rotating field in addition to the B_0 field are easily reconciled with the previous results. A factor of two increase in SAR and ΔT is recorded compared to the case of a sinusoidal waveform. All other notes from the prior paragraph remain valid.

7.3 Conclusions

SAR and ΔT are increased by a factor of two in the presence of a rotating magnetic field compared to a purely sinusoidal magnetic field. This is not a scenario that has previously been examined in the context of hyperthermia and thermoablation and may be of interest to the reader. More relevant to this thesis is the finding that, in the presence of the B_0 field characteristic of open MRI systems (where B_0 might vary between 0.1 T and 0.35 T), SAR is reduced significantly although appreciable changes in temperature are still envisaged. The results of Figure 7-6 suggest that the proposal of Chapter 2 (the application of rotating field transverse to B_0 to generated modulated magnetic fluid magnetization) be coupled to the application of magnetic nanoparticles in hyperthermia treatment.

Chapter 8

Summary and Future Work

8.1 Summary of Thesis Contributions

This thesis represents the first attempt to integrate the fields of MRI and the dynamic behavior of magnetic fluids, in particular, the unusual properties of magnetic fluids in rotating magnetic fields. The novel contributions from the thesis are summarized here.

- The strong dependence of T1 and T2 relaxation times on the superparamagnetic nanoparticle radius has been demonstrated (Ch. 1). By comparison with transmission electron microscopy, it has been shown that, with knowledge of the water's relaxation time constants, an accurate prediction of the particle radius can be made based on the measured T1 and T2 times for the suspension.

- It has been demonstrated that MRI can be used to accurately quantify magnetization due to MRI contrast agents (Ch 5). This was accomplished using a 3T MRI system for two types of contrast agent: paramagnetic Gd-based Magnevist and superparamagnetic SPIO-based Feridex. The results closely agreed

with measurements made using vibrating sample magnetometery.

- The work presented, for the first time, a modified Langevin relation for non-saturated superparamagnetic suspensions in MRI (Ch 1, App. A) . This was achieved by means of a small-signal linearization about the operating point, determined by the B_0 field of the MRI, where the AC rotating field was represented as small-signal perturbations about the operating point.

- The change in magnetic fluid magnetization was simulated in the presence of magnetic particle spin in MRI. The spin was achieved by a rotating magnetic field (Ch. 2). The effect of flow and the field's orientation were investigated (Ch. 3).

- The non-ohmic heating associated with superparamagnetic fluid suspensions due to a rotating field was investigated for the first time by means of numerical simulation and theoretical analysis (Ch. 7). The analysis was extended to find the effect of the MRI's B_0 field.

- The presence of linear magnetic forces on magnetic fluid flow in MRI was investigated for the typical dosages of commercial contrast agents at 3 T and 7 T MRI (Ch. 6). The forces were not found to be significant compared to typical *in vivo* pressure drives.

8.2 Proposals for Future Work

The proposals for future work are divided into three distinct categories: (i) a proposal for a coupled MRI-hyperthermia system using magnetic nanoparticles for selective heating, (ii) demonstration of nanoparticle spin using ultra-low field MRI and (iii)

design of *in vivo* ferrofluid pumping techniques for targeted drug delivery.

8.2.1 Coupling MRI and Hyperthermia with Magnetic Nanoparticles

As shown in the analysis and results of Chapter 7, the heating effects of magnetic nanoparticles due to rotating magnetic fields is considerable even in low-field MRI. This result suggests a combination of low-field MRI, which could be used for diagnostic purposes, and the use of magnetic nanoparticles for selective hyperthermia in cancer therapy. Much analysis remains undone in this area, particularly with respect to the nanoparticles' behavior. It would be of use to examine the effects of blood perfusion on the expected *in vivo* temperature rise as well as expanding the tissue conduction work of Andra [84]. Currently, the analysis uses the evaluated SAR to calculate the expected rise in temperature. However, since the SAR is determined assuming an adiabatic process, it seems that that a more rigorous examination based on the laws of thermodynamics is in order. Also worth examining is the effect of *smart* nanoparticles (those agents which can intelligently bond to selective tissue types *in vivo* [1, 2]) so that clinicians can accurately predict what concentration of magnetic material is available at the tumor site for hyperthermia.

8.2.2 Nanoparticle Spin using Ultra-low Field MRI

Based on the analysis of Chapters 2 and 3, it should be of significant experimental interest to determine if magnetic nanoparticle spin can be used to change image intensity in MRI. This work suggests that this is best achieved at very low DC field so that the rotating magnetic field can be used to arbitrarily rotate the magnetic nanoparticles, unencumbered by magnetic saturation effects. As noted in Ch. 3, the

use of ultra-low field MRI has been demonstrated as a feasible imaging technique for clinical applications with a main field strength in the range of μT [110]. Adding a rotating field on the order of mT to such a system, which would allow interaction with the magnetic nanoparticles, presents one possible scenario of investigating ferrofluid spin in the MRI environment.

8.2.3 Ferrofluid Pumping for Targeted Drug Delivery

This is not a new proposal but, since the theoretical basis rests heavily on the work of chapters 2 and 3 of this thesis, the author believes that this may represent the most promising avenue for clinical application of magnetic nanoparticles in MRI. Using the nanoparticles as a passive contrast agent (as shown in Ch. 1), the position of the magnetic nanoparticles could be predicted *in vivo*. Applied standing waves cause the nanoparticles to move towards the target area [114, 115]. Obviously, the technique is most suited to applications where the vasculature is close to the skin surface (*e.g.*, in the leg or arm) and one critical goal of the work would be to determine the required nanoparticle concentration *in vivo*, necessary to successfully move the magnetic nanoparticles, and thereby the nanoparticle-bound drug, to the subject's target area.

Appendix A

Linearization of the Langevin Function

A.1 Introduction

The Langevin relation relates the ratio of the magnetic to thermal energy densities in a ferrofluid [42]. It takes the form of (A.1) and $L(\alpha)$ describes the portion of the magnetic nanoparticles in the ferrofluid that align with a constant, external, magnetic field, of magnitude $|\mathbf{H}|$. The Langevin parameter, α, is a function of the magnetic field magnitude $|\mathbf{H}|$ within the ferrofluid, as given by (A.2) where M_d is the single domain magnetization of the particle (assumed magnetite), V_p is the particle magnetic volume, μ_0 is the permeability of free space, k is Boltzmann's constant and T is the absolute temperature. The ferrofluid saturation magnetization M_s is related to M_d by the fraction solid volume in the suspension, denoted by ϕ where $M_s = \phi M_d$.

$$\mathbf{M}_{eq} = \mathbf{M}_s L(\alpha) = \mathbf{M}_s(\coth(\alpha) - 1/\alpha) \tag{A.1}$$

$$\alpha = \frac{M_d V_p \mu_0 |\mathbf{H}|}{kT} \tag{A.2}$$

A.2 Linearization of the Langevin Relation

Linearization of the Langevin function can be performed about a DC operating point defined by the DC magnetic field intensity H_0. It is assumed that there are no large-signal DC components directed along $\boldsymbol{i}_x$ or $\boldsymbol{i}_y$, which are unit vectors along the x and y axes respectively, so that H_0 is directed along $\boldsymbol{i}_z$, the unit vector along z. Additional small-signal perturbations about that operating point along $\boldsymbol{i}_x$, $\boldsymbol{i}_y$ and $\boldsymbol{i}_z$ are denoted by $\tilde{h}_x$, $\tilde{h}_y$ and $\tilde{h}_z$ respectively leading to the expression in (A.4).

$$\mathbf{H} = h_X \boldsymbol{i}_x + h_Y \boldsymbol{i}_y + h_Z \boldsymbol{i}_z \tag{A.3}$$

$$\mathbf{H} = \tilde{h}_x \boldsymbol{i}_x + \tilde{h}_y \boldsymbol{i}_y + (H_0 + \tilde{h}_z) \boldsymbol{i}_z \tag{A.4}$$

Similarly for the associated equilibrium magnetization vector, $\mathbf{M}_{eq}$ where the components of magnetization due to the perturbations along $\boldsymbol{i}_x$, $\boldsymbol{i}_y$ and $\boldsymbol{i}_z$ are denoted $\tilde{m}_{xo}$, $\tilde{m}_{yo}$ and $\tilde{m}_{zo}$ respectively.

$$\mathbf{M}_{eq} = m_X \boldsymbol{i}_x + m_Y \boldsymbol{i}_y + m_Z \boldsymbol{i}_z \tag{A.5}$$

$$\mathbf{M}_{eq} = \tilde{m}_{xo} \boldsymbol{i}_x + \tilde{m}_{yo} \boldsymbol{i}_y + (M_0 + \tilde{m}_{zo}) \boldsymbol{i}_z \tag{A.6}$$

Under equilibrium conditions, the magnetic field and the magnetization vectors will be colinear. Therefore $\mathbf{H}$ and $\mathbf{M}_{eq}$ are collinear and (A.6) can be written in terms of (A.4).

$$\mathbf{M}_{eq} = M_s L(\alpha) \frac{\tilde{h}_x \boldsymbol{i}_x + \tilde{h}_y \boldsymbol{i}_y + (H_0 + \tilde{h}_z)\boldsymbol{i}_z}{\sqrt{(\tilde{h}_x)^2 + (\tilde{h}_y)^2 + (H_0 + \tilde{h}_z)^2}} \tag{A.7}$$

Considering a first-order Binomial expansion of the denominator of (A.7), one can rewrite the expression for $\mathbf{M}_{eq}$ as (A.8).

$$\mathbf{M}_{eq} \approx M_s L(\alpha) \frac{\tilde{h}_x \boldsymbol{i}_x + \tilde{h}_y \boldsymbol{i}_y + (H_0 + \tilde{h}_z)\boldsymbol{i}_z}{H_0} (1 - \frac{\tilde{h}_z}{H_0}) \tag{A.8}$$

The Langevin parameter α is written as the linear sum of contributions due to the Langevin function evaluated at the operating point (denoted α_0) and the contribution due to the small-signal perturbations (denoted α'). The terms α_0 and α' are evaluated by a first-order Binomial expansion of (A.2) where $|\mathbf{H}|$ is given by (A.4) to yield (A.12) and (A.13).

$$\alpha = \alpha_0 + \alpha' \tag{A.9}$$

$$\alpha = \frac{M_d V_p \mu_0}{kT} \sqrt{(\tilde{h}_x)^2 + (\tilde{h}_y)^2 + (H_0 + \tilde{h}_z)^2} \tag{A.10}$$

$$\alpha \approx \frac{M_d V_p \mu_0}{kT} H_0 (1 + \frac{\tilde{h}_z}{H_0}) \tag{A.11}$$

$$\Rightarrow \alpha_0 = \frac{M_d V_p \mu_0 H_0}{kT} \tag{A.12}$$

$$\Rightarrow \alpha' = \alpha_0 \frac{\tilde{h}_z}{H_0} \tag{A.13}$$

Simplifying $L(\alpha)$ using a first-order Taylor Series expansion, leads to (A.16).

$$L(\alpha) = \coth(\alpha_0 + \alpha') - \frac{1}{\alpha_0 + \alpha'} \tag{A.14}$$

$$L(\alpha) \approx L(\alpha_0) + \frac{\partial L(\alpha)}{\partial \alpha}|_{\alpha=\alpha_0} \alpha' \tag{A.15}$$

$$L(\alpha) \approx \coth(\alpha_0) - \frac{1}{\alpha_0} - \frac{\alpha'}{\sinh^2(\alpha_0)} + \frac{\alpha'}{\alpha_0^2} \tag{A.16}$$

Substituting for $L(\alpha)$ in (A.8) allows the constituent components of $\mathbf{M}_{eq}$ to be expressed as follows and the component due to the DC H_0 field, which is z-directed, is given by (A.20).

$$\tilde{m}_{xo} \approx M_s L(\alpha_0) \frac{\tilde{h}_x}{H_0} \approx \frac{M_0}{H_0} \tilde{h}_x \tag{A.17}$$

$$\tilde{m}_{yo} \approx M_s L(\alpha_0) \frac{\tilde{h}_y}{H_0} \approx \frac{M_0}{H_0} \tilde{h}_y \tag{A.18}$$

$$\tilde{m}_{zo} \approx M_s \left(\frac{-\alpha_0}{\sinh^2 \alpha_0} + \frac{1}{\alpha_0}\right) \frac{\tilde{h}_z}{H_0} \approx \frac{\partial M_0}{\partial H_0} \tilde{h}_z \tag{A.19}$$

$$M_0 = M_s L(\alpha_0) \tag{A.20}$$

The expressions of (A.17) through (A.20) show that for z-directed perturbations, the relationship between the small signal magnetic field and the resultant magnetization is due to the slope of the Langevin relation evaluated at the DC operating point defined by H_0. When the perturbations are either x or y-directed, the relationship between the small signal magnetic field and the resultant magnetization is related by the ratio M_0/H_0. Comparing these two relations, it is easily shown that the two relations are approximately equal in the low-field limit, when the DC field determining the operating point becomes comparable with the small-signal perturbations, as shown in Fig. A-1 for the typical numerical values of magnetic particle radii (4 nm). As the B_0 field increases, the value of M_0/H_0 exceeds the slope of the Langevin function evaluated at the operating point for all values of DC field, as shown in Figure A-1.

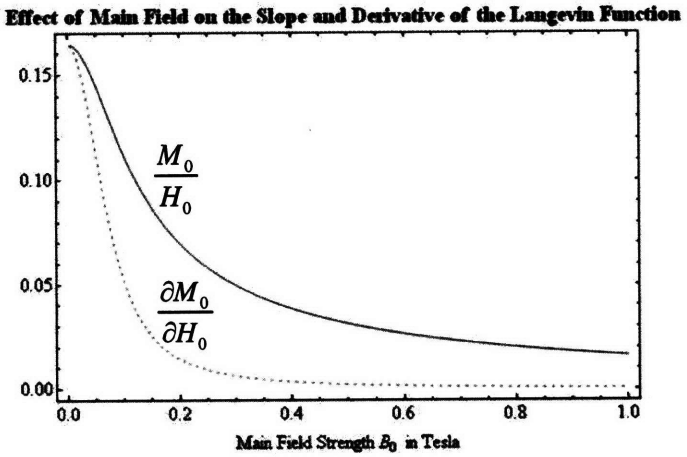

Figure A-1: The values of M_0/H_0 and $\frac{\partial M_0}{\partial H_0}$ are plotted for the parameters of Table 3.1 including a particle core radius of 4 nm. As expected, the values converge in the low-field limit.

Appendix B

Defining Contrast Agent Concentration

Throughout this thesis, every effort has been made to maintain consistent units of contrast agent concentration. However, in light of the many formulations that appear in the literature, a number of clarifying comments are offered.

B.1 Ferrofluids and SPIO Contrast Agents

In general, workers in the traditional applications of ferrofluids will use the solid volume fraction to define concentration [42, 47, 48, 90]. The fraction indicates the volume of magnetic nanoparticles as a fraction of the total volume of solution and is usually denoted as ϕ. This is the approach applied for all of the work in this thesis unless otherwise stated.

However, in MRI, it makes little sense to speak in terms of ϕ since the total volume of the solution is often unknown or indeterminate (*e.g.*, the total blood volume of the patient to whom the agent is being administered). Therefore, SPIO contrast agents

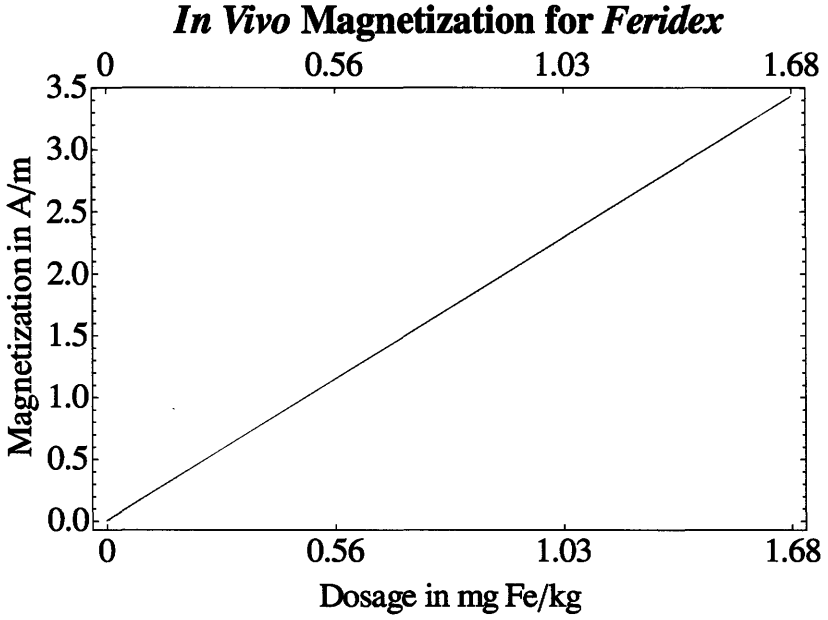

Figure B-1: *In vivo* magnetization is plotted in units of $A \cdot m^{-1}$, for a person of 70 kg with a total blood volume of 4 liters, as a function of the administered dose of Feridex. The recommended dosage is 0.56 mg Fe/kg.

are commonly referred to in terms of their recommended dosage in mg of Fe per kg of bodyweight. The majority of SPIO agents are comprised of magnetite (Fe_3O_4) [59]. As of February 2008, the sole FDA-approved SPIO agent available in the US is Feridex [59], manufactured by AMAG Pharmaceuticals, Cambridge, Massachusetts. The recommended dosage for Feridex is 0.56 mg Fe per kg. For a human weighing 70kg, this corresponds to a total dosage of 39.2 mg Fe or, given the molar composition of magnetite, 54.14 mg of Fe_3O_4. Magnetite has a density of 5210 $kg \cdot m^{-3}$ [42], yielding a total *in vivo* solid volume of 1×10^{-8} m^3 Fe_3O_4. Considering the total *in vivo* blood volume to be 4 liters [103], this corresponds to an *in vivo* value for ϕ, after administration of the recommended dosage of Feridex, of 2.6×10^{-6}.

An additional source of confusion is due to the nomenclature arising in theoretical

studies of T1 and T2 relaxation time. In the works of Gillis et al. [8, 10–13, 16], a third terminology is employed. Here, the preferred unit of concentration is the molar concentration in moles of Fe per liter, usually denoted C (see Eqs. (1.17) and (1.18) of Chapter 1). The *liter* arises due to the use of *cgs* units. In addition, the unit is often written [8, 12, 16] as "mM" which corresponds to millimoles of Fe per liter of solution. The reference to Fe or to the control volume is seldom included. Since one mole of Fe corresponds to 56 grams, the recommended dosage of Feridex, corresponds to an *in vivo* value of $C = 1.75\times10^{-4}$ moles Fe per liter. Again, the *in vivo* blood volume is considered to be 4 liters.

Table B.1 lists factors of the recommended dosage for Feridex SPIO contrast agent and each of the corresponding units of concentration described above. As well as the molar concentration, C, the mass concentration, C_m in mg Fe per liter is also included.

Feridex dose in mg Fe/kg	Feridex dose in mol Fe/kg	*In vivo* ϕ	*In vivo* C_m in mg Fe per liter	*In vivo* C in mol Fe per liter
0.28	5×10^{-6}	1.3×10^{-6}	4.93	0.88×10^{-4}
0.56	10×10^{-6}	2.6×10^{-6}	9.86	1.75×10^{-4}
1.12	20×10^{-6}	5.2×10^{-6}	19.6	3.5×10^{-4}
1.68	30×10^{-6}	7.8×10^{-6}	29.6	5.25×10^{-4}

Table B.1: Units of *in vivo* concentration for Feridex using all units of concentration found in the literature. The *in vivo* values assume a human bodyweight of 70 kg and a total *in vivo* blood volume of 4 liters. Fe has a molar mass of 56 g. The recommended (1x) dosage is 0.56 mg Fe/kg bodyweight.

While insightful, the concentration of the agent *in vivo* gives no indication of the *in vivo* magnetization associated with the SPIO agent. To quantify this magnetization,

one needs to make some assumptions regarding the saturation of the agent *in vivo*. The agent saturation is determined by the Langevin relation (see Fig. 1-4). However, as this figure clearly represents, all SPIO agents of realistic particle size will be fully saturated at clinical MRI strengths beyond 1 T. Therefore, the *in vivo* magnetization, M, is simply given by $M = \phi M_d$ where M_d is the single-domain magnetization of magnetite, with a value of 446×10^3 A·m^{-1}. The resulting *in vivo* magnetization is plotted in Fig. B-1, again for a person of 70 kg with a total blood volume of 4 liters.

B.2 Gd Contrast Agents

Unlike SPIO contrast agents, Gd agents are complex molecular structures which contain long chains of bonding atoms around the Gd ion (Gd^{3+}). The agent considered in this work is Magnevist, with a molecular structure of $C_{28}H_{54}GdN_5O_{20}$. The recommended dosage is expressed in molarity rather than in mass, as is the case for Feridex. The prescribed dosage for *Magnevist* is 0.1 millimoles of agent per kg bodyweight. However, recognizing that each mole of the agent corresponds to approximately 6 moles of Gd, the recommended dosage is 0.6 millimoles Gd per kg. After the agent is injected into the subject, it is diluted in the subject's bloodflow, which acts as the agent's solvent. For *in vivo* administration to a normal, healthy adult with a total blood volume 4 liters [103], this corresponds to an *in vivo* Gd concentration $C = 10.43$ mM Gd (*i.e.*, millimoles of Gd per liter of blood volume *in vivo*). The various possible concentration units for *Magnevist* for recommended dosages and *in vivo* concentration are shown in Table B.2.

Magnevist dose in mg Gd/kg	Magnevist dose in mol Gd/kg	*In vivo* ϕ	*In vivo* C_m in mg Gd per liter	*In vivo* C in mol Gd per liter
7.85	0.5×10^{-4}	-	820	5.22×10^{-3}
15.7	1×10^{-4}	-	1639	10.43×10^{-3}
31.4	2×10^{-4}	-	3278	20.86×10^{-3}
47.1	3×10^{-4}	-	5067	31.29×10^{-3}

Table B.2: Units of *in vivo* concentration for Magnevist using all units of concentration found in the literature. The *in vivo* values assume a human bodyweight of 70 kg and a total *in vivo* blood volume of 4 liters. The solid fraction volume is a meaningless parameter for Gd agents since much of the particle mass is non-magnetic. Gd has a molar mass of 157 g. The recommended (1x) dosage is 15.7 mg Gd/kg bodyweight.

Gadolinium agents remain magnetically unsaturated up to main fields of about 50 T [9] so that the agent's magnetization is linearly proportional to the applied magnetic field intensity, H, with the constant of proportionality being the magnetic susceptibility. The results of Chapter 5 yielded a value for χ_m, the mass susceptibility, of 1.8×10^{-6} m^3/kg Gd as measured by MRI. Assuming that the agent's magnetization is significantly less than the strength of the main field ($M \ll B_0/\mu_0$), then the Gd agent's *in vivo* magnetization is given by (B.1), where C_m is the mass concentration in mg Gd/liter and the mass susceptibility is expressed in liters/mg Gd. For the value from the MRI measurement, this is equivalent to 1.8×10^{-9} liters/mg Gd. The *in vivo* magnetization is plotted for $B_0 = 1.5$ T, 3 T and 7 T in Fig. B-2 as a function of the dosage in mmol of agent per kg bodyweight. As already noted, the magnetization is a function of field since the Gd agent is not magnetically saturated. Also, the recommended dosage (usually expressed in units of moles of agent rather moles of Gd) is 0.1 mmol/kg which corresponds to 0.6 mmol Gd/kg.

$$M \approx \chi_m \frac{B_0}{\mu_0} C_m \tag{B.1}$$

Comparing Figs. B-1 and B-2 it is clear that the *in vivo* magnetization is increased using Gd compared to SPIO agents. This is somewhat counter-intuitive since Gd is a paramagnetic species and significantly less magnetic than the superparamagnetic nanoparticles. However, the concentrations administered as recommended dosages ensure that there is such an abundance of Gd ions per unit blood volume, that the Gd agent has more appreciable net effect than the SPIO agent on the *in vivo* magnetization.

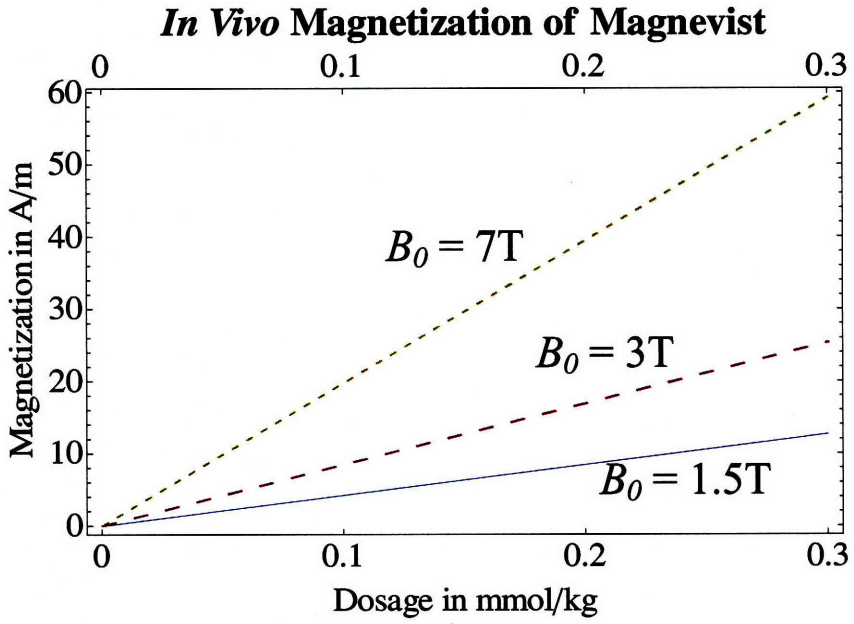

Figure B-2: *In vivo* magnetization is plotted in units of $\text{A}\cdot\text{m}^{-1}$, for a person of 70 kg with a total blood volume of 4 liters, as a function of the administered dose of Magnevist in mmol/kg. The recommended dosage is 0.1 mmol/kg.

Appendix C

Prior Work on T1 and T2 Characterization

Preliminary investigations were undertaken by Professor Adalsteinsson to characterize the T1 and T2 relaxation times associated with dilutions of MSG-W11 ferrofluid with distilled water at $B_0 = 1.5$ T. These investigations, led to the results of Fig. C-1 and provided the impetus for the work of this thesis. The ferrofluid was diluted by three different amounts, $\phi_1 = 2.75 \times 10^{-2}$, $\phi_2 = 2.75 \times 10^{-6}$ and $\phi_3 = 2.75 \times 10^{-8}$. A control sample of distilled water was also used. For each sample, the corresponding T1 and T2 times were characterized.

C.1 Experiments

A series of spin-echo MR images were acquired with increasing repetition times (TR), but with a fixed, short echo time (TE=14 ms). These data were used to estimate T1, since the amount of signal recorded for each vial is exponentially related to T1, as given by Eq. (C.1). The signal is also weighted by T2 due to the echo time, TE,

but this weighting is constant for each solution and does not interfere with the T1 estimate. The values investigated for TR were 83, 167, 500, 600 and 2000 ms. The results are shown in Figure C-1.

$$S(t) \propto 1 - e^{-\frac{TR}{T1}} \tag{C.1}$$

A second data set with increasing echo times (TE) at a fixed, long repetition rate (TR = 5000 ms) was acquired to estimate T2, since the signal, in this case, is exponentially weighted by TE. When T1 is a significant fraction of TR (as is the case for the distilled water solution), a better model for the recorded signal requires knowledge of T1, as given by Eq. (C.2). The value of TE was varied between 0 and 800 ms and the results are shown in Figure C-1.

$$S(t) \propto (1 - e^{-\frac{TR}{T1}} - 2e^{-\frac{TR-TE/2}{T1}})e^{-\frac{TE}{T2}} \tag{C.2}$$

A single slice through the center of the vials was used for analysis. A rectangular area within each vial was used to estimate mean and standard deviation for the T1 and T2 data sets. A nonlinear, least-squares fit to the increase in signal due to increased TR was used to estimate T1 whereas the signal decay as a function of increasing echo time was used to estimate T2 by including the prior estimates of T1. In all cases, the image acquisition consisted of six contiguous, coronal slices, 8 mm thick, with 256×160 pixels over a 16 cm field-of-view.

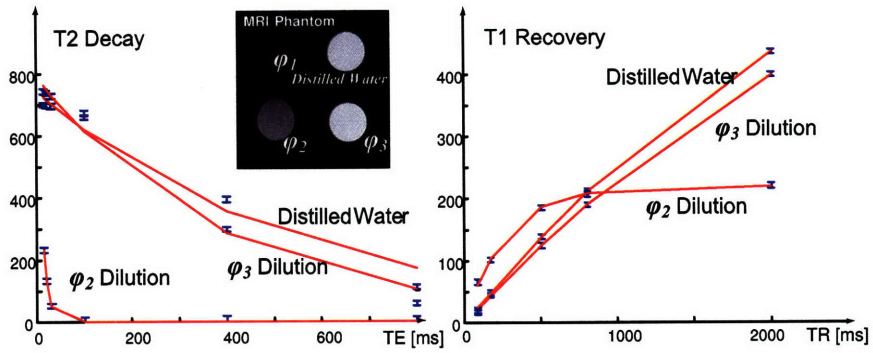

Figure C-1: The insert shows the layout of four vials in the MRI phantom constructed to evaluate the relaxation properties of diluted solutions of water-based ferrofluid. The upper left quadrant has $\phi_1 = 2.75 \times 10^{-4}$ dilution and by its signal void shows that the ferrofluid is a strong negative T2 contrast agent. Left: Decay of MR-visible signal with increasing TE with TR=5s. The $\phi_2 = 2.75 \times 10^{-6}$ solution clearly has a dramatically shorter T2 than the distilled water and the $\phi_3 = 2.75 \times 10^{-8}$ solution. Right: Signal recovery with increasing TR for TE=14 ms with substantial shortening of T1 for the ϕ_2 vial of ferrofluid.

C.2 Results

Based on the results shown in Fig. C-1, the ϕ_1 dilution was too highly concentrated to yield any significant SNR at 1.5 T. This is seen by the top-left image in the insert of Fig. C-1, where the vial is indistinguishable from the background noise. However, the ϕ_2 and ϕ_3 dilutions yield much-improved SNR.

The values of T1 and T2 were estimated based on an exponential curve fit of the plots in Fig. C-1. This yields a T1 value for the ϕ_2 dilution of 260 ms while the value for ϕ_3 dilution was 3000 ms. Similarly, the T2 relaxation times was estimated for each concentration and for ϕ_2, the value was 11 ms. This value increased to 470 ms

for ϕ_3. For the distilled water, the values of T1 and T2 were estimated as 3200 ms and 570 ms respectively.

It should be noted that the estimate of T2 for long T2 species is not thought to be accurate. This is due to both T1 effects (T1 is substantial compared to TR), as well as imaging artifacts at the very late echo times. The T2 measurement of the current reference solution could be improved by lengthening TR or by applying an alternate T2 measurement methodology (e.g., "T2 preparation" sequences as are used in flow-independent MR angiography). The T2 estimates of the reference solution could also be improved by doping them to reduce T1 and T2 to a few hundred milliseconds.

Bibliography

[1] A. Moore, Z. Medarova, A. Potthast, and G. Dai, "In vivo targeting of underglycosylated MUC-1 tumor antigen using a multimodal imaging probe," Cancer Research, Vol. 64, 2004, pp. 1821-1827.

[2] Z. Tyeklar, S.U. Dunham, K. Midelfort, D.M. Scott, H. Sajiki, K. Ong, R.B. Lauffer, P. Caravan, and T.J. McMurry, "Structural, kinetic, and thermodynamic characterization of the interconverting isomers of MS-325, a gadolinium(III)-based magnetic resonance angiography contrast agent," Inorganic Chemistry, Vol. 46, No. 16, pp. 6621-6631.

[3] Y. Liu, H. D'Arceuil, J. He, M. Duggan, S. Seri, Y. Hashiguchi, A. Nakatani, R.G. Gonzalez, J. Pryor and A. de Crespigny, "Dynamic susceptibility contrast perfusion imaging of cerebral ischemia in nonhuman primates: comparison of Gd-DTPA and NMS60," Journal of Magnetic Resonance Imaging, Vol. 22, No. 4, 2005, pp. 461-466.

[4] H.E. DArceuil, A.J. de Crespigny, L. Pelc, D. Howard, S. Seri, Y. Hashiguchi, A. Nakatani and M.E. Moseley, "A Comparison of CH3-DTPA-GD (NMS60) and GD-DTPA for Evaluation of Acute Myocardial Ischemia," The International Journal of Cardiovascular Imaging, Vol. 21, No. 5, 2005, pp. 539-547.

[5] J.B. Mandeville, B.G. Jenkins, Y.C. Chen, Y.C., J.K. Choi, Y.R. Kim, D. Belen, C. Liu, B.E. Kosofsky and J.J. Marota, "Exogenous contrast agent improves sensitivity of gradient-echo functional magnetic resonance imaging at 9.4 T," Magnetic Resonance in Medicine, Vol. 52, No. 6, 2004, pp. 1272-1281.

[6] R.C. Walker, G.L. Purnell, L.B. Jones-Jackson, K.L. Thomas, J.A. Brito and E.J. Ferris, "Introduction to PET Imaging with Emphasis on Biomedical Research," NeuroToxicology, Vol. 25, Issue 4, 2004, pp. 533-542.

[7] M. Zahn and E. Adalsteinsson, 2005, Systems and Methods for Tuning Properties of Nanoparticles, US Patent Application 60/719681

[8] R. Muller, P. Gillis, F. Moiny and A. Roch, "Transverse Relaxivity of Particulate MRI Contrast Media: from Theories to Experiment," Magnetic Resonance in Medicine, Vol. 22, 1991, pp. 178-182.

[9] S.H. Koenig and K.E. Kellar, "Theory of 1/T1 and 1/T2 NMRD Profiles of Solutions of Magnetic Nanoparticles," Magnetic Resonance in Medicine, Vol. 34, 1995, pp. 227-233.

[10] P. Gillis, A. Roch and R.A Brooks, "Corrected Equations for Susceptibility-Induced T2-Shortening," Journal of Magnetic Resonance, Vol. 137, 1999, pp. 402-407.

[11] A. Roch, R.N. Muller and P. Gillis, "Theory of Proton Relaxation Induced by Superparamagnetic Particles," Journal of Chemical Physics, Vol. 110, No. 11, 1999, pp. 5403-5411.

[12] R.A. Brooks, F. Moiny and P. Gillis, "On T2-Shortening by Weakly Magnetized Spheres: The Chemical Exchange Model," Magnetic Resonance in Medicine, Vol. 45, 2001, pp. 1014-1020.

[13] Y. Goussin, P. Gillis and F. Lo Bue, "Susceptibility-Induced T2-Shortening and Unrestricted Diffusion," Magnetic Resonance in Medicine, Vol. 47, 2002, pp. 194-195.

[14] J.H. Jensen and R. Chandra, "NMR Relaxation in Tissues with Weak Magnetic Inhomogeneities," Magnetic Resonance in Medicine, Vol. 44, 2000, pp. 144-156.

[15] J.H. Jensen and R. Chandra, "Strong Field Behavior of the NMR Signal from Magnetically Heterogeneous Tissues," Magnetic Resonance in Medicine, Vol. 43, 2000, pp. 226-236.

[16] J.W.M. Bulte, R.A. Brooks, B.M. Moskowitx, L.H. Bryant and J.A. Frank, "Relaxometry and Magentometry of MR Contrast Agent MION-46L," Magnetic Resonance in Medicine, Vol. 42, 1999, pp. 379-384.

[17] D.A. Yablonskiy and E.M. Haacke, "Theory of NMR Signal Behavior in Magnetically Inhomogenous Tissues: the Static Dephasing Regime," Magnetic Resonance in Medicine, Vol. 32, 1994, pp. 749-763.

[18] R.M. Weisskoff, C.S. Zuo, J.L. Boxerman and B.R. Rosen, "Microscopic Susceptibility Variation and Transverse Relaxation: Theory and Experiment," Magnetic Resonance in Medicine, Vol. 31, 1994, pp. 601-610.

[19] V.G. Kiselev and S. Posse, "Analytical Model of Susceptibility-Induced MR Signal Dephasing: Effects of Diffusion in a Microvascular Network," Magnetic Resonance in Medicine, Vol. 41, 1999, pp. 499-509.

[20] N. Bloembergen, "Proton Relaxation Times in Paramagnetic Solutions," Journal of Chemical Physics, Vol. 27, 1957, pp. 572-573.

[21] H.C. Torrey, "Bloch Equations with Diffusion Terms," Physical Review, Vol. 104, No. 3, 1956, pp. 563-565.

[22] H.Y. Carr and E.M. Purcell, "Effects of Diffusion on Free Precession in Nuclear Magnetic Resonance Experiments," Physical Review, Vol. 94, No. 3, 1954, pp. 630-644.

[23] J.H. Freed, "Dynamic effects of pair Correlation functions on spin relaxation by translational diffusion in liquids," Journal of Chemical Physics, Vol. 68, No. 9, 1978, pp. 4034-4037

[24] R.B. Lauffer, "Paramagnetic Metal Complexes as Water Proton Relaxation Agents for NMR Imaging: Theory and Design," Chemical Reviews, Vol. 87, 1987, pp 901-927.

[25] P. Gillis and S.H. Koenig, "Transverse Relaxation of Solvent Protons Induced by Magnetized Spheres: Application to Ferritin, Erthrocytes and Magnetite," Magnetic Resonance in Medicine, Vol. 5, 1987, pp. 232-245.

[26] Y.J. Wang, S.M. Hussain and G.P. Krestin, "Superparamagnetic Iron Oxide Agents: Physiochemical Characteristics and Applications in MR Imaging," Journal of European Radiology, Vol. 11, 2001, pp. 2319-2331.

[27] A. Bjornerud and L. Johansson, "The utility of superparamagnetic contrast agents in MRI: theoretical consideration and applications in the cardiovascular system," NMR in Medicine, Vol. 17, 2004, pp.465-477.

[28] K.B. Saebo, "Degradation, Metabolism and Relaxation Properties of Iron Oxide Particles for Magnetic Resonance Imaging," *PhD Thesis.* Uppsala University, Sweden, 2004.

[29] R. Mills, "Self-diffusion in normal and heavy water in the range 145°C," Journal of Physical Chemistry, Vol. 77, 1973, pp. 685-688.

[30] K.F. King, A. Ganin, X.J. Zhou and M.A. Bernstein,"Concomitant Gradient Field Effects in Spiral Scans," Magnetic Resonance in Medicine, Vol. 41, 1999, pp. 103-112.

[31] X.J. Zhou, Y.P. Du, M.A. Bernstein, H.G. Reynolds, J.K. Maier and J.A. Polzin, "Concomitant Magnetic-Field-Induced Artifacts in Axial Echo Planar Imaging," Magnetic Resonance in Medicine, Vol. 39, 1998, pp. 596-605.

[32] M.A. Bernstein, K.F. King and X.J. Zhou, *Handbook of MRI Pulse Sequences.* New York: Elsevier Academic Press, 1999, pp. 292ff.

[33] M.A. Bernstein, X.J. Zhou, K.F. King, J.A. Polzin, A. Ganin, N.J. Pelc and G.H. Glover, "Concomitant Gradient Terms in Phase Contrast MR: Analysis and Correction," Magnetic Resonance in Medicine, Vol. 39, 1998, pp.300-308.

[34] G.A. Wright, "Magnetic Resonance Relaxation Behavior of Blood: Study and Applications," *PhD Thesis.* Stanford University, 1991.

[35] E.M. Haacke, R.W. Brown, M.R. Thompson and R. Venkatesan, *Magnetic Resonance Imaging: Physical Principles and Sequence Design.* New York: John Wiley and Sons, 1999.

[36] Stewart C. Bushong, *Magnetic Resonance Imaging: Physical and Biological Principles.* New York: Mosby, Inc., 1996.

[37] D.G. Nishimura, *Principles of Magnetic Resonance Imaging.* Stanford University, 1996.

[38] U. Hafeli, W. Schutt, J. Teller and M. Zborowski (eds.), *Scientific and Clinical Applications of Magnetic Carriers.* New York: Plenum Press, 1997.

[39] M.T. Vlaardingerbroek and J.A. den Boer, *Magnetic Resonance Imaging.* New York: Springer Publishing, 1996.

[40] X. Li, E.T. Han, C.B. Ma, T.M Link, D.C. Newitt, and S. Majumdar, "In Vivo 3T Spiral Imaging Based Multi-Slice $T_{1\rho}$ Mapping of Knee Cartilage in Osteoarthritis," Magnetic Resonance in Medicine, Vol. 54, 2005, pp. 929-936.

[41] A.J. Wheaton, A. Borthakur, M.T. Corbo, G. Moonis, E. Melham and R. Reddy, "$T_{2\rho}$-Weighted Contrast in MR Images of the Human Brain," Magnetic Resonance in Medicine, Vol. 52, 2004, pp. 1223-1227.

[42] R.E. Rosensweig, *Ferrohydrodynamics.* New York: Dover Publications, 1997.

[43] M. Zahn, *Electromagnetic Field Theory: a problem solving approach.* Florida: Krieger Publishing Company, 2003.

[44] S.M. Elborai, "Ferrofluid Surface and Volume Flows in Uniform Rotating Magnetic Fields," *PhD Thesis.* Massachusetts Institute of Technology, 2006.

[45] X. He, "Ferrohydrodynamic Flows in Uniform and Non-uniform Rotating Magnetic Fields," *PhD Thesis.* Massachusetts Institute of Technology, 2006.

[46] C. Rinaldi, T. Franklin, M. Zahn and T. Cader, "Magnetic Nanoparticles in Fluid Suspension: Ferrofluid Applications," *Dekker Encyclopedia of Nanoscience and Nanotechnology*, 2004.

[47] M. Zahn and D. R. Greer, "Ferrohydrodynamic pumping in spatially uniform sinusoidally time-varying magnetic fields," Journal of Magnetism and Magnetic Materials, Vol. 149, pp. 165-173, 1995.

[48] M. Shliomis, "Effective Viscosity of Magnetic Suspensions," Soviet Physics JETP (Zhurnal Eksperimen-. taVnoi i Teoreticheskoi Fiziki), Vol. 34, 1972, pp.1291.

[49] M. Shliomis and Y. Raikher, "Experimental investigations of magnetic fluids," IEEE Transcations on Magnetics, Vol. 16, 1980, pp. 237-250.

[50] M. Shliomis, "Comment on Magnetoviscosity and relaxation in ferrofluids," Physical Review, Vol. 64, 2001.

[51] M. Shliomis, "Ferrohydrodynamics: Testing a Third magnetization equation," Physical Review, Vol. 64, 2001.

[52] A.F. Pshenichnikov, "Magnetic Fluid Motion driven by a high-frequency rotating magnetic field," Fluid Dynamics, Vol. 31, No. 1, 1996.

[53] J. Popplewell, R. Rosensweig and R.J. Johnston, "Magnetic field induced rotations in ferrofluids," IEEE Transactions on Magnetics, Vol. 26, pp. 1852 - 1854, 1990.

[54] A.V. Lebedev and A.F. Pshenichnikov, "Rotational effect: the influence of free or solid moving boundaries," Journal of Magnetism and Magnetic Material, Vol. 122, 1993, pp.227.

[55] A.-F. Lehlooh and S.H. Mahmood, "Mossbauer spectroscopy of Fe_3O_4 ultrafine particles," Journal of Magnetism and Magnetic Material, Vol. 151, 1995, pp.163.

[56] A.-F. Lehlooh, S.H. Mahmood and J.M. Williams, "On the particle size dependence of the magnetic anistropy energy constant," Physica B, Vol. 321, 2002, pp.159-162.

[57] L.W. Yeary, J.W. Moon, L.J. Love, J.R. Thompson, C.J. Rawn and T.J. Phelps, "Magnetic properties of biosynthesized magnetite nanoparticles," IEEE Transactions on Magnetics, Vol. 41, 2005, pp. 4384-4389.

[58] R.P. Morais, G.R.R. Goncalves, K. Skeff Neto, F. Pelegrini, N. Buske, "Study of particle-particle interaction in magnetic fluids using magnetic resonance," IEEE Transactions on Magnetics, Vol. 38, 2002, pp. 3225-3227.

[59] R. Weissleder, G. Elizondo, J. Wittenberg, C.A. Rabito, H.H. Bengele and L. Josephson, "Ultrasmall superparamagnetic iron oxide: characterization of a new class of contrast agents for MR imaging," Radiology, Vol. 175, 1990, pp.489-493.

[60] C.W. Jung and P. Jacobs, "Physical and Chemical Properties of Superparamagnetic Iron Oxide MR Contrast Agents: Ferumoxides, Ferumoxtran, Ferumoxsil," Magnetic Resonance Imaging, Vol. 13, 1994, pp. 661-674.

[61] Magnevist Patient Information, Bayer Healthcare.
http : //berlex.bayerhealthcare.com/html/products/pi/Magnevist_PI.pdf

[62] Feridex Patient Information, AMAG Pharmaceutical.
www.berlex.com/html/products/pi/Feridex_PI.pdf

[63] J.B. Mandeville, J. Moore, D.A. Chesler, L. Garrido, R. Weissleder and R.M.Weisskoff, "Dynamic liver imaging with iron oxide agents: Effects of size and biodistribution on contrast," Magnetic Resonance in Medicine, Vol. 37, 1997, pp.885-890.

[64] Y.J. Wang, S.M. Hussain and G.P. Krestin, "Superparamagnetic iron oxide contrast agents: physicochemical characteristics and applications in MR imaging," European Journal of Radiology, Vol. 11, 2001, pp.2319-2231.

[65] A. Roch, Y. Goussin, R.N. Muller and P. Gillis, "Superparamagnetic colloid suspensions: Water magnetic relaxation and clustering," Journal of Magnetism and Magnetic Material, Vol. 293, 2005, pp.532-539.

[66] C.H. Cunningham, T. Arai, P.C. Yang, M.V. McConnell, J.M. Pauly and S.M. Conolly, "Positive Contrast Magnetic Resonance Imaging of Cells Labeled with Magnetic Nanoparticles," Magnetic Resonance in Medicine, Vol. 53, 2005, pp.999-1005.

[67] A.J. de Crespigny, H.E. DArceuil, T. Engelhorn and M.E. Moseley, "MRI of Focal Cerebral Ischemia Using ^{17}O-Labeled Water," Magnetic Resonance in Medicine, Vol. 43, 2000, pp.876-883.

[68] E.H. Kim, H.S. Lee, B.K. Kwak and B-K. Kim, "Synthesis of ferrofluid with magnetic nanoparticles by sonochemical method for MRI contrast agent," Journal of Magnetism and Magnetic Material, Vol. 289, 2005, pp.328-330.

[69] D.K. Kim, W. Voit, W. Zapka, B. Bjelke, M. Muhammed and K.V. Rao, "Biomedical application of ferrofluids containing magnetite nanoparticles," Proceedings of the Materials Research Society Symposium Spring Meeting, San Francisco, California, USA. pp.Y8.32.1-Y8.32.6.

[70] W.S. Seo, J.H. Lee, X. Sun, Y. Suzuki, D. Mann, Z. Liu, M. Terashima, P.C. Yang, M.V. McConnell, D.G. Nishimura and H. Dai, "FeCo/graphitic-shell

nanocrystals as advanced magnetic-resonance-imaging and near-infrared agents," Nature Materials, Vol. 5, 2006, pp.971976.

[71] A. Abragam, *Principles of Nuclear Magnetism.* London: Oxford University Press, 1961.

[72] J. Pauly, P. Le Roux, D. Nishimura and A. Macovski, "Parameter Relations for the Shinnar-Le Roux Selective Excitation Pulse Design Algorithm," IEEE Transactions on Medical Imaging, Vol. 10, 1991, pp.53-65.

[73] M.R. Satcher, "De-bottling the electrospinning process using superparamagnetic particles," *Masters Thesis.* North Carolina State University, 2006.

[74] M.T. Thompson, "Simple Models and Measurements of Magnetically Induced Heating Effects in Ferromagnetic Fluids," IEEE Transactions of Magnetics, Vol. 34, 1998, pp.3755-3764.

[75] N.S. El Saghir, I.I. Elhajj1, F.B. Geara and M.H. Hourani, "Trauma-associated growth of suspected dormant micrometastasis," BioMed Central Cancer, Vol. 5, 2005, No. 94.

[76] F.G. Shellock, "Radiofrequency Energy-Induced Heating During MR Procedures: A Review," Magnetic Resonance in Medicine, Vol. 12, 2000, pp.3036.

[77] L.L. Wald and E. Adalsteinsson, "Parallel Imaging in Clinical MR Applications," in *Parallel Imaging in Clinical MR Applications*, (eds. Stefan O. Schoenberg, Olaf Dietrich and Maximilian F. Reiser), Berlin, Germany: Springer Berlin Heidelberg, 2007.

[78] Christopher M. Collins, Shizhe Li and Michael B. Smith, "SAR and B_1 field distributions in a heterogeneous human head model within a birdcage coil," Magnetic Resonance in Medicine, Vol. 40, No.6, pp. 847-856, 1998.

[79] A.C. Zelinski, K. Setsompop, V. Alagappan, B. Gagoski, F. Hebrank, U. Fontius, F. Schmitt, E. Adalsteinsson and L.L. Wald, "Pulse Design Methods for Reduction of Specific Absorption Rate in Parallel RF Excitation," Proceedings of the International Society for Magnetic Resonance in Medicine, Berlin, Germany, May 2007, p. 1698.

[80] R. Hergt and S. Dutz, "Magnetic particle hyperthermia - biophysical limitations of a visionary tumour therapy," Journal of Magnetism and Magnetic Materials, Vol. 311, pp. 187-192, 2007.

[81] R. Hergt, S. Dutz, R. Muller and M. Zeisberger, "Magnetic particle hyperthermia: nanoparticle magnetism and materials development for cancer therapy," Journal of Physics: Condensed Matter, Vol. 18, pp. S2919-S2934, 2006.

[82] P. Moroz, S.K. Jones and B.N. Gray, "Magnetically mediated hyperthermia: current status and future directions," International Journal of Hyperthermia, Vol. 18, pp. 267-284, 2002.

[83] A. Jordan, R. Scholz, P. Wurst, H. Fahling and R. Felix, "Magnetic fluid hyperthermia (MFH): Cancer treatment with AC magnetic field induced excitation of biocompatible superparamagnetic nanoparticles," Journal of Magnetism and Magnetic Materials, Vol. 201, pp. 413-419, 1999.

[84] W. Andra, C.G. d'Amblay, R. Hergt, I. Hilger and W.A. Kaiser, "Temperature distribution as function of time around a small spherical heat source of local mag-

netic hyperthermia," Journal of Magnetism and Magnetic Materials, Vol. 194, pp.197-203, 1999.

[85] I.A. Brezovich, "Low frequency hyperthermia," Medical Physics Monograph, Vol. 16, pp. 82-111, 1988.

[86] R. McDermott, A.H. Trabesinger, M. Muck, E.L. Hahn, A. Pines and J. Clark, "Liquid-State NMR and Scalar Couplings in Microtesla Magnetic Fields," Science, Vol. 295, 2002, pp. 2247-2249.

[87] P.C. Sen, *Principles of Electric Machines and Power Electronics*. New York: John Wiley and Sons, 1989.

[88] B.M. Berkovsky, "Thermomechanics of Magnetic Fluids: Theory and Applications," Proceedings of the International Advanced Course and Workshop on Thermomechanics of Magnetic Fluids, Udine, Italy, 1977.

[89] B.M. Berkovsky, V.F Medvedev and M.S. Krakov, *Magnetic Fluids: Engineering Application*, Oxford, England: Oxford University Press, 1993.

[90] V.G. Bashtovoy, B.M. Berkovsky and A.N. Vislovich, *Introduction to Thermomechanics of Magnetic Fluids*, Washington DC: Hemisphere Publishing Corporation, 1988.

[91] S. Kamiyama and J. Shimoiizaka, "Magnetic Fluids," Proceedings of the Fourth International Conference on Magnetic Fluids, Toyko and Sendai, Japan, 1986.

[92] P.G. de Gennes and P.A. Pincus, "Pair correlations in a ferromagnetic colloid," Zeitschrift fur Physik B Condensed Matter, Vol. 11, No. 189, 1970, pp. 189-198.

[93] J.F. Schenck, "The role of magnetic susceptibility in magnetic resonance imaging: MRI magnetic compatibility of the first and second kinds," Medical Physics, Vol. 23, 1996, pp. 815-850.

[94] D.G. Tomasi and R. Wang, "Induced magnetic field gradients and forces in the human head in MRI," Journal of Magnetic Resonance Imaging, Vol. 26, 2007, pp. 1340-1345.

[95] T. Budinger and C. Cullander, "Health effects of in vivo nuclear magnetic resonance," In: C. James C and A. Margulis, (eds). *Biomedical Magnetic Resonance*, San Francisco: Radiology Research and Education Foundation, 1984, pp. 421-441.

[96] T.F. Budinger, "Nuclear Magnetic Resonance (NMR) In-Vitro Studies: Known Thresholds for Health Effect," Journal of Computer Assisted Tomography, Vol. 51, 143–204, 1986.

[97] C. Rinaldi, A. Chaves, S. Elborai, X. He and M. Zahn, "Magnetic fluid rheology and flows," Current Opinion in Colloidal and Interface Science, Vol. 10, 2005, pp. 141-157.

[98] Y. Haik, V. Pai, C-J. Chen, "Apparent viscosity of human blood in a high static magnetic field," Journal of Magnetism and Magnetic Material, Vol. 225, pp. 180-186, 2001.

[99] H.H. Woodson and J.R. Melcher, *Electromechanical Dynamics*, New York: John Wiley and Sons, 1968.

[100] S. Goldstein, (ed), *Modern Developments in Fluid Dynamics*. Vol. 1. New York: Dover Publications, 1965.

[101] R.M. Weisskoff and S. Kiihne S., "MRI susceptometry: image-based measurement of absolute susceptibility of MR contrast agents and human blood," Magnetic Resonance in Medicine, Vol. 24, pp. 375-383, 1992.

[102] R.P. Kennan, J. Zhong and J.C. Gore, "Intravascular susceptibility contrast mechanisms in tissues," Magnetic Resonance in Medicine, Vol. 31, pp. 9-21, 1994.

[103] E.B. Mason, *Human Physiology.* New York: Addison Wesley/Cummings Publishing Company, p.275, 1983.

[104] A. Potthast, (Siemens Medical Solutions, Erlangen, Germany), *Private Communication*, 2007.

[105] G.K. Batchelor, *An Introduction to Fluid Dynamics.* Cambridge, England: Cambridge University Press, 2000.

[106] E.E. Tzirtzilakis, "A mathematical model for blood flow in magnetic field," Physics of Fluids, Vol. 17, 2005, p. 077103(15).

[107] F. Gazeau, B.M. Heegaard, J.-C. Bacri, A. Cebers and R. Perzynski, "Magnetic susceptibility in a rotating ferrofluid: Magneto-vortical resonance," Europhysics Letters, Vol. 35, 1996, pp. 609-614.

[108] J.-C. Bacri, R. Perzynski, M.I. Shliomis, G.I. Burde, "Negative-Viscosity Effect in a Magnetic Fluid," Physical Review Letters, Vol. 75, 1995, pp. 2128-2131.

[109] J Singh and R. Bajaj, "Couette flow in ferrofluids with magnetic field," Journal of Magnetism and Magnetic Materials, Vol. 294, 2005, pp. 53-62.

[110] V.S. Zotev, A.N. Matlashov, P.L. Volegov, A.V. Urbaitis, M. A. Espy and R. H. Kraus Jr., "SQUID-based instrumentation for ultralow-field MRI," Superconductor Science and Technology, Vol. 20, 2007, pp. S367S373.

[111] L.A. Zaremba, "FDA Guidelines for Magnetic Resonance Equipment Safety," Proceedings of the American Association of Physicists in Medicine Annual Meeting, Montreal, Canada, July 2002.

[112] F.G. Shellock, "Metallic Neurosurgical Implants: Evaluation of Magnetic Field Interactions, Heating, and Artifacts at 1.5-Tesla," Journal of Magnetic Resonance Imaging, Vol. 14, 2001, pp. 295299.

[113] R.E. Rosensweig, "Heating magnetic fluid with alternating magnetic field," Journal of Magnetism and Magnetic Materials, Vol. 252, 2002, p. 370.

[114] A.S. Lubbe, C. Alexiou and C. Bergemann, "Clinical applications of magnetic drug targeting," Journal of Surgical Research, Vol. 95, 2001, pp. 200-206.

[115] P.A. Voltairas, D.I. Fotiadis and L.K. Michalis, "Hydrodynamics of magnetic drug targeting," Journal of Biomechanics, Vol. 35, 2002, pp. 813-821.